

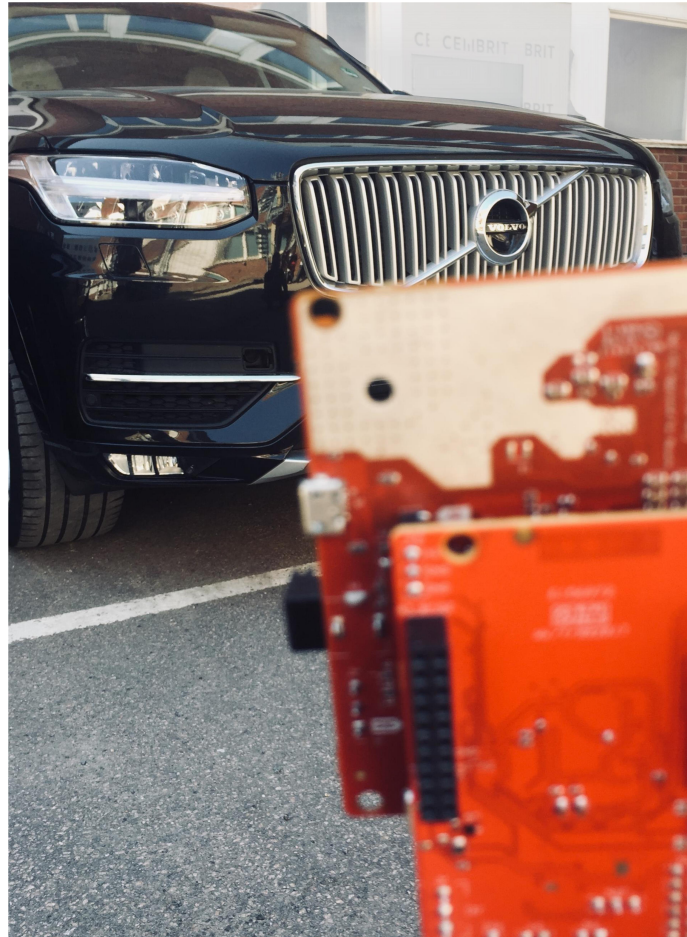


**CHALMERS**  
UNIVERSITY OF TECHNOLOGY



UNIVERSITY OF GOTHENBURG

---



# Automotive FMCW Radar Development and Verification Methods

Master's thesis in Embedded Electronic System Design

SANOAL MACHADO

SANTIAGO MANCHENO

---

Department of Computer Science and Engineering  
CHALMERS UNIVERSITY OF TECHNOLOGY  
UNIVERSITY OF GOTHENBURG  
Gothenburg, Sweden 2018



MASTER'S THESIS 2018

# Automotive FMCW Radar Development and Verification Methods

SANOAL MACHADO  
SANTIAGO MANCHENO



Department of Computer Science and Engineering  
CHALMERS UNIVERSITY OF TECHNOLOGY  
UNIVERSITY OF GOTHENBURG  
Gothenburg, Sweden 2018

Automotive FMCW Radar Development and Verification Methods  
SANOAL MACHADO  
SANTIAGO MANCHENO

© SANOAL MACHADO & SANTIAGO MANCHENO, 2018.

Supervisor: Lena Peterson, Department of Computer Science and Engineering.  
Company Supervisor: Kristian Adziewski, Volvo Cars.  
Examiner: Per Larsson-Edefors, Department of Computer Science and Engineering.

Master's Thesis 2018  
Department of Computer Science and Engineering  
Chalmers University of Technology and University of Gothenburg  
SE-412 96 Gothenburg  
Telephone +46 31 772 1000

Cover: Back-side view of hardware radar module aiming at a XC90 Volvo Car.

Typeset in L<sup>A</sup>T<sub>E</sub>X  
Gothenburg, Sweden 2018

## Abstract

This report describes the research on radar development and virtual verification methods using an automotive frequency-modulated continuous-wave (FMCW) mmWave sensing module. This thesis work provides a clear description on how a radar works from the analog front-end to target characterization through digital signal processing (DSP), by providing accurate and efficient verification methods to evaluate not only the radar performance but also the target characteristics. The report starts with a theoretical overview on FMCW radar concepts. The next part of report gives a detailed explanation on developing and setting up the hardware tool chain along with the software and tools that are necessary to capture the raw analog-to-digital converter (ADC) data. The next section of the report focuses on the main adopted implemented methodologies for the DSP block. Once all these different topics are covered, this project concludes by comparing the obtained results from the DSP algorithms with the ground-truth data obtained from different pre-defined hardware (HW) test-scenarios.

The results from the thesis work mainly focus in three different type of analysis: stationary targets, dynamic targets and the comparison of implemented adaptive signal processing algorithm. For the first two type of analysis, results provide some evaluation criteria on fundamental radar performance parameters such as range, velocity and angle of arrival (AoA) estimation of the measured target with respect to radar. Additionally, the signal-to-noise ratio (SNR) is exploited to calculate one of the most relevant target characterization parameters: the radar cross section (RCS). For the last type of analysis, a success rate indicator compares and contrasts the performance of the proposed adaptive signal-processing algorithm with other similar implementations. The results from the analysis confirms the right implementation of a radar verification tool, which allows the user to extract the most relevant characteristics of the radar and target, with the freedom of changing the main algorithmic parameters and observe their effect on target detection and characterization. From the results, is clear that future improvements are needed to improve target detection algorithms especially for the cases involving certain corner scenarios.

**Keywords:** *FMCW radar, AWR1243 mmWave sensing module, Target detection, Adaptive signal processing, Evaluation module, Radar thermal noise, Radar clutter.*

## Acknowledgements

First of all, we would like to thank Volvo Cars AB for giving us the wonderful opportunity to perform this master thesis. We would also like to thank our supervisor Kristian Adziewski at Volvo Cars and academic supervisor Lena Peterson at Chalmers University for all the help, constant support and knowledge shared with us. A special thanks to Tian Zheng and Elias Marel from Volvo Cars for sharing their knowledge on the subject, constructive feedback and endless ideas.

Last but not the least, we would also like to thank our respective families for being our constant moral support throughout this thesis work. This project, with all the hard and constant dedication behind it, is dedicated to all of you. Without your support, none of this would have been possible.

Sanoal Machado & Santiago Mancheno, Gothenburg, June 2018



# Contents

|  |           |
|--|-----------|
| <b>List of Acronyms</b>                | <b>x</b>  |
| <b>1 Introduction</b>                  | <b>1</b>  |
| 1.1 Context                            | 1         |
| 1.2 Problem Statement                  | 3         |
| 1.3 Thesis Outline                     | 4         |
| <b>2 Background</b>                    | <b>5</b>  |
| 2.1 The FMCW Radar                     | 5         |
| 2.1.1 Range Estimation                 | 7         |
| 2.1.2 Velocity Estimation              | 10        |
| 2.1.3 Angle Estimation                 | 13        |
| 2.1.4 Summary of Estimation Facts      | 15        |
| 2.2 Signal and Target Characterization | 16        |
| 2.2.1 Signal-to-Noise Ratio (SNR)      | 16        |
| 2.2.2 Radar Cross Section (RCS)        | 18        |
| 2.3 The CA-CFAR detection              | 18        |
| <b>3 Hardware Tool Chain</b>           | <b>21</b> |
| 3.1 AWR1243 BoosterPack                | 21        |
| 3.2 mmWave-DevPack                     | 24        |
| 3.3 TSW1400 EVM                        | 24        |
| <b>4 Software and Tools</b>            | <b>27</b> |
| 4.1 Firmware and GUI                   | 27        |
| 4.1.1 DFP Firmware Package             | 27        |
| 4.1.2 Radar Studio                     | 27        |
| 4.1.3 HSDC Pro                         | 28        |
| 4.2 FMCW Chirp and Frame Structure     | 28        |
| 4.3 Raw ADC Data Format                | 29        |
| <b>5 System Implementation</b>         | <b>32</b> |
| 5.1 MATLAB Post-Processing             | 32        |
| 5.1.1 DSP-IP Block Overview            | 32        |
| 5.1.2 Range Estimation (1D-FFT)        | 33        |
| 5.1.3 Velocity Estimation (2D-FFT)     | 34        |
| 5.1.4 Angle Estimation (3D-FFT)        | 36        |
| 5.1.5 Lateral Distance Estimation      | 39        |
| 5.1.6 1D and 2D CA-CFAR                | 40        |

---

|          |   |            |
|----------|---|------------|
| 5.1.7    | SNR and RCS Estimation . . . . .                      | 43         |
| 5.1.8    | The Spectral Power of the Raw ADC Data . . . . .      | 45         |
| 5.2      | HW-Scenario Definition . . . . .                      | 45         |
| 5.2.1    | Stationary Test Case Scenarios . . . . .              | 46         |
| 5.2.2    | Dynamic Test Case Scenario . . . . .                  | 47         |
| 5.2.3    | Configuration of Chirp and Frame Parameters . . . . . | 47         |
| <b>6</b> | <b>Results and Analysis</b>                           | <b>49</b>  |
| 6.1      | Stationary Results . . . . .                          | 49         |
| 6.1.1    | Calibration Case: The Corner Reflector . . . . .      | 49         |
| 6.1.2    | Target Characterization: The Polar RCS . . . . .      | 53         |
| 6.2      | Dynamic Results: Moving Target Analysis . . . . .     | 55         |
| 6.2.1    | Range Profile (1D) Results . . . . .                  | 56         |
| 6.2.2    | Range-Doppler Profile (2D) Results . . . . .          | 57         |
| 6.2.3    | Angle Profile (3D) Results . . . . .                  | 58         |
| 6.2.4    | SNR and RCS Results . . . . .                         | 61         |
| 6.3      | CA-CFAR Performance Results . . . . .                 | 63         |
| <b>7</b> | <b>Conclusion and Future Work</b>                     | <b>65</b>  |
|          | <b>Bibliography</b>                                   | <b>68</b>  |
| <b>A</b> | <b>Appendix 1</b>                                     | <b>I</b>   |
| <b>B</b> | <b>Appendix 2</b>                                     | <b>III</b> |

# List of Acronyms

|                |   |
|----------------|---|
| <b>ACC</b>     | Adaptive cruise control   |
| <b>ADAS</b>    | Autonomous-driving assistance systems                               |
| <b>ADC</b>     | Analog-to-digital converter   |
| <b>AEBS</b>    | Automatic emergency breaking system                                 |
| <b>AoA</b>     | Angle of arrival  |
| <b>AR</b>      | Automotive radar  |
| <b>ASIC</b>    | Application-specific integrated circuit                             |
| <b>BIST</b>    | Built-in self-test  |
| <b>CA-CFAR</b> | Cell-averaging Constant false-alarm rate                            |
| <b>CMOS</b>    | Complementary metal-oxide-semiconductor                             |
| <b>CSI</b>     | Camera serial interface   |
| <b>CUT</b>     | Cell under test   |
| <b>DAC</b>     | Digital-to-analog converter   |
| <b>DBF</b>     | Digital beam forming  |
| <b>DFP</b>     | Device firmware package   |
| <b>DOA</b>     | Direction of arrival  |
| <b>DSP</b>     | Digital signal processing   |
| <b>ESPRIT</b>  | Estimation of Signal Parameters via Rotational Invariance Technique |
| <b>EVM</b>     | Evaluation module   |
| <b>FER</b>     | Frame error rate  |
| <b>FFT</b>     | Fast Fourier transform  |
| <b>FMCW</b>    | Frequency-modulated continuous-wave                                 |
| <b>FPGA</b>    | Field-programmable gate array                                       |
| <b>FTDI</b>    | Future technology devices internal                                  |
| <b>GUI</b>     | Graphical user interface  |
| <b>HD</b>      | High density  |
| <b>HSDC</b>    | High speed data converter   |

|              |                                     |
|--------------|-------------------------------------|
| <b>I32</b>   | 32 signed integer                   |
| <b>IF</b>    | Intermediate frequency              |
| <b>IP</b>    | Intellectual property               |
| <b>LDO</b>   | Low dropout                         |
| <b>LNA</b>   | Low-noise amplifier                 |
| <b>LVDS</b>  | Low-voltage differential signalling |
| <b>MPD</b>   | Matrix pencil method                |
| <b>MSS</b>   | Master subsystem                    |
| <b>MUSIC</b> | Multiple signal classification      |
| <b>PCB</b>   | Printed circuit board               |
| <b>PLL</b>   | Phase-locked loop                   |
| <b>RCS</b>   | Radar cross section                 |
| <b>RTT</b>   | Round-trip time                     |
| <b>SNR</b>   | Signal to noise ratio               |
| <b>SOI</b>   | Signal of interest                  |
| <b>SOP</b>   | Sense on power                      |
| <b>SPI</b>   | Serial peripheral interface         |
| <b>SRR</b>   | Short-range radar                   |
| <b>TI</b>    | Texas Instruments                   |
| <b>USB</b>   | Universal serial bus                |
| <b>UWB</b>   | Ultra wide-band                     |
| <b>WHO</b>   | World health organization           |

# 1

## Introduction

It is undeniable that, with the constant innovation and technology improvement in the automobile industry, cars have become a central part of our daily lives. For this reason, safety is, and will always be, the highest priority in order to prevent fatalities or serious injuries for all car occupants. The world health organization (WHO) [1] shows that 1.25 million people die each year as a result of road traffic accidents and, without any action, these crashes are predicted to become the 7<sup>th</sup> leading cause of death by 2030. To overcome these challenges, measures are taken by automobile companies to improve the efficiency of active-safety systems on cars. Currently, it is an ongoing investigation domain, which needs new and updated knowledge, which is usually obtained through research and development projects.

The active-safety department at Volvo Cars Corporation is constantly developing new functions and frameworks that are needed to build cars with very high safety standards. Since safety has always been the highest priority at Volvo Cars, it has become the key motivation for Vision 2020, which aims for zero fatalities and serious injuries in all new Volvo cars by 2020. The safety of these cars relies heavily on the performance of multiple sensors including radars, laser, cameras, lidars, ultrasonic sensors, among others. For this reason, creating new investigation projects that will test the performance of different sensors, will not only improve the current active-safety systems, but will also evaluate new alternatives for more reliable ones.

### 1.1 Context

Automotive radar (AR) is one among the primary sensors, which is becoming significant in automotive technology [2]. The increased popularity of AR is because when compared to other sensors, radar has a high tolerance for all environmental conditions such as fog, rain, snow, and bad or dazzling light [3]. The radar technology usually employed nowadays for AR is a frequency-modulated continuous-wave (FMCW) signal. FMCW is highly flexible with relatively moderate signal processing requirements, which can be met with low-cost field-programmable gate arrays (FPGAs), microprocessors with specialized acceleration engines or specialized application-specific integrated circuits (ASICs).

The main purpose of FMCW radar is to measure the target range, velocity and angle estimation by using a frequency-modulated continuous signal, known as the beat frequency or the intermediate frequency (IF) [2]. This signal is mainly modulated linearly and can be modelled using a propagation delay and the Doppler frequency [4]. To emphasize the importance of this beat frequency, the analytical explanation [5] in (1.1) presents how the beat frequency is directly proportional to the round-trip time (RTT) of the target as well

as to its range. The equation for the beat frequency ( $f_b$ ) is

$$f_b = \frac{\Delta f}{T_b} \cdot T_p, \quad (1.1)$$

where  $\Delta f$  is the frequency unit change,  $T_b$  is the beat frequency period, and  $T_p$  is the RTT to the target. RTT to the target is also equal to  $T_p = (2R)/c$ , where  $R$  is the range and  $c$  is the velocity of light. However, in most AR applications, not only target range and velocity are to be measured but also the angle position (azimuth and elevation angle). An array of receiving antennas (a common characteristic of FMCW radars), will provide the required angle information using digital beam forming (DBF) processing [6].

There are several advantages in the usage of FMCW radars linked to their hardware and software characteristics. On the hardware side, one advantage is related to their physical characteristics by using simple solid-state transceivers, which have enabled millimeter-wave radars operating at higher frequencies. These frequencies (77 – 81 GHz) are now part of a regulatory assigned wide-band (75 – 110 GHz) often referred as the ultra wide-band (UWB) short-range radar (SRR) [7]. On the software side, the advantage is that the FMCW radar can use the fast Fourier transform (FFT) as the main correlator to accurately detect multiple objects based on their tones in the frequency domain. For example, in a typical FMCW radar with a fast-ramp waveform approach, 2D FFT and DBF algorithms are used for target detection [6]. The efficient 1D FFT and 2D FFT processing methods<sup>1</sup> mainly enable, in most cases, an accurate estimation of range and velocity of the object without any ambiguity. This is particularly important in the detection of multiple objects.

However, there are still a number of challenges that need to be addressed while designing the FMCW radar. One of these is the leakage of the transmitted signal into the receiver. This problem may result in consequences from degrading the receiver's sensitivity to completely damaging the receiver's mixer depending on the transmitted power level. Several alternatives to overcome this problem [2] consider the physical separation of the transmitter and receiver antenna or the implementation of a reflected power canceller. Another challenge for FMCW radars while measuring range and velocity together, is the ambiguity in the results which may cause ghost or missed targets for particular corner cases in which there are multiple equidistant targets moving at the same velocity. Given the importance of this challenge, several alternatives have been proposed. First, different linear modulation patterns [3], [4], [8] using subsequent ramp signals with different slopes can be used for multiple-target detection. Also, a 3D FFT processing method (known as the Angle FFT) [9], can be introduced as a solution to this challenge by measuring the angle position of the targets. Finally, various algorithmic approaches from inserting additional moving target, DBF, and decision blocks [6] to adapting a matrix pencil method (MPD) for a multidimensional range-velocity spectrum [10] have been investigated. Nonetheless, future implementation, verification or modification of these algorithms and their effect on the detection performance are still to be determined.

Although all challenges mentioned before need to be considered for an accurate FMCW radar development, there are several additional problems that have not been yet substantially addressed in the literature or current research projects. The first problem, is related to the migration challenge from the legacy 24 GHz operational frequency to the SRR band. Despite the fact that there is a complete approach of a fully-integrated and highly linear 79 GHz FMCW synthesizer [7], future research on high-frequency resolution and

---

<sup>1</sup>In most literature, the 1D FFT is known as Range FFT and the 2D FFT is known as Doppler FFT.

its effects on the sensor performance is still a research area in need of more investigation. Last, another main challenge is related to the lack of proper radar design-verification loops to carefully investigate and understand how the raw-radar digital data is structured and how it can be used to model the hardware performance. Understanding this verification/modelling process will have a huge impact on the development and evaluation time of any current implementation.

## 1.2 Problem Statement

The goal of this thesis work is to develop a radar design-verification chain of an automotive FMCW radar from the pure analog waveform to digital signal processing by utilizing a 76 – 81 GHz development radar prototype available at Volvo Cars. This project is intended as an initial step towards the development of an in-house radar design-verification loop, which contains an internally developed digital signal processing (DSP) intellectual property (IP) block which is not currently available at Volvo Cars. Based on the input data stream, the implemented radar-verification system will be capable of providing several main contributions. First, it will be capable of evaluating raw radar data at every stage of the DSP processing from signal acquisition up to target detection. Second, it will provide a tool to the users to evaluate not only the radar performance but target characteristics with the freedom of changing main algorithmic design parameters and observe the impact on the DSP results. Finally, it will also give the opportunity to provide designers with a deeper understanding of radar modelling in accordance with the selected test parameters.

The main input data stream for the implemented system will come from the hardware tool-chain (input FMCW transceivers) as presented in Fig. 1.1.

In accordance with the given input, the verification process will compare the measurement results, i.e. target range measurement, target velocity, target angular position, among others, with the ground truth data (real physical measurements) of different test-scenarios with different types of targets. This final comparison will elucidate the performance of the implemented system.

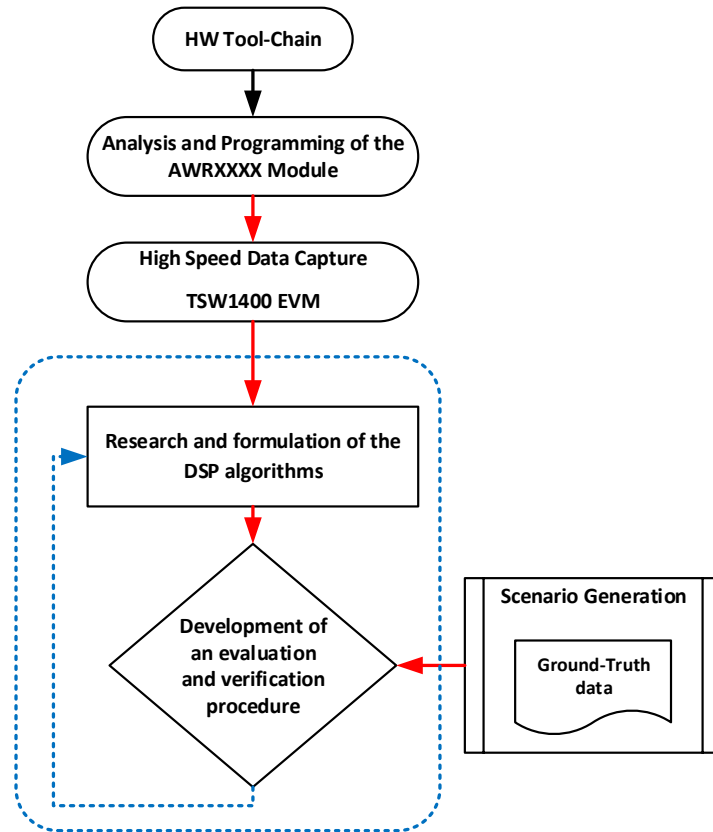


**Figure 1.1:** Problem Statement Flowchart: It starts with a first step of input data generation (from the HW model). This first step is then followed by the development of our own DSP algorithms. Finally, an evaluation loop is generated to verify the results from the DSP algorithms compared with the test scenario (physical ground-truth) data. A deeper detail on input generation, DSP processing and verification methods will be explained in further chapters.

### 1.3 Thesis Outline

The work flow shown in Fig. 1.1, summarizes the general concept of the project while providing different abstraction levels in order to converge into the intended design-verification system.

The organization of this thesis is as follows. In Chapter 2, we introduce and discuss the theoretical background of the FMCW radar, and review the main mathematical and algorithmic procedures for the post-capture DSP. In Chapter 3 and 4, we explain in detail the characteristics of the provided hardware tool-chain, software and tools that are used to extract the raw-digital radar data. In Chapter 5, we demonstrate the specifics of our current implementation concerning algorithm development and test-scenario definition. In Chapter 6, we discuss about the obtained results and errors while providing a complete analysis on the acquired outcome. Finally, in Chapter 7, we summarize our entire contribution with conclusions and present a short discussion on the possible future work that can be generated from the outcome of this thesis project.

# 2

## Background

As stated in Chapter 1, the FMCW signal technology is becoming more relevant for AR sensor systems. For this reason, a more detailed explanation on the theoretical and mathematical background of FMCW signals is required to understand how the signal is synthesized, received and post-processed. In this chapter, a complete explanation of the basic operation of the FMCW radar is introduced, followed by the procedure of how to estimate relevant target characteristics such as range, velocity and angle. Then, a description of signal and target characterization is provided by exploiting concepts like signal to noise ratio (SNR) and radar cross section (RCS) respectively. Finally, this chapter ends with a description of a basic technique for target detection based on the average spectral energy from the measured signal.

### 2.1 The FMCW Radar

The main concept behind any FMCW radar is a signal which is known as a “*chirp*”. This signal can be understood as a sinusoidal wave with a frequency value that increases linearly with time as presented in Fig. 2.1 a) (as an amplitude-time plot) and b) (as an instantaneous frequency-time plot). This linear change characteristic of the chirp signal creates the saw-tooth type frequency as shown in Fig. 2.1.

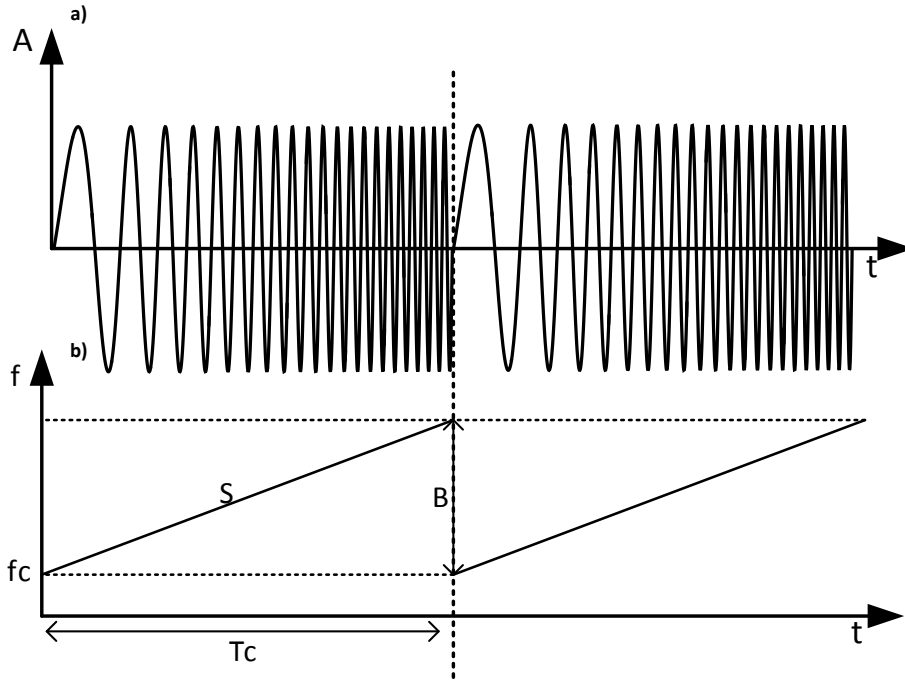


**Figure 2.1:** Chirp Signal. Figure a) shows the amplitude-time domain representation. Figure b) shows the instantaneous frequency-time domain representation.

From Fig. 2.1 b), we can extract four important characteristics that describe every chirp signal. First we have the ramp-start or start frequency ( $f_c$ ), which is the initial frequency value. As mentioned before, the development of this thesis was performed using a mmWave radar module with an operating frequency range of (76-81) GHz. Second we have the frequency sweep bandwidth ( $B$ ), which represents the frequency interval between the ramp-start and ramp-end values. Third, the chirp duration ( $T_c$ ) represents the allocated chirp cycle time. Finally, the chirp slope ( $S$ ) which can be defined as

$$S = \frac{B}{T_c}, \quad (2.1)$$

represents the rate of change of the chirp signal frequency per unit of time.

Once the chirp signal is introduced, it becomes more natural to explain the workflow of a general FMCW radar. For this purpose, the workflow diagram presented in Fig. 2.2 conveys all the main steps executed by the radar from the transmission of the signal, reception of the reflected signal, up to the digital front-end signal sampling.

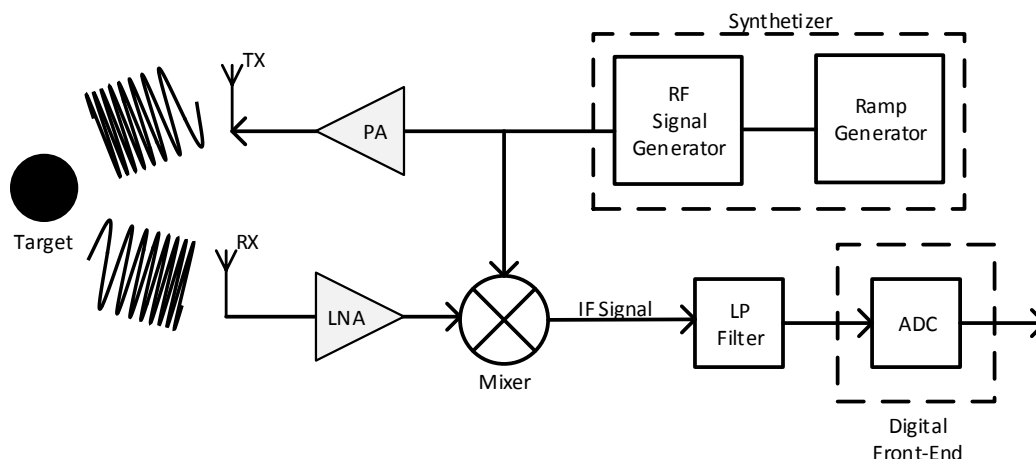


**Figure 2.2:** FMCW Radar Workflow: An on-board synthesizer creates the chirp signal based on the different user-configurable chirp parameters. This chirp signal is then transmitted. The received signal is mixed with the original chirp signal to generate the IF signal. Finally, this IF signal is low-pass filtered and digitized [9] [11].

Based on the workflow presented in Fig. 2.2, the FMCW radar general steps can be described as follows. Initially, an on-board synthesizer (composed by a ramp and an RF-signal generator) creates the chirp signal based on the different user-configurable chirp parameters (as detailed in the following chapters). Once the chirp is amplified and transmitted (TX), the receiver antenna (RX) detects the reflected-delayed version of the same chirp signal. This received signal, after the low-noise amplifier (LNA), is mixed with the original one to generate the beat frequency or IF signal. Finally, this IF signal is low-pass filtered, to eliminate any high-frequency contributions, and digitized. The resulting serialized digital signal is ready to be transmitted to any other device for the corresponding post-processing DSP algorithms.

The DSP algorithms will be based on a mathematical layout in which, by analyzing the signal on the frequency domain, multiple physical characteristics of the measured target(s) such as range, velocity, angle, among others can be derived. These characteristics will be detailed on the following subsections and will serve as a platform model for the further algorithm development used on this thesis work.

### 2.1.1 Range Estimation

The first and most frequent measurement result from the usage of a FMCW radar is the range estimation, which corresponds to the distance between the radar module (with the on-board transmitting and receiving antennas) and the measured target. However, to fully understand how the range is related to the chirp signal, one must refer back to the radar workflow diagram in Fig. 2.2 and analyze the IF signal coming from the mixer block.

The output from a mixer block ( $X_{\text{out}}$ ) from two sinusoidal inputs can be represented as

$$X_{\text{out}}(t) = \sin [(\omega_1 - \omega_2)t + (\theta_1 - \theta_2)], \quad (2.2)$$

where  $\omega_1 - \omega_2$  and  $\theta_1 - \theta_2$  are the difference of the instantaneous frequencies and phase of the two input signals respectively, as presented in Fig. 2.3. In this diagram, a single target in front of the radar produces an IF signal with a constant frequency value of  $S \cdot \tau$  (where  $S$  is the slope of the chirp and  $\tau$  is the RTT).

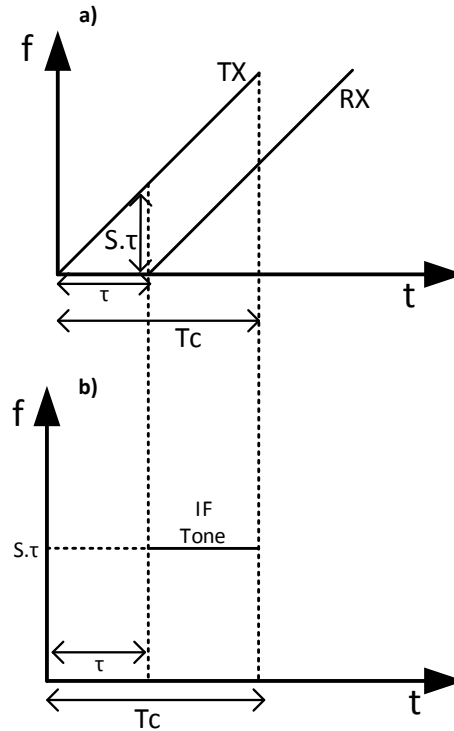


**Figure 2.3:** IF signal of a one-target measurement. Figure a) shows the frequency-time domain representation of the transmitted and received signal. Figure b) shows the frequency-time domain representation of the IF tone [9].

The relationship between the IF tone value with the target range ( $R$ ) can be explained by using (1.1) in which the value of  $S \cdot \tau$  can be expressed as

$$IF_{\text{tone}} = S \cdot \tau = S \cdot \frac{2R}{c}. \quad (2.3)$$

For the case where not only one, but multiple objects are placed in front of the radar, multiple reflected chirps will be detected by the RX antenna and multiple IF tones will be obtained as illustrated in Fig. 2.4. It is important to notice that the frequency value of each IF tone is proportional to the range to each target that is placed in front of the radar.

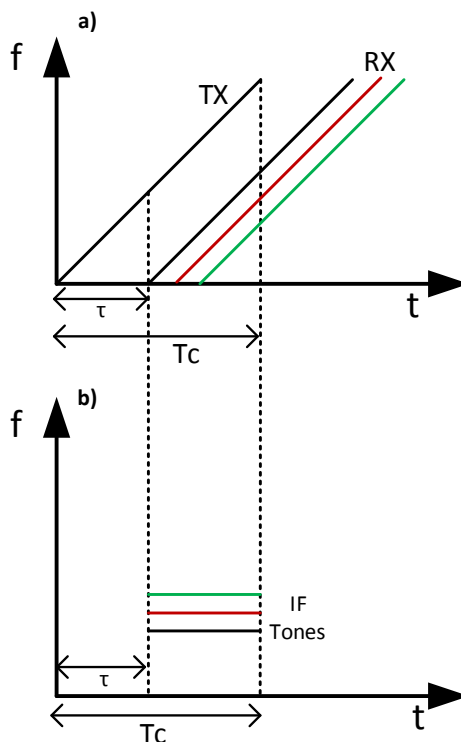


**Figure 2.4:** IF signal of a multiple-target measurement. Figure a) shows the frequency-time domain representation of the transmitted and received signals. Figure b) shows the frequency-time domain representation of the IF tones [9].

For a single- or multiple-object detection case scenario, it is important to define limits on how far the object(s) can be located from the radar module to generate a correct detection and how close the targets can be to each other for the radar to be able to separate them (multiple-object detection). For these reasons, it is relevant to define the two main characteristics of range estimation as range resolution and maximum range distance.

Considering once again the definitions of the beat frequency (1.1) and chirp slope (2.1), and recalling that two tones can be resolved in frequency as long as their difference ( $\Delta f_c$ ) is greater than  $1/T_c$ , the range resolution ( $R_{\text{res}}$ ) can be defined as

$$R_{\text{res}} = \frac{c}{2B}, \quad (2.4)$$

which depends mainly on the swept bandwidth ( $B$ ) of the chirp.

If we now refer back to Fig. 2.4, the highest frequency value IF tone will determine the desired maximum distance that the radar can detect. However, considering the workflow presented in Fig. 2.2, this IF signal must be digitized for further DSP. For this reason, the IF-bandwidth will be limited to the sampling frequency ( $f_s$ ) of the analog-to-digital converter (ADC). Considering this limitation and using the definition of beat frequency

i.e., (1.1), the maximum range distance ( $R_{\max}$ ) can be defined as

$$R_{\max} = \frac{f_s c}{2S}, \quad (2.5)$$

which is directly proportional to the sampling frequency ( $f_s$ ).

### 2.1.2 Velocity Estimation

In a multiple-object detection scenario, consisting of multiple targets (with different relative velocities) which are equidistant from the radar, there is a relevant problem in object detection using the range estimation FFT. This problem is caused by the fact that the frequency transform of that instant measurement will only contain one peak (one IF tone), since all targets are located at the same distance from the radar. Therefore, for the radar to be able to separate out the objects not only in the terms of their range, but also for their relative velocities, the phase of the IF signal ( $\Phi_0$ ) must be taken into consideration.

To demonstrate that the phase variation ( $\Delta\Phi$ ) of the IF signal is proportionally related to the range variation ( $\Delta R$ ), Fig. 2.5 presents a diagram that clearly shows the effect of a  $\Delta\tau$  displacement over the transmitted (TX) and received (RX) signal. This diagram resembles a single-target scenario.

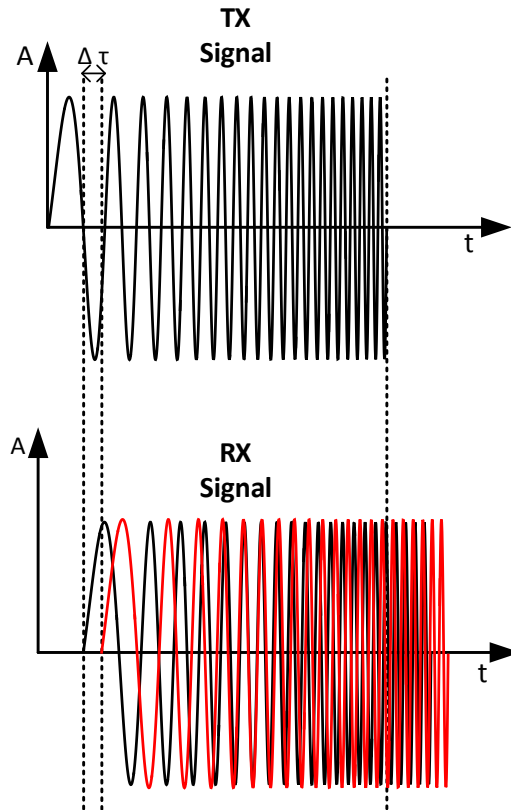


**Figure 2.5:** TX and RX signal representation after a  $\Delta\tau$  shift [9].

If the target is moving at a certain relative velocity with respect to the radar, the RX signal shifts an amount of  $\Delta\tau$  (red signal in diagram) while the TX signal travels an additional phase of  $2\pi f_c \Delta\tau$ , then the conventional sinusoidal representation of the TX and RX signal can be represented as

$$TX||RX = A \cdot \sin(2\pi f_c t + \Phi_0), \quad (2.6)$$

where  $A$  is the amplitude,  $f_c$  is the chirp carrier frequency, and  $\Phi_0$  is the phase value. The IF signal phase difference can be defined by using (1.1), and recalling that  $c = \lambda \cdot f_c$  and  $\tau$  represents the RTT. This phase difference can be represented as

$$\Delta\Phi = 2\pi f_c \Delta\tau = \frac{4\pi \Delta R}{\lambda}, \quad (2.7)$$

where  $\lambda$  is the wavelength.

Now, considering that a normal FMCW radar transmits not one but multiple chirp signals separated by a time period of  $T_c$ , the phase difference measured across two consecutive chirps can be used to estimate the velocity of the target ( $v$ ) that has travelled a  $\Delta R = v \cdot T_c$  distance. Replacing this result and rearranging (2.7), the velocity of the target can be expressed as

$$v = \frac{\lambda \Delta\Phi}{4\pi T_c}. \quad (2.8)$$

To expand the velocity estimation further, let's now consider a multiple-object scenario in which two (or more) targets are equidistant to the radar but with different relative velocities. Similar to the single-object scenario described before, there will be a single IF tone measured by the radar. However, this tone will now contain the phase information of all the targets. For this reason, in order to resolve and detect every multiple object, a discrete “*Doppler-FFT*” technique needs to be applied over a series of range-FFT peaks that correspond to every  $N$ -equispaced transmitted chirps as presented in Fig. 2.6.

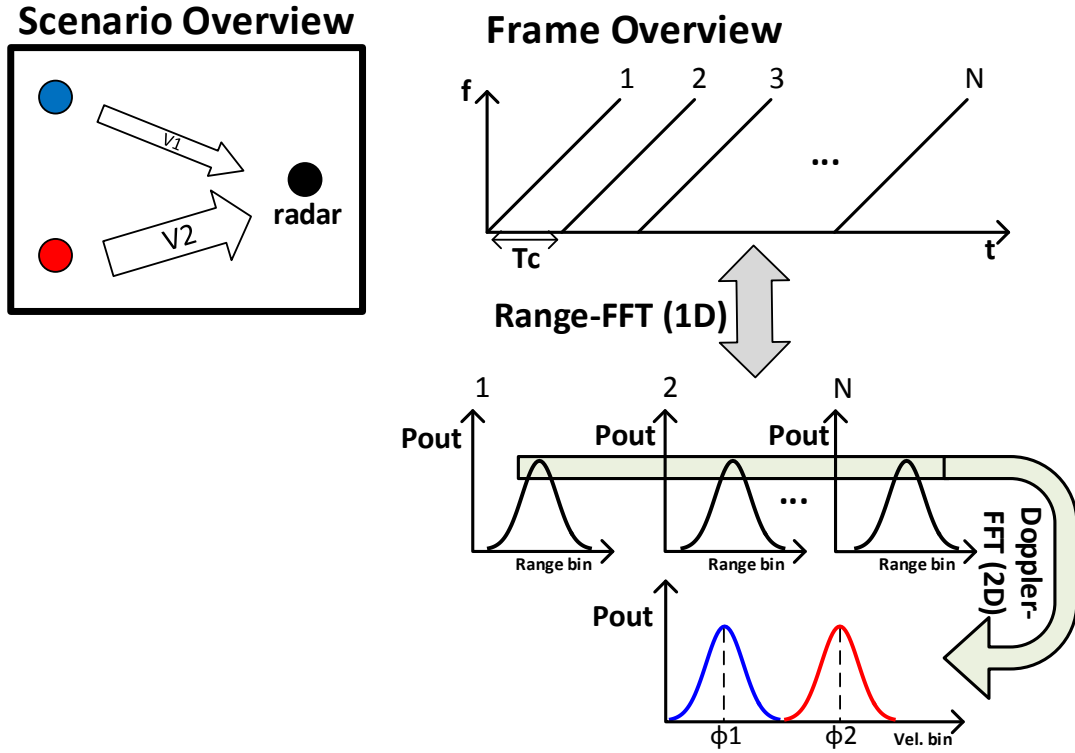


**Figure 2.6:** Multiple-object velocity estimation workflow. For this scenario, the two targets have different relative velocities [9].

From Fig. 2.6, we can notice that each peak of the Doppler-FFT corresponds to the phase difference of one measured target. Furthermore, recalling the results from (2.8), the relative velocities of the targets can be expressed as

$$v_1 = \frac{\lambda \Delta \Phi_1}{4\pi T_c} \quad || \quad v_2 = \frac{\lambda \Delta \Phi_2}{4\pi T_c}, \quad (2.9)$$

with an assumption that the two objects are approaching the radar.

Once the velocity-estimation concept is defined, there are two remaining characteristics that need to be clarified, i.e., velocity resolution ( $v_{\text{res}}$ ) and maximum velocity ( $v_{\text{max}}$ ). Velocity resolution can be defined as the minimum velocity between objects for the radar to be able to detect them separately. Using (2.7) and recalling that for a discrete signal, we find that two or more peaks can be separated (in frequency) as long as they are  $(2\pi)/N$  (radians/samples) apart, the velocity resolution can be defined as

$$\begin{aligned} \Delta \Phi &> \frac{2\pi}{N} \\ v &> \frac{\lambda}{2NT_c} \\ \Rightarrow v_{\text{res}} &= \frac{\lambda}{2T_f}, \end{aligned} \quad (2.10)$$

where  $NT_c$  is known as the frame time ( $T_f$ ). On the other hand, the maximum velocity can be estimated from the fact that, as mentioned in [9], unambiguous velocity can be measured only if the phase difference ( $\Delta\Phi$ ) is less than  $\pi$  radians. Therefore, the maximum velocity can be expressed as

$$\begin{aligned}\Delta\Phi &< \pi \\ v &< \frac{\lambda}{4T_c} \\ \Rightarrow v_{\max} &= \frac{\lambda}{4T_c},\end{aligned}\tag{2.11}$$

which is inversely proportional to the chirp periodicity ( $T_c$ ).

### 2.1.3 Angle Estimation

So far, we have discussed about single- and multiple-object scenarios with different relative velocities to the radar. However, there is still one more scenario that has not been covered yet. Now, consider a multiple-object scenario in which two or more targets are approaching the radar at the same range and with the same relative velocity. According to our previous results, this scenario will generate a single-tone peak in both, 1D and 2D, FFT analysis. To be able to separate objects moving at the same distance and velocity, the angle of arrival (AoA) must be taken into consideration. It is important to mention that angle estimation needs at least two receiving antennas.

Fig. 2.7 illustrates how the AoA can be calculated for a single-object scenario. In this diagram, we assume having one transmitting (TX) and two receiving (RX) antennas.

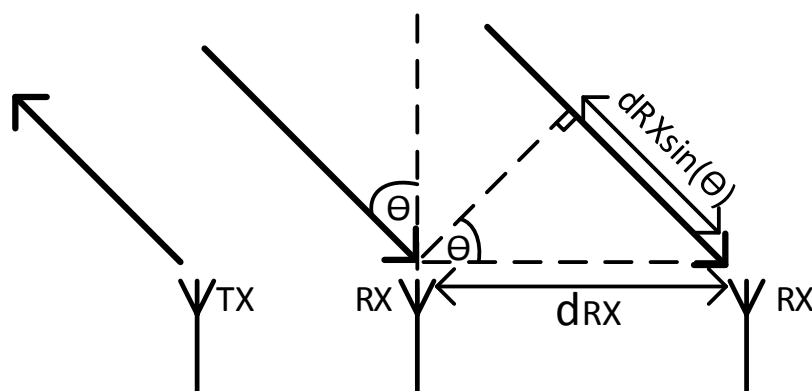


**Figure 2.7:** Single-object AoA estimation. Representation of the AoA ( $\theta$ ) of the reflected signal for the first receiving antenna (RX) and its relationship with the extra distance that this reflected signal has to travel to the second antenna [9].

In Fig. 2.7,  $d_{RX}$  represents the distance between the receiving antennas and  $\theta$  represents the AoA. As we can notice from the diagram, the additional distance ( $\Delta d_{RX}$ ) that the reflected wave must travel to the second antenna is equal to  $d_{RX} \sin(\theta)$ . As a consequence, if we consider that the phase difference between two antennas can be expressed as

$$\Delta\Phi = \frac{2\pi\Delta d_{RX}}{\lambda} = \frac{2\pi d_{RX} \sin(\theta)}{\lambda}, \quad (2.12)$$

then we can calculate the AoA as

$$\theta = \sin^{-1}\left(\frac{\lambda\Delta\Phi}{2\pi d_{RX}}\right). \quad (2.13)$$

To further understand the multiple-object scenario as described in the beginning of this subsection, let us consider two (or more) objects equidistant from the radar with the same relative speed. For this scenario, each peak of the Doppler-FFT will contain phase information of every target. For this reason, in order to resolve and detect every multiple object, a discrete "Angle-FFT" technique needs to be applied over a series of Doppler-FFT peaks that correspond to every  $N_{RX}$  receiver antenna as presented in Fig. 2.8.

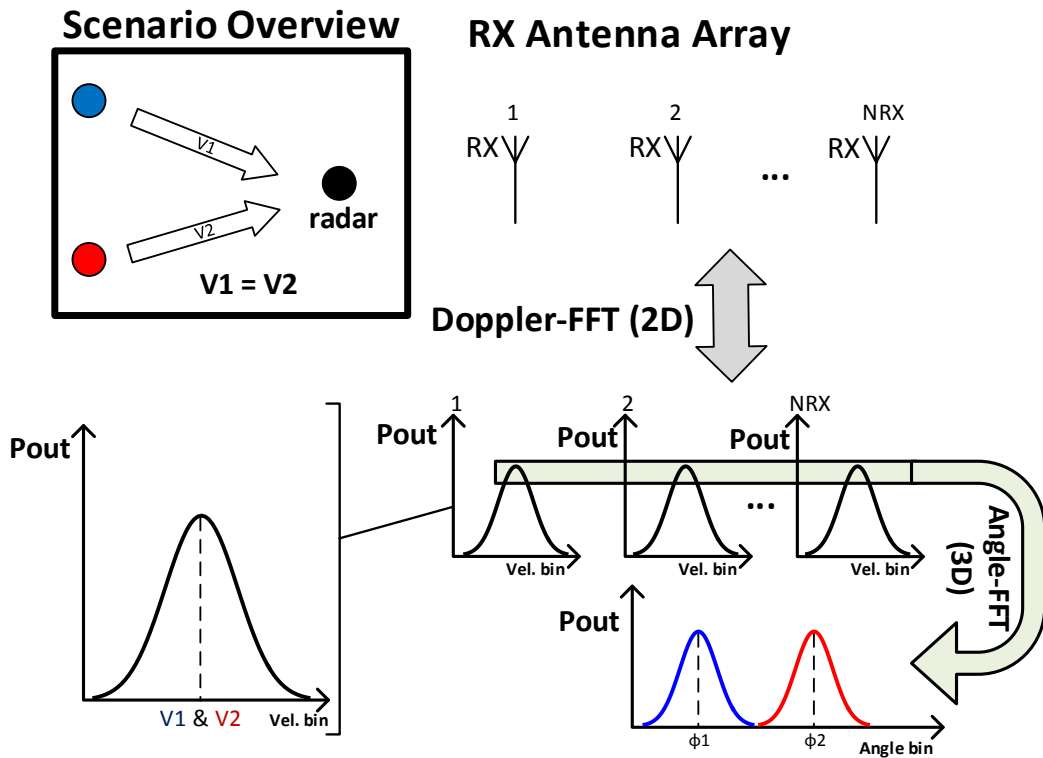


**Figure 2.8:** Multiple-object AoA estimation workflow. For this scenario, the two targets have the same relative velocity [9].

From Fig. 2.8 and considering the results from (2.13), we can express the AoA of every

object as

$$\theta_1 = \sin^{-1} \left( \frac{\lambda \Delta \Phi_1}{2\pi d_{RX}} \right) \parallel \theta_2 = \sin^{-1} \left( \frac{\lambda \Delta \Phi_2}{2\pi d_{RX}} \right), \quad (2.14)$$

with a assumption that the two objects are approaching the radar.

Following the same procedure as the one executed for range and velocity estimation, we will define the angular resolution ( $\theta_{\text{res}}$ ) and the maximum angular value or angular field of view ( $\theta_{\text{max}}$ ). To estimate the angular resolution from two objects with ( $\theta$ ) and ( $\theta + \Delta\theta$ ) AoA, we will use the same constraint as the one applied for velocity resolution and the result from (2.12) to formulate  $\theta_{\text{res}}$  as

$$\begin{aligned} \Delta\Phi &= \frac{2\pi d_{RX}}{\lambda} \cdot (\sin(\theta + \Delta\theta) - \sin\theta) > \frac{2\pi}{N_{RX}} \\ &\frac{2\pi d_{RX}}{\lambda} \cdot \cos(\theta) \Delta\theta > \frac{2\pi}{N_{RX}} \\ \Delta\theta &> \frac{\lambda}{N_{RX} d_{RX} \cos\theta} \\ \Rightarrow \theta_{\text{res}} &= \frac{\lambda}{N_{RX} d_{RX} \cos\theta}, \end{aligned} \quad (2.15)$$

which is inversely proportional to the number of receiver antennas. In a standard FMCW radar design, the separation between the antennas is equal to  $\lambda/2$ . For this reason,  $\theta_{\text{res}}$  can be also expressed as

$$\theta_{\text{res}} = \frac{2}{N_{RX} \cos\theta}. \quad (2.16)$$

On the other hand, the angular field of view can also be estimated using the same criterion as that of the maximum velocity. Therefore,  $\theta_{\text{max}}$  can be expressed as

$$\begin{aligned} \Delta\Phi &= \frac{2\pi d_{RX} \sin(\theta)}{\lambda} < \pi \\ \theta &< \sin^{-1} \left( \frac{\lambda}{2d_{RX}} \right) \\ \Rightarrow \theta_{\text{max}} &= \sin^{-1} \left( \frac{\lambda}{2d_{RX}} \right), \end{aligned} \quad (2.17)$$

which is inversely proportional to the antenna separation. In a standard FMCW radar design, the separation between the antennas is equal to  $\lambda/2$  which results in an angular field of view of  $\pm\pi/2$  radians (azimuth).

### 2.1.4 Summary of Estimation Facts

In Table 2.1, we present a summary of all the relevant facts obtained from the previous subsections. This table will also compare all the characteristics of each estimation category, i.e., range, velocity and angle.

**Table 2.1:** Summary of estimation facts.

|            | Category                       |  |  |
|------------|--------------------------------|--|--|
|            | Range [m]                      | Velocity [m/s]                         | Angle [rad] <sup>1</sup>   |
| Definition | $\frac{c \cdot IF_{tone}}{2S}$ | $\frac{\lambda \Delta \Phi}{4\pi T_c}$ | $\sin^{-1} \left( \frac{\lambda \Delta \Phi}{2\pi d_{RX}} \right)$ |
| Resolution | $\frac{c}{2B}$                 | $\frac{\lambda}{2T_f}$                 | $\frac{2}{N_{RX} \cos \theta}$                                     |
| Maximum    | $\frac{F_s c}{2S}$             | $\frac{\lambda}{4T_c}$                 | $\pm \frac{\pi}{2}$  |

## 2.2 Signal and Target Characterization

In all the previous sections from this chapter, we have discussed about the different target-estimation criteria that can be extracted from the spectral behavior of the received signal. However, in order to have a true measure of the quality of the received signal, the SNR will be introduced in this section in relationship with the antenna parameters and target distance. This evaluation criterion (SNR) will be later proved to be fundamental in the estimation of the RCS, which is considered one of the most common parameters to describe the target.

### 2.2.1 Signal-to-Noise Ratio (SNR)

SNR is a factor that describes the relationship between the power of the received signal to the level of the background noise. This relationship can be expressed as

$$SNR = \frac{P_{\text{signal}}}{P_{\text{noise}}}, \quad (2.18)$$

where  $P_{\text{signal}}$  represents the concentrated power from a single/multiple target and  $P_{\text{noise}}$  represents the concentration of the unwanted power from the background noise. It is important to understand that the background noise can be generally understood as the combination of unwanted or disturbing energy from different type of sources. From all the noise sources, the two most relevant ones are the radar thermal noise and radar clutter. Radar thermal noise (also known as Johnson or Nyquist noise) can be interpreted as a white signal with uniform spectral power density across the entire frequency spectrum. On the other side, radar clutter can be divided into two categories: mainlobe

<sup>1</sup>Angular results for resolution and angular field of view assume a standard separation between the receiving antennas of  $\lambda/2$ .

and sidelobe [12]. Mainlobe clutter is the consequence of unwanted ground returns within the radar beamwidth and sidelobe clutter is the combination of the undesired returns from any other direction outside the mainlobe. Ground return is the most common source of sidelobe clutter due to the high amount of reflective area at close range. Recalling the estimation results from previous chapter, sidelobe clutter will be mainly allocated at short range in the one dimensional profile (range profile) and at the zero frequency in the two dimensional profile (velocity profile).

Once the general description of SNR has been made, it is time to associate this parameter to the analysis of radars in communication systems. For this purpose, it is important to define the radar range equation. Assuming a transmitted power ( $P_t$ ) over a target, the radar range equation [9] [13] can be defined as

$$\begin{aligned} \frac{P_r}{P_t} &= \sigma \cdot \frac{G^2}{4\pi} \left[ \frac{\lambda}{4\pi d^2} \right]^2 = \frac{\sigma G^2 \lambda^2}{(4\pi)^3 d^4} \\ &\Rightarrow P_r = \frac{\sigma P_t G^2 \lambda^2}{(4\pi)^3 d^4}, \end{aligned} \quad (2.19)$$

where  $P_r$  is the received power (also can be interpreted as  $P_{\text{signal}}$ ),  $\sigma$  is the RCS of the target,  $G$  is the antenna gain,  $\lambda$  is the wavelength value and  $d$  is the distance to the target. If we now use the result from (2.18) and if we model the noise power ( $P_{\text{noise}}$ ) as a Nyquist thermal noise expressed as

$$P_{\text{noise}} = k_B T \Delta f, \quad (2.20)$$

where  $k_B$  is the Boltzmann constant,  $T$  is the antenna temperature and  $\Delta f$  is the measured bandwidth, we can rewrite the SNR as

$$\begin{aligned} SNR &= \frac{P_r}{P_{\text{noise}}} = \frac{P_r}{k_B T \Delta f} \\ &\Rightarrow SNR = \frac{\sigma P_t G^2 \lambda^2 T_{\text{meas}}}{(4\pi)^3 d^4 k_B T}, \end{aligned} \quad (2.21)$$

where  $T_{\text{meas}} = 1/\Delta f$  is the measurement period. The result presented in (2.21) will be sufficient if we consider the antenna network and its elements such as attenuators, transmission lines, filters, among others as noise-free. For a complete analysis, consider the antenna as a “lossy” network. For this purpose, the definition of the noise figure ( $F$ ) [14] as the ratio between the input and output SNR is necessary. Considering (2.21) as the input SNR, we can reach a final expression for the output SNR as

$$\begin{aligned} SNR_{\text{out}} &= \frac{SNR_{\text{in}}}{F} \\ &\Rightarrow SNR_{\text{out}} = \frac{\sigma P_t G^2 \lambda^2 T_{\text{meas}}}{(4\pi)^3 d^4 k_B T F}, \end{aligned} \quad (2.22)$$

where  $F$  represents the antenna noise figure.

### 2.2.2 Radar Cross Section (RCS)

RCS, usually represented by  $\sigma$ , is a typical target parameter that describes the spatial distribution of energy that is spread in all directions once the radar wave hits the target. RCS depends on many physical characteristics of the target such as geometry and type of material as well as on radar parameters such as operating frequency and polarization of the incident wave [15]. This parameter is most frequently represented in dBsm (dB relative to one square meter).

The importance in the study of the RCS calculation relies upon the fact that this criterion will provide precise information about the interaction of the target with the incident wave. In the automobile industry, this knowledge opens new opportunities to evaluate, estimate and categorize different types of targets according to their RCS behaviour. For this reason, providing a tool that calculates this parameter for every measured target will not only be able to describe the radar performance but also the target characteristics. Recalling result (2.22), we can define the RCS value as

$$\sigma = \frac{SNR_{\text{out}}(4\pi)^3 d^4 k_B T F}{P_t G^2 \lambda^2 T_{\text{meas}}}, \quad (2.23)$$

which will mainly depend on both antenna parameters and distance to the target. If we now group all the parameters that are due to the antenna and are independent of the measured bandwidth, incident wavelength, and distance to the target, we can define a constant value ( $AP$ ) as

$$AP = \frac{P_t G^2}{k_B T F}, \quad (2.24)$$

which will redefine (2.23) as

$$\sigma = \frac{SNR_{\text{out}}(4\pi)^3 d^4}{\lambda^2 T_{\text{meas}} AP}. \quad (2.25)$$

## 2.3 The CA-CFAR detection

The extraction of target information from pure radar signals is a complex task, due to the uncontrolled and varying noisy environment. In most practical scenarios, the noise power associated with clutter returns is unknown and/or time varying. In such situations, adaptive digital signal processing techniques can be used to remove the noise and to enhance the detectability of targets. These techniques are needed to maintain a constant false alarm rate in a time-varying noise environment. The cell-averaging constant false-alarm rate (CA-CFAR) detection often referred as “*adaptive threshold detection*” or “*automatic detection*”, is a technique developed to provide predictable detection and false alarm behavior in a realistic interference scenario. The CA-CFAR is often used to regulate the false alarm probability to a desired level in varying background environments through energy averaging [16].

In real time, a CA-CFAR detector in a radar system detects targets with varying interference by dynamically adjusting to the detection thresholds in order to maintain a constant design-specific false-alarm rate with a corresponding probability of failure ( $P_{fa}$ ). The  $P_{fa}$

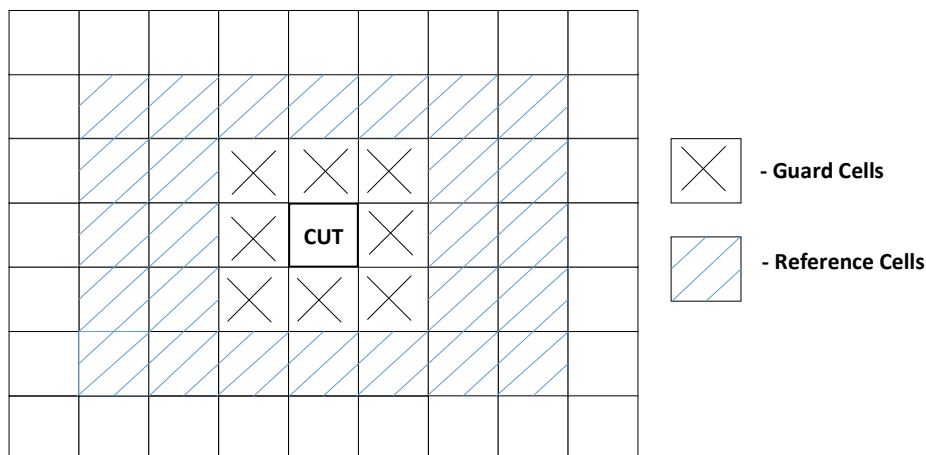
has a value typically no higher than  $10^{-3}$  and very often in the range of  $10^{-6}$  to  $10^{-8}$  [16]. The threshold is determined by estimating the interference around the target. The detector estimates the interference power for a cell under test (CUT) by averaging the sample values of adjacent cells, under the assumption that interference statistics are homogeneous in a localized area [17].

**CA-CFAR Algorithm:** A CFAR window is the set of  $N$  cells around the CUT, that are included in the estimation of the interference power. These cells are known as the reference/training cells. The CFAR window excludes a set of cells immediately adjacent to the CUT (called guard cells), since energy from a target in the CUT might occupy multiple cells around the CUT as well. Hence, energy from the guard cells does not represent interference alone, but would also contain both interference and target energy. The extra energy from the target would tend to raise the detector threshold artificially, if included in the calculation.

The combined reference cells, guard cells and CUT are referred to as the CFAR window [16]. Fig. 2.9 shows the architecture of the CA-CFAR algorithm for one and two dimensional data with the CUT, in the center.



a)



b)

**Figure 2.9:** Architecture of the CA-CFAR algorithm. Figure a) CA-CFAR window for one-dimensional data. Figure b) CA-CFAR window for two-dimensional data [16].

The maximum likelihood estimate for the interference power ( $\widehat{\beta^2}$ ) in a CFAR window consisting of  $N$  cells, is obtained from the average of the available samples, which can be represented as

$$\widehat{\beta^2} = \frac{1}{N} \sum_{i=1}^N x_i. \quad (2.26)$$

The required threshold ( $\widehat{T}$ ), is then calculated as a function of the estimated interference

power and the desired false alarm probability ( $\overline{P}_{fa}$ ) which can be expressed as

$$\hat{T} = \alpha \hat{\beta}^2, \quad (2.27)$$

where  $\alpha$  is defined as

$$\alpha = N(\overline{P}_{fa}^{-\frac{1}{N}} - 1). \quad (2.28)$$

This calculated value of threshold  $\hat{T}$  is then compared to the value of the CUT. If the values of the CUT exceed the computed value, then a target detection is declared.

# 3

## Hardware Tool Chain

The hardware tool-chain setup for capturing the raw ADC data consists of the AWR1243 BoosterPack evaluation board, the mmWave-DevPack and the TSW1400 evaluation module (EVM) provided by Texas Instruments (TI). A detailed explanation of the hardware mentioned above, will be presented throughout this chapter.

### 3.1 AWR1243 BoosterPack

The AWR1243 BoosterPack is an easy-to-use evaluation board for the AWR1243 mmWave high-performance front-end. It enables raw capturing of the ADC data from the front-end and the evaluation of the RF-performance.

Fig. 3.1 shows the front and rear views of the evaluation board, respectively.

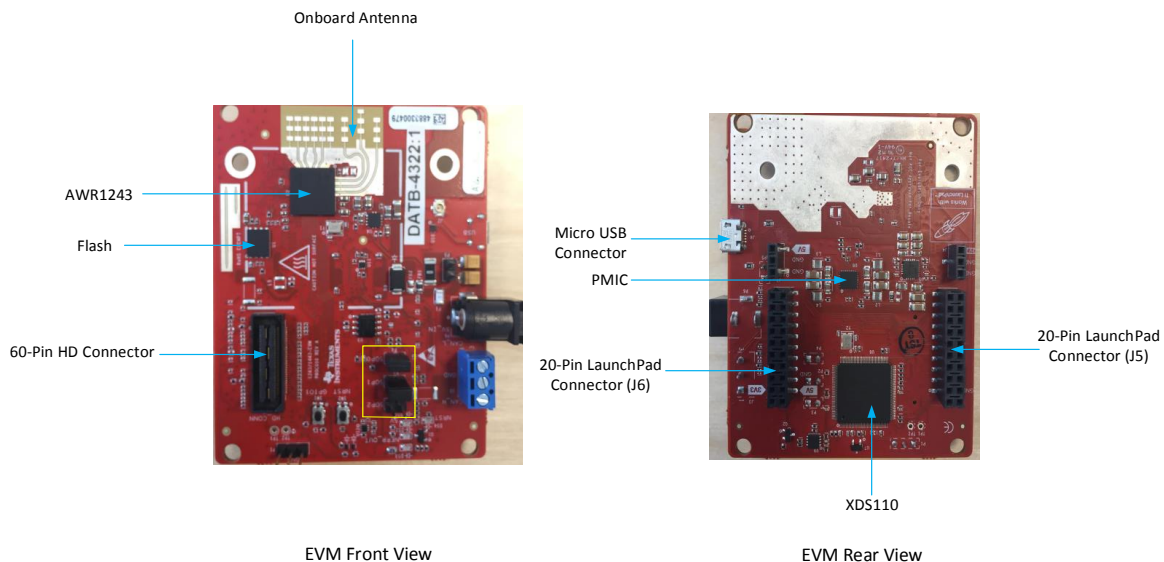


**Figure 3.1:** BoostPack front and rear view.

Some of the key features from the board are [18]:

- 40-pin launchPad connectors (J5 and J6), which enables the BoosterPack to be directly connected to the Devpack.

- 60-pin high density (HD) connector for raw ADC data transfer over camera serial interface (CSI) or any of the high-speed debug interface and controls signals (SPI, UART, I2C, SOPs). This connector is connected to the DevPack board and interface with the TSW1400 EVM.
- On board antenna and 5 V power jack to power the board. The BoostPack includes onboard-etched antennas for the four receiver and three transmitter channels in order to enable the tracking of multiple objects with their respective distance, and velocity information. This design also enables the estimation of both azimuth and elevation angles.
- Sense on power jumpers: Sense on power (SOP) lines are sensed only during the boot up of the AWR1243 device. The device can be set to operate in three different modes based on the state of the SOP lines. The state of the device is illustrated in Table 3.1.

**Table 3.1:** SOP modes.

| Use      | Reference | Comments                             |
|----------|-----------|--------------------------------------|
| SOP[2:0] | SOP2      | 101 (SOP mode 5) = Flash programming |
|          | SOP1      | 001 (SOP mode 4) = Functional mode   |
|          | SOP0      | 011 (SOP mode 2) = Dev mode          |

- TI provides a mmWave-device firmware package (DFP) i.e., DFP for the boostpack to have seamless control and configuration of the device, which will be explained on detail in Chapter 4.

**AWR1243 FMCW transceiver:** The BoosterPack consists of the AWR1243 mmWave sensing module, which is a self-contained FMCW transceiver in a single chip belonging to the TI family of [76-81] GHz radar band. This sensor module is compact and has a high-performance front-end, which supports fast-chirp FMCW modulations from a closed-loop frequency synthesizer featuring a wide-IF bandwidth complex baseband. This sensor uses electromagnetic waves in the [76-81] GHz frequency to determine the radial distance (range) to the object, relative radial velocity to the object, and the AoA using multiple transmitters (TX), receivers (RX) [19].

Some key characteristics of the AWR1243 sensors are:

- AWR1243 sensors are capable of providing a maximum of 4 GHz sweep bandwidth.
- The sensor module supports ramp slopes up to 100 MHz/ $\mu$ s and an IF bandwidth up to 15 MHz.
- The device supports a maximum sampling rate up to 37.5 Msps.
- The device includes a synchronization feature, which enables the cascading of multiple devices on a single printed circuit board (PCB) in order to create large coherent arrays for high-resolution processing.

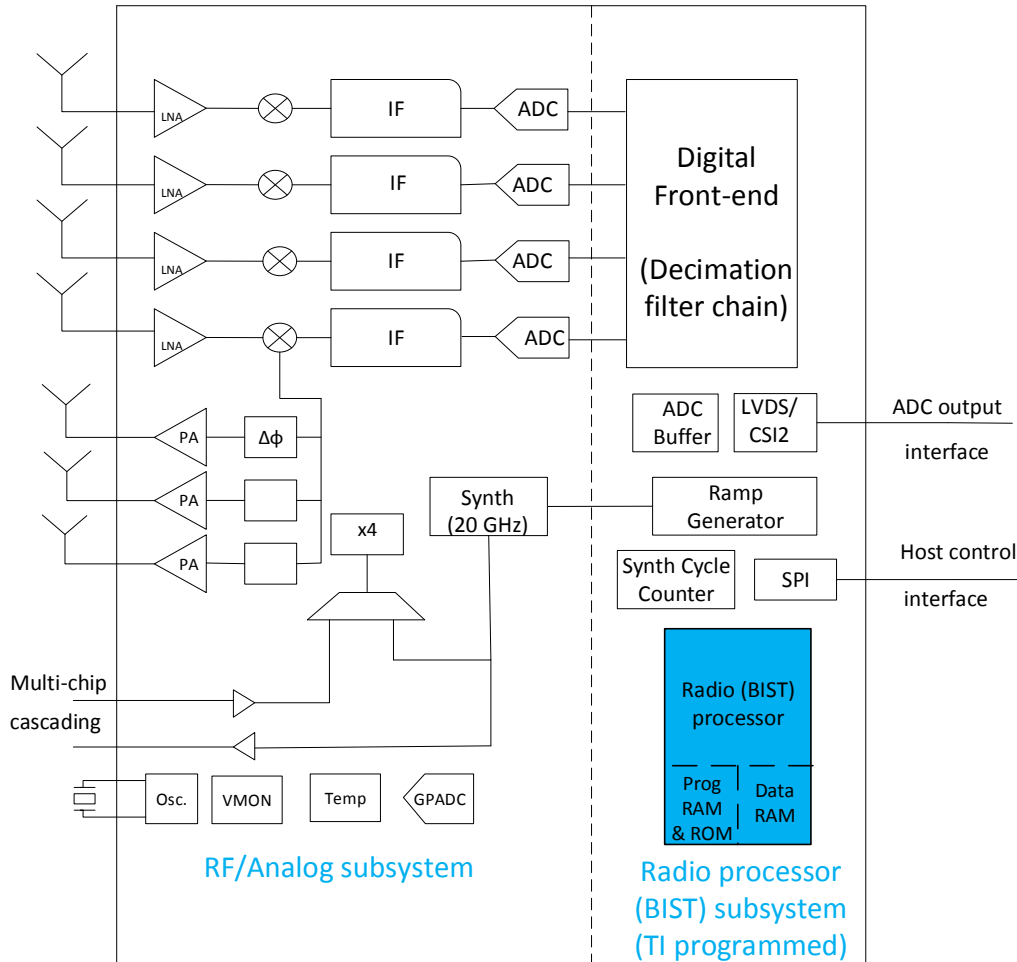


**Figure 3.2:** AWR1243 mmWave intelligent front-end sensor [19].

Fig. 3.2 depicts the block diagram of the AWR1243 sensor which consists of a RF/analog subsystem, clock subsystem and a radio processor subsystem. The RF/analog subsystem includes the analog sub-circuitry namely, the synthesizer, three transmit channels and four receiver channels in a single chip [20]. This subsystem also includes a crystal oscillator and temperature sensors. Each of the transmit channel includes an independent binary phase modulator and a variable-gain power amplifier with a simple single-ended output with a direct interface to an antenna. The receiver channels includes mixers, LNAs, and a complex baseband with a 15 MHz IF bandwidth. The continuous time sigma-delta ADC digitizes the analog signals, and the digital front-end provides decimation and signal conditioning [19] [20].

A maximum of two transmit channels can be operated simultaneously, whereas all the four receiver channels can be operated at the same time. The AWR1243 device supports a complex-baseband architecture, which makes use of a quadrature mixer and dual IF with ADC chains providing complex I and Q outputs for each receiver channel [20].

The clock subsystem generates [76-81] GHz from an input reference of 40 MHz crystal. It consists of an in-built oscillator circuit followed by a clean-up phase-locked loop (PLL) and an RF synthesizer circuit. The output from the RF synthesizer circuit is then processed by an X4 multiplier to create the required frequency in the range of [76-81] GHz spectrum [20].

The radio processor subsystem part of the device includes an internal processor known as the built-in self-test (BIST) processor, a ramp generator for flexible real-time operation and other associated peripherals and interfaces [19]. The most important characteristics of the radio processor subsystem are:

- The BIST processor is responsible for configuring the RF/analog and digital front-ends in real time, as well as to periodically schedule the calibration and functional-safety monitoring. This periodic task enables the mmWave front-end to be self-contained and capable of adapting itself to different temperatures and aging effects.
- The ramp generator provides flexible chirp generation with 512 unique chirps following four different chirp profiles that can be pre-configured. Thus, eliminating any need for real-time control within the active radar operation period.
- The primary interface is over the CSI, which is usually used to have connection with an external DSP. However, low-voltage differential signalling (LVDS) is also available as a debug interface, which is mainly used for raw-data capturing and recording. The device can communicate with the external host processor using the serial peripheral interface (SPI). Hence, the external host processor can be used to configure and control the device by sending the commands to it over the SPI interface.

## 3.2 mmWave-DevPack

The mmWave-DevPack is an add-on board used with TI-mmWave sensor EVMs such as the AWR1243BOOST to increase the number of serial interfaces and PC connectivity to the mmWave sensor EVMs. It also provides an interface for the Radar Studio tool (part of the DFP firmware package), which is explained in Chapter 4, to configure the radar device and capture the raw ADC data using the TSW1400 EVM. There is an on-board low dropout (LDO) voltage regulator, which is enabled only when the BoosterPack (connected to the DevPack) is powered. This feature mainly prevents the DevPack from powering up before the BoosterPack [21].

Some of the key features of the board interfaces are [21]:

- Powered over a micro universal serial bus (USB) connector and has a 20-pin launchPad connectors for all the digital controls from the AWR1243BOOST.
- 120-pin connector to interface with the TSW1400 EVM.
- 60-pin HD connector for a high-speed ADC data transfer over the CSI or LVDS interface and emulator signals from the BoosterPack.

## 3.3 TSW1400 EVM

The TSW1400 EVM is a complete pattern-generator and data-capture circuit board, which is specifically designed to evaluate most of TI's high-speed ADC and digital-to-analog converter (DAC). The device provides two direct interfaces to TI ADC EVMs. For the first type of interface, the data is captured through a high-speed LVDS bus capable of providing 16 bits of data at 1.5 Gsps (Giga samples per second) and the other uses a dual 16-bit complementary metal-oxide-semiconductor (CMOS) interface that will be enabled

in a future firmware upgrade [22].

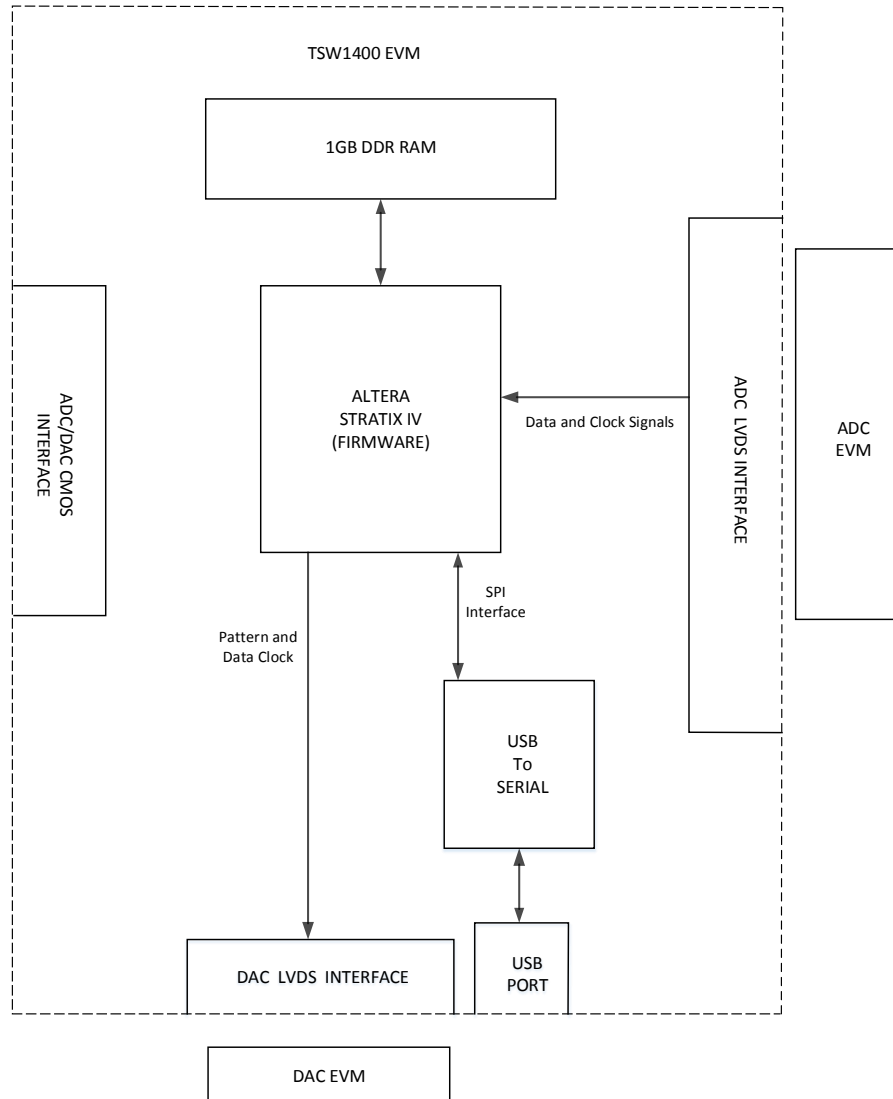


**Figure 3.3:** TSW1400 EVM Block Diagram [22].

Fig. 3.3 illustrates the block diagram of the TSW1400 EVM module. The board comes with a 1 GB-DDR memory card. Sampled data from the ADC interface is de-serialized and formatted by an Altera Stratix IV FPGA, which stores the sampled data into the board DDR memory module. This on-board memory enables the TSW1400 EVM to store up to 512 MB of 16-bit data samples. Due to the limitation of this on-board memory, the TSW1400 EVM can capture frames from the radar module only for a maximum of 10 seconds. Hence the total period of data capture ( $Frame_{periodicity} \cdot No_{frames} < 10$ ) seconds.

The FPGA can read the data from on-board memory and transmit it over SPI bus. Hence, the captured data can be acquired on a host PC by using an on-board high speed USB to SPI converter that bridges the FPGA-SPI interface to the host PC and graphical user interface (GUI) [22]. This GUI provided by TI, high speed data converter (HSDC) Pro, supports the testing of all TI high speed data converter EVMs which are explained in detail in Chapter 4.

The TSW1400 EVM can be also used for pattern generation. In this mode, the device generates the desired test patterns for a DAC EVM under test. These patterns are sent from the host PC over the USB-interface to the TSW1400 EVM. The FPGA stores the received data into the DDR memory card. The data from this on-board memory is then read to be transmitted to a DAC EVM either across a LVDS interface or a CMOS interface connector [22]. The hardware connection between the components for capturing and extracting the ADC data is explained in Appendix A.

# 4

## Software and Tools

In order to configure the complete hardware tool-chain from the radar module up to the raw ADC data capturing, specific device firmware packages and GUIs must be used. In this chapter, these software tools are introduced followed by a detailed explanation on the FMCW chirp and frame structure to be used in this thesis work. Finally, this chapter concludes with the illustration of the format in which the raw ADC data is captured depending on factors like sampling type (real or complex), number of receiver antennas ( $N_{RX}$ ), among others.

### 4.1 Firmware and GUI

For the configuration of the radar module, as per the user requirements, and to capture the raw ADC data for post-processing purposes, the firmware and GUIs that are used in this thesis work are explained in this section of the chapter.

#### 4.1.1 DFP Firmware Package

The DFP package provides seamless control, configuration, calibration, and monitoring capabilities for the RF/analog and digital front-end subsystem of the AWR1243 radar module. It also enables the mmWave front-end to adapt itself to some dynamic conditions such as temperature. The main features of the DFP package include:

- Easy and flexible configuration of the RF/analog subsystem.
- Built-in calibration and monitoring capabilities.
- Seamless control and communication using well defined abstracted APIs.
- Master subsystem (MSS) firmware is included as a part of the package, which in turn consists of core system drivers, peripheral device drivers, and system/control services.
- Provides a GUI tool known as Radar Studio to control and configure the mmWave front-end. This tool also enables the post-processing and visualization of the raw ADC radar data.

#### 4.1.2 Radar Studio

The Radar Studio tool is mainly designed for testing and to communicate with TI radar devices. This tool is mainly used for characterization and system evaluation. The main

functionality of the tool includes: configuration and control of the mmWave device by sending commands over SPI. The raw ADC data is then captured using the TSW1400 EVM module and this data is post-processed using a MATLAB runtime environment to visualize the results that are displayed on the GUI [23].

Radar Studio utilizes C-based DLLs and a set of APIs to communicate from the GUI to the radar device. This communication is executed through a future technology devices internal (FTDI) FT4232H interface. The FT4232H is a 2.0 hi-speed USB (480 Mbps) to UART IC featuring 4-UART ports [23].

Some key features of this software are [23]:

- Offers radar board control i.e., SOP change and reset control.
- Flash programming.
- RS232 connection to device and firmware download capability.
- SPI connection to issue radar API commands.
- Interaction with the TSW1400 EVM and the HSDC pro GUI.
- Support for the post-processing of the captured raw ADC data.

### 4.1.3 HSDC Pro

The HSDC Pro GUI supports testing of the AWR1243 sensor module connected to the Devpack, while using with the TSW1400 EVM. The high speed data from the LVDS interface is captured and stored directly inside the FPGA DDR memory card, which is then transmitted over SPI. As a consequence, the captured data can be acquired on a host PC. HSDC Pro utilizes a DLL and a set of APIs to communicate from the GUI to the TSW1400 EVM utilizing a FTDI FT4232H device [24]. The GUI provides an option to store the captured raw ADC data either as a 32 signed integer (I32) *.csv* or as a binary *.bin* file.

Some key features of this software are [24]:

- Continuous data capture.
- External trigger capability.
- Master and slave operation.
- Frequency and time analysis.
- Saving and exporting the captured data into separate files for post-processing purposes.

## 4.2 FMCW Chirp and Frame Structure

The AWR1243 device enables the configuration of chirp parameters in a frame by defining it in terms of chirp profiles. Chirp profiles are basic chirp timing templates which are useful to have significant variance in one or more different chirp parameters (e.g., start frequency, slope, idle time, and so on). The radar device supports up to four different chirp profiles. Each chirp definition entry in the RAM memory belongs to one of the four chirp profiles.

Therefore, up to 512 unique chirps per profile can be pre-programmed and stored in the chirp configuration RAM. Thus, a frame consists of sequence of chirps from a start-index to an end-index in the chirp configuration RAM which can be looped for a maximum of 255 times [25]. Fig. 4.1 illustrates a single chirp with its associated parameters and a frame structure that consists of a series of chirps followed by an inter-frame time.

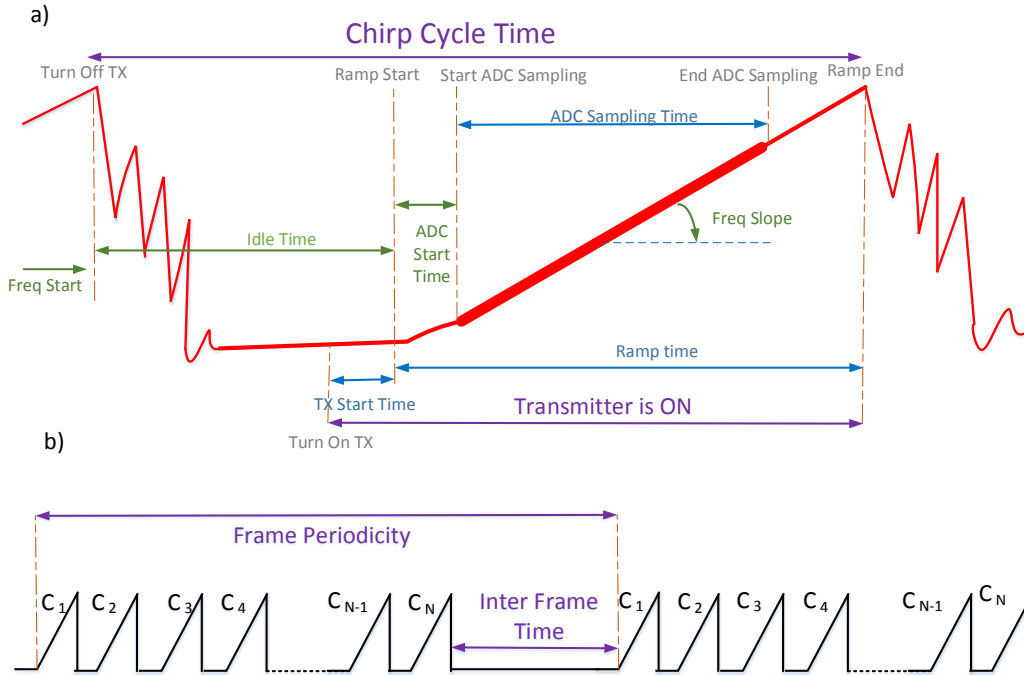


**Figure 4.1:** FMCW Chirp and Frame structure [25]. Figure a) shows a typical FMCW chirp. Figure b) shows a typical frame structure.

The chirp parameters that are controllable per profile are [25]:

1. **Idle time:** The time duration between the end of the previous chirp and the start of next chirp. The minimum value required for the idle time is mainly determined by the synthesizer ramp-down settling time, which is a function of ramp-down bandwidth.
2. **ADC Start Time:** The time from the start of the ramp in which the ADC starts sampling the data.
3. **Ramp Time:** The total time allocated for the frequency ramp. After this time, the synthesizer frequency is reset to the start frequency of the next chirp. In other words, the ramp time is the sum of (a) the ADC start time, (b) the ADC sampling time and (c) the excess-ramp time at the end of the ramp. There is no hard requirement on the excess-ramp time.

### 4.3 Raw ADC Data Format

Once the raw ADC data is captured and stored on the host PC (either on a *.bin* or a *.csv* file), it is important to understand how this data is structured for a righteous post-processing development. For this purpose, Fig. 4.2 illustrates the format in which

the data will be stored per frame on a complete 4-receivers (RX) with 4-active-LVDS lanes scenario. Understanding the format of the incoming raw ADC data is a key step to develop the DSP algorithms in MATLAB for several reasons. Initially, the raw data should be evaluated differently depending on the sampling type (real or complex). In addition, it is important to understand the size and the distribution of the samples so they can be divided per frame and per chirp, since the frequency analysis is done over chirps. For illustration purposes, each frame is assumed to have a general structure of  $M$ -chirps containing  $N$ -samples per chirp.

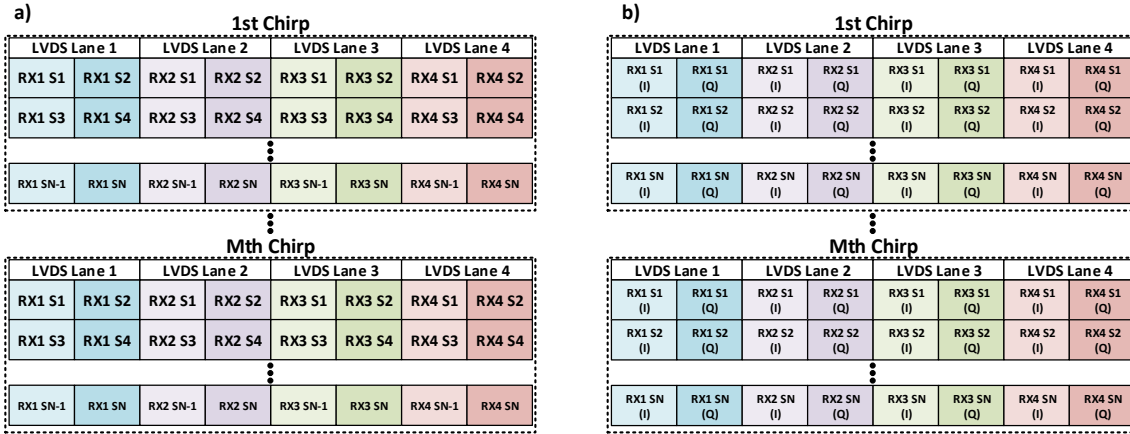


**Figure 4.2:** Raw ADC data format. Figure a) shows a format for real data capture. Figure b) shows a complex data capture format.

It is important to mention that each captured sample (represented by every individual box on Fig. 4.2) is two bytes long (16-bit). It is also clear from the diagram that the main difference between the real and complex case format is on the distribution of samples per LVDS lane. For the real format, each LVDS lane contains two samples of one receiver (e.g., RX S1 and RX S2). On the other hand, in the complex format, each LVDS lane contains only one sample of one receiver (e.g., RX S1(I) and RX S1(Q)). This is due to the fact that each sample is divided on its in-phase (I) and quadrature (Q) part.

To accurately post-process the data, we must separate the samples per receiver (RX) and organize them together either on a column or row wise format. For this reason, for the real data format, we will transpose the input matrix and interleave the incoming samples to obtain the final matrix as presented in Fig. 4.3. On the other hand, for the complex data format, we will transpose the input matrix and combine the input samples in order to obtain the same final matrix as presented in Fig. 4.3.

**Frame**

|        |        |        |        |     |          |        |          |          |     |               |             |
|--------|--------|--------|--------|-----|----------|--------|----------|----------|-----|---------------|-------------|
| RX1 S1 | RX1 S2 | RX1 S3 | RX1 S4 | ... | RX1 SN-1 | RX1 SN | RX1 SN+1 | RX1 SN+2 | ... | RX1 S (M*N)-1 | RX1 S (M*N) |
| RX2 S1 | RX2 S2 | RX2 S3 | RX2 S4 | ... | RX2 SN-1 | RX2 SN | RX2 SN+1 | RX2 SN+2 | ... | RX2 S (M*N)-1 | RX2 S (M*N) |
| RX3 S1 | RX3 S2 | RX3 S3 | RX3 S4 | ... | RX3 SN-1 | RX3 SN | RX3 SN+1 | RX3 SN+2 | ... | RX3 S (M*N)-1 | RX3 S (M*N) |
| RX4 S1 | RX4 S2 | RX4 S3 | RX4 S4 | ... | RX4 SN-1 | RX4 SN | RX4 SN+1 | RX4 SN+2 | ... | RX4 S (M*N)-1 | RX4 S (M*N) |

**Figure 4.3:** Raw ADC final matrix.

Recall that, for the complex data format, each sample of the final matrix in Fig. 4.3 is the result of the combination of the in-phase (I) and quadrature (Q) part as  $\text{Complex}_{\text{Sample}} = I + jQ$ .

# 5

## System Implementation

So far we have introduced a wide theoretical background that covers the complete functionality of the FMCW radar. In addition, a detailed explanation on all the SW and HW tools that were used in this thesis project were also illustrated in previous chapters in order to capture the raw ADC data from the radar module for post-processing purposes. This chapter will mainly cover two important topics that will clarify the methodology used in this thesis project. First, all the MATLAB-based post-processing algorithms will be introduced to describe the DSP methods. Second, an illustration of all the HW test-scenarios is presented in order to constitute a referential ground-truth data for the future analysis of results.

### 5.1 MATLAB Post-Processing

All the following MATLAB post-processing algorithms are based on the theoretical background described in Chapter 2, which is summarized in Table 2.1. It is important to emphasize that every algorithm flowchart assumes an appropriate raw ADC input-file reading and, depending on the data format (real or complex), will contain an starting raw ADC data matrix as the one presented in Fig. 4.3.

#### 5.1.1 DSP-IP Block Overview

Fig.5.1 represents the block diagram of the entire DSP algorithm based on MATLAB. The algorithm is mainly divided into three sub-blocks, namely

1. **Target detection part:** This stage consists of the range-processing block, Doppler-processing block and AoA estimation block. The AoA block is further used to compute the lateral distance of the target with respect to radar.
2. **Adaptive signal processing:** This section of the module mainly deals with the filtering of noise and clutter by making use of the CA-CFAR algorithm. The peak of signal energy is also computed in this stage, which later aids in the calculation of SNR, RCS, and lateral distance.
3. **Evaluation module:** This module describes the radar performance while exploiting the characteristics of target. The algorithm for estimation and categorization of target is implemented in this module.

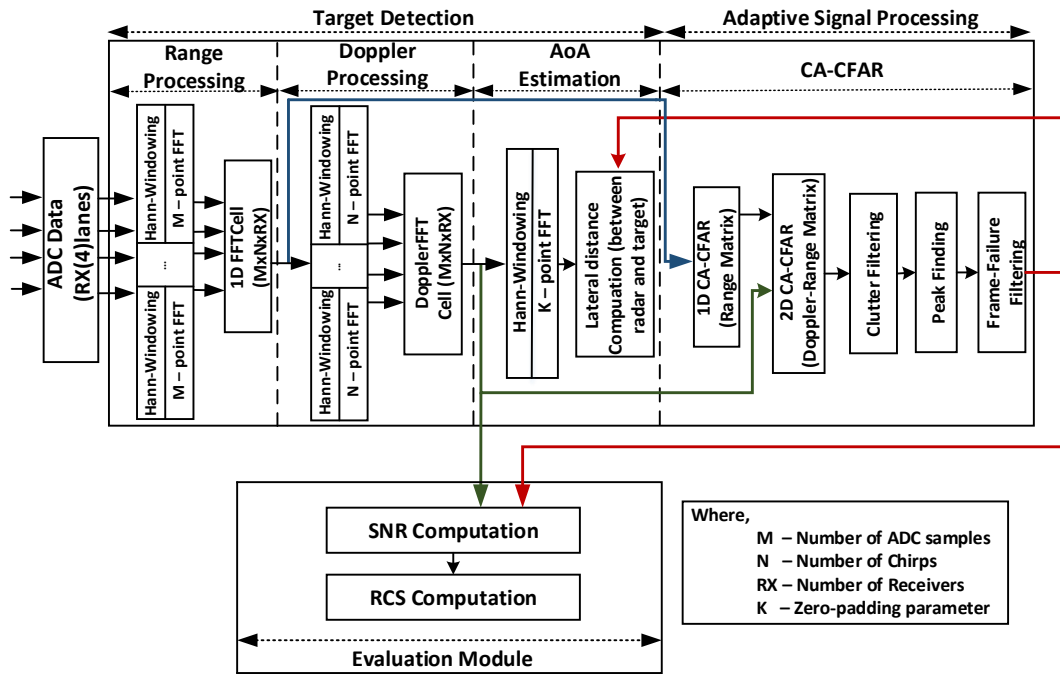


Figure 5.1: General block diagram for the main DSP algorithm implementation.

A detailed explanation on the implementation of every sub-block will be explained throughout the following sections within this chapter.

### 5.1.2 Range Estimation (1D-FFT)

The flowchart diagram introduced in Fig. 5.2 summarizes the implemented algorithm for range profile estimation.

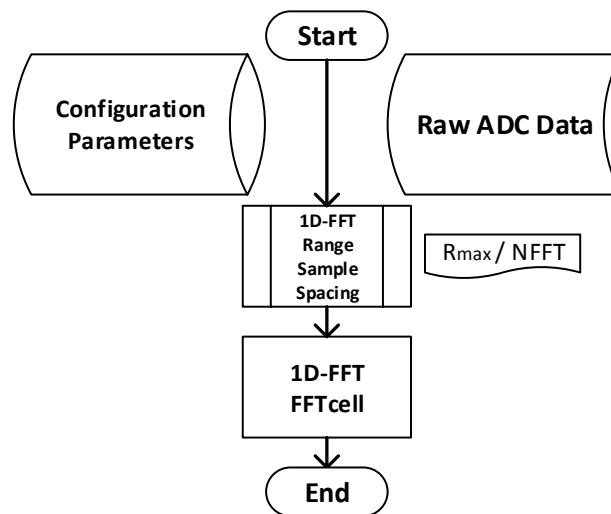
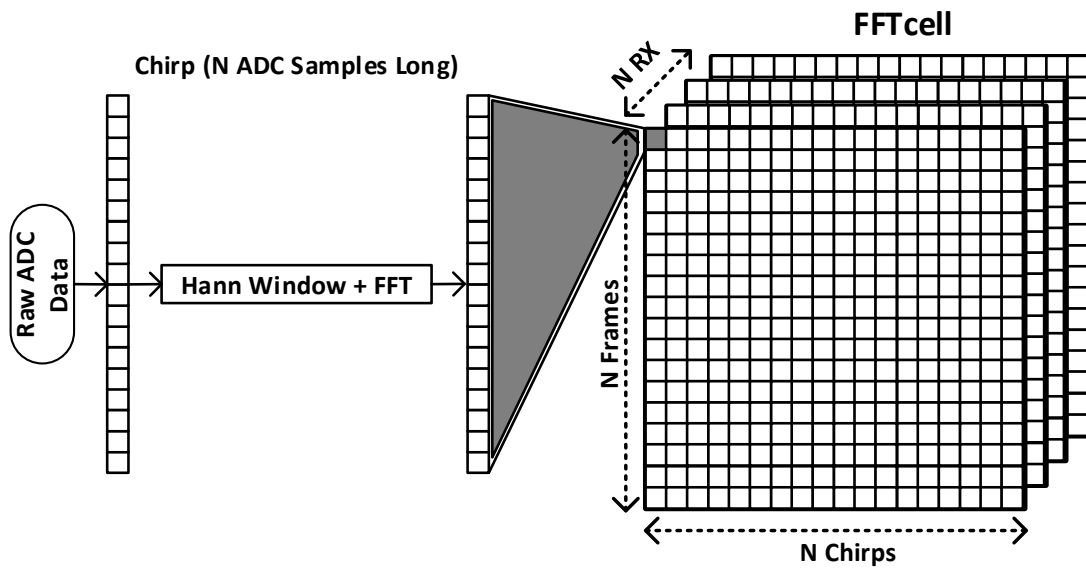


Figure 5.2: Range FFT (1D) algorithm flowchart.

The algorithm presented in Fig. 5.2 contains several stages which are executed to obtain the 1D FFT results for target-range estimation. Initially, the algorithm will extract the global variables that correspond to the raw ADC captured data, FMCW chirp, and frame configuration as pre-defined by the user. Subsequently, the range-bin space vector is defined to map the FFT samples into a physical spacial domain (range). This range-bin vector is computed using the maximum range distance definition (2.5) and distributing its value into the total number of ADC samples. Finally, the FFT transformation is applied to every sample vector that constitutes every chirp allocated inside every frame. To make this procedure more clear, the diagram shown in Fig. 5.3 will illustrate this operation.



**Figure 5.3:** Range FFT (1D) core operation.

Fig. 5.3 illustrates the concept of range-FFT. As presented in the diagram, every chirp is extracted from the raw ADC data set in a form of a vector. This vector is then passed through a windowing and FFT transformation that will result in a vector of the same length (number of ADC samples long). The result for every chirp is then stored in an individual cell of a cell-type variable called FFTcell. This procedure is performed for every frame that corresponds to every receiver (RX). The information is then separated by receiver (RX), resulting in a multidimensional cell as presented in the diagram.

### 5.1.3 Velocity Estimation (2D-FFT)

The flowchart diagram introduced in Fig. 5.4 summarizes the implemented algorithm for range-velocity (Doppler FFT) profile estimation.

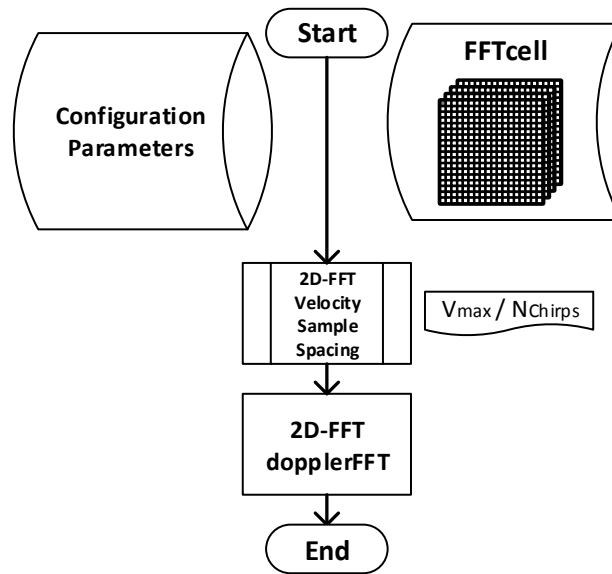


**Figure 5.4:** Range-Doppler FFT (2D) algorithm flowchart.

The algorithm presented in Fig. 5.4 presents a similar structure as for the 1D range profile. The main difference now is that this algorithm will start with the pre-defined configuration parameters and the FFTcell variable, which contains the results for the range estimation. Latterly, the velocity-bin space vector is defined using the maximum velocity definition (2.11) and then dividing its value into the total number of chirps per frame. This velocity-space vector will be later used to map the 2D FFT results into a physical domain (velocity). Finally, the FFT transformation is applied across the chirps of every frame allocated inside every receiver (RX). To make this procedure more visible, the diagram in Fig. 5.5 will illustrate this operation.

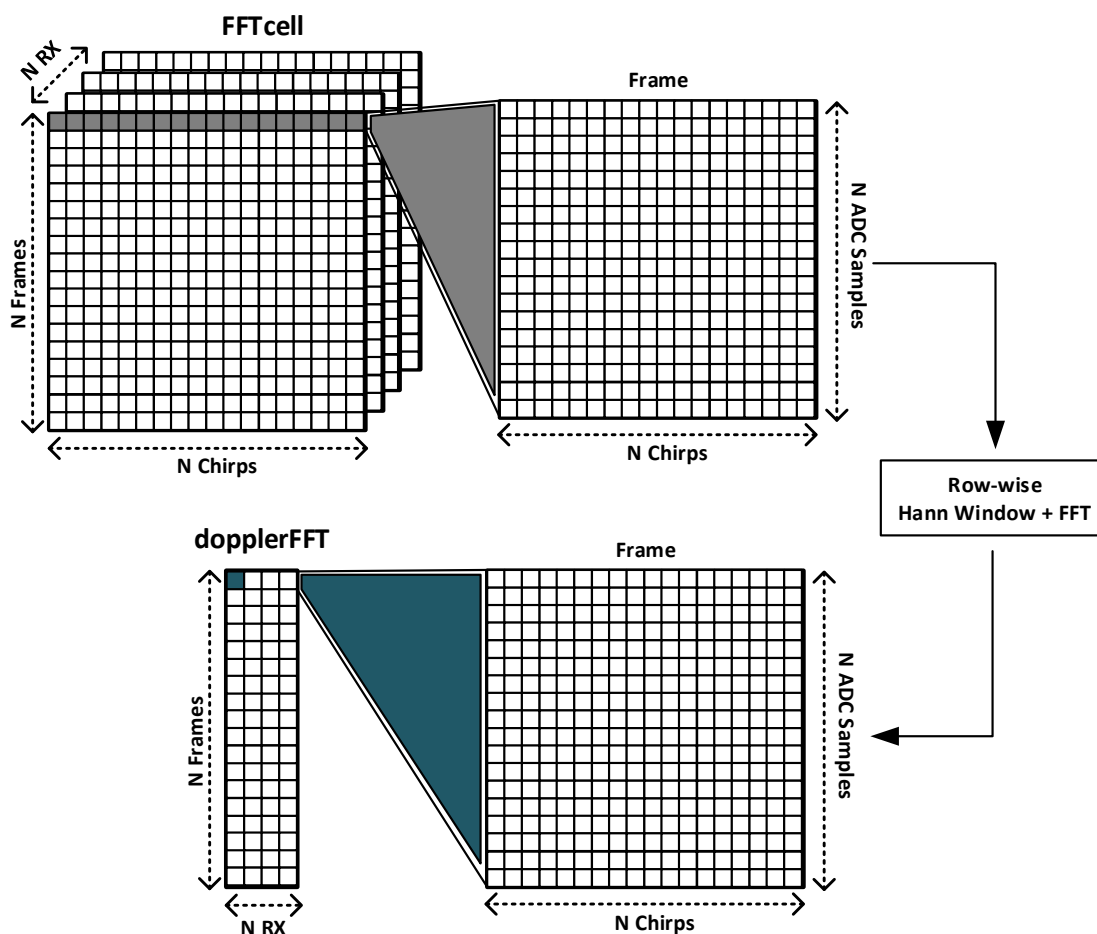


**Figure 5.5:** Range-Doppler FFT (2D) core operation.

Fig. 5.5 illustrates the concept of range-Doppler FFT. As seen in the figure, every frame of each receiver (RX) is extracted from the FFTcell variable. This matrix is then passed through a row-wise windowing and FFT transformation. This procedure will result in a matrix with the same dimensions. It is important to emphasize here that the windowing and FFT function are performed row-wise since we want to exploit the phase difference between chirps within the same frame. Every result for each frame is then stored in an individual cell of a cell-type variable called DopplerFFT. This procedure is performed for every frame that corresponds to every receiver (RX). The information is then separated (column wise) per receiver (RX), resulting in a two dimensional cell as presented in the diagram.

#### 5.1.4 Angle Estimation (3D-FFT)

The flowchart diagram introduced in Fig. 5.6 summarizes the implemented algorithm for the Angle FFT profile estimation.

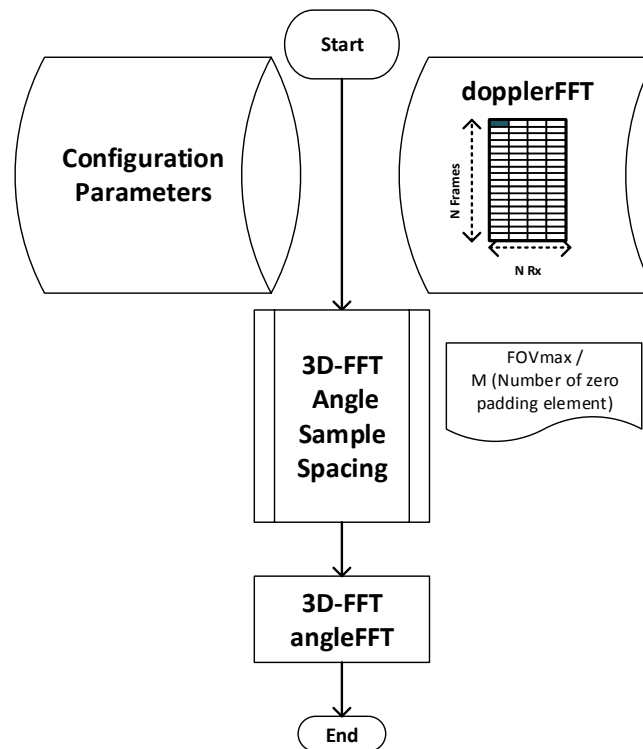


**Figure 5.6:** Angle FFT (3D) algorithm flowchart.

The algorithm presented in Fig. 5.6 contains a similar structure as for the 2D range-Doppler profile. However, one of the differences now is that this algorithm will start with the DopplerFFT variable, which contains the result for the range-Doppler estimation. Following this, the angle-bin space vector is obtained by dividing the maximum field of view as given by the definition (2.17) by the total number of zero-padded elements from the angular dimension (from the 3D FFT). This angular-bin vector will be later used to map the 3D FFT results into the physical domain (AoA). Finally, the FFT transformation is applied across pages for the total number of receivers (RX channels). The resultant matrix obtained is expanded by a factor equal to total number of zero-padded elements. A clear illustration of this procedure is demonstrated in Fig. 5.7.

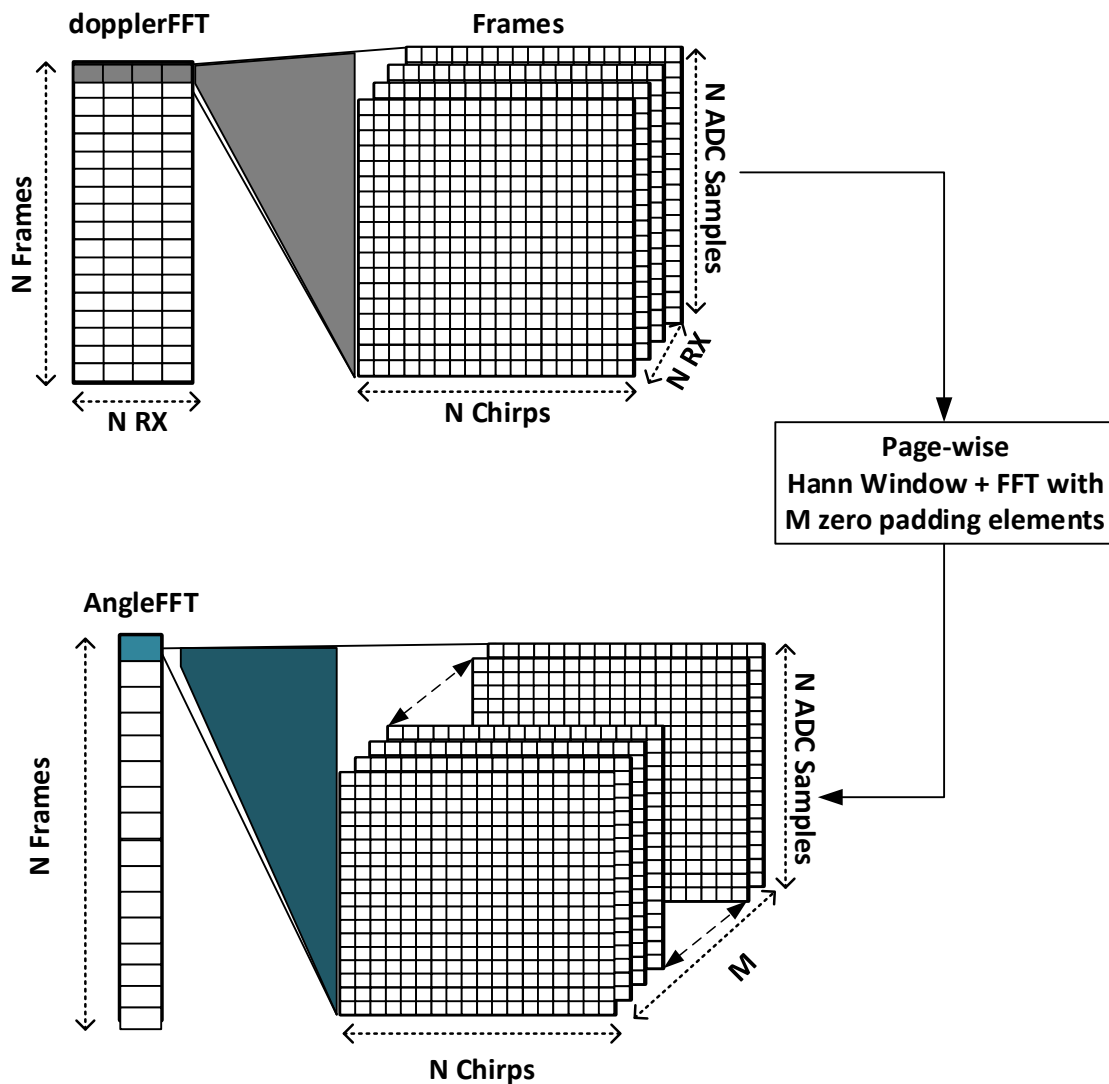


**Figure 5.7:** Angle FFT (3D) core operation.

As seen from the figure, for each frame, the range-Doppler matrix from all the four receivers is combined in a single matrix. This combination results in a 3D-matrix ( $Range \times Doppler \times N_{\text{Receivers}}$ ). After generating the 3D matrix, page-wise windowing is applied throughout the matrix. The FFT procedure is now applied across the receivers i.e., pages and the result is expanded by zero padding. The resulting matrix third dimension size ( $M$ ) is determined by a certain number which is user configurable. In our implementation, we have chosen to zero-pad the matrix by 100 times i.e.,  $M = 100$ . This is done in order to have a better mapping of the 3D FFT results into the physical domain (AoA). It is also important to note that, the windowing and FFT function are performed page-wise. This is because we want to exploit the phase difference between the receivers to estimate the AoA. The resultant zero padded matrix is then stored column-wise for every frame, resulting in a one-dimensional cell known as AngleFFT as presented in the diagram.

### 5.1.5 Lateral Distance Estimation

Fig. 5.8 contains the flowchart of the algorithm to compute the lateral distance of the target with respect to the radar.

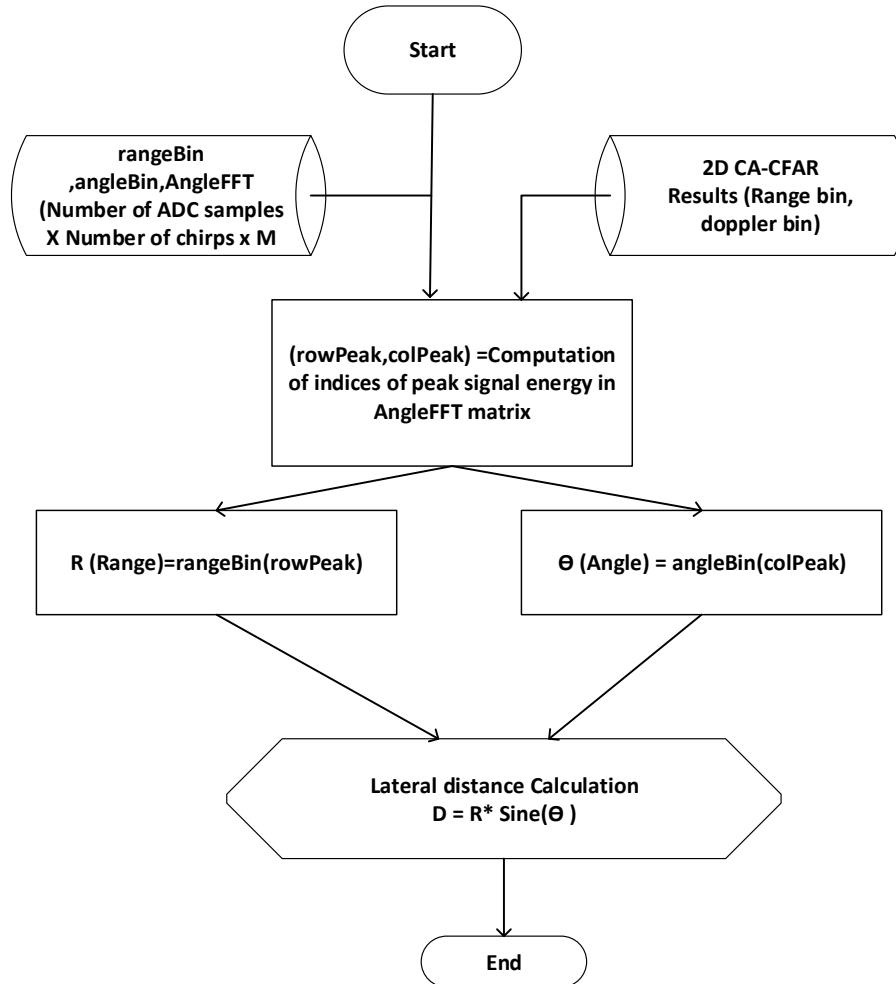


**Figure 5.8:** Lateral distance estimation algorithm flowchart.

The algorithm presented in Fig. 5.8, mainly takes the output matrices from the angle estimation results such as AngleFFT and angleBin (angular bin vector) as the input parameters. Additionally, it also takes the rangeBin (range bin vector) and the 2D CA-CFAR result profiles as the input parameters. With all of these available input parameters, the algorithm computes the bin-indexes of the highest peak signal energy in the AngleFFT matrix, which corresponds to the detected target. The range ( $R$ ) and AoA ( $\theta$ ) of the target with respect to radar is then calculated by mapping the computed indices to the rangeBin and angleBin profiles respectively.

The lateral distance computation can be derived using Fig. 5.9 as reference.

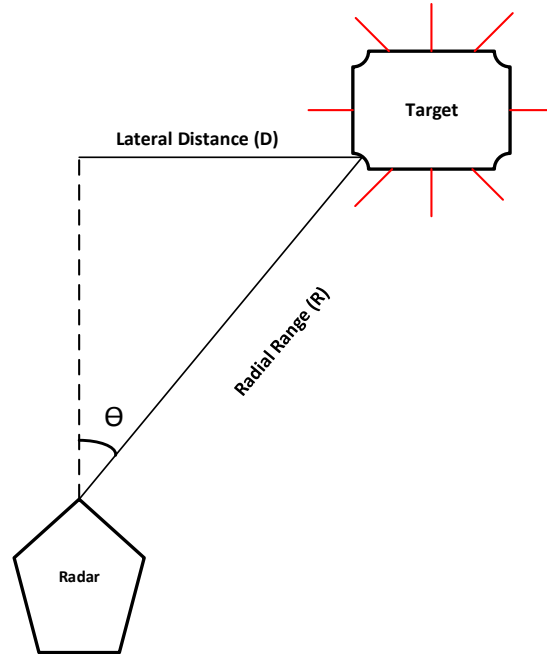


**Figure 5.9:** Mathematical overview of the lateral distance estimation.

As we can observe from Fig. 5.9, the lateral distance ( $D$ ) can be mathematically derived as

$$\sin(\theta) = \frac{\text{Lateral Distance}(D)}{\text{Radial Range}(R)} \quad (5.1)$$

$$\text{Lateral Distance}(D) = \text{Radial Range}(R) * \sin(\theta).$$

### 5.1.6 1D and 2D CA-CFAR

Fig. 5.10 shows the flowchart of the 1D CA-CFAR algorithm implementation. The algorithm initiates by taking results from the 1D FFT matrix as the input. The defined size of the CA-CFAR window is a user configurable, one-dimensional (e.g.,  $Guard_{size} = 3 || Train_{size} = 32$ ) sliding window. The scaling factor  $\alpha$ , is calculated in accordance with the definition (2.28), where  $\bar{P}_{fa}$  is set to  $10^{-8}$ . The 1D CA-CFAR windowing is applied row-wise on the input 1D FFT matrix. The resulting matrix contains the average energy for every cell of the incoming 1D FFT matrix. Next step is to multiply this matrix with the scaling factor:  $\alpha$ .

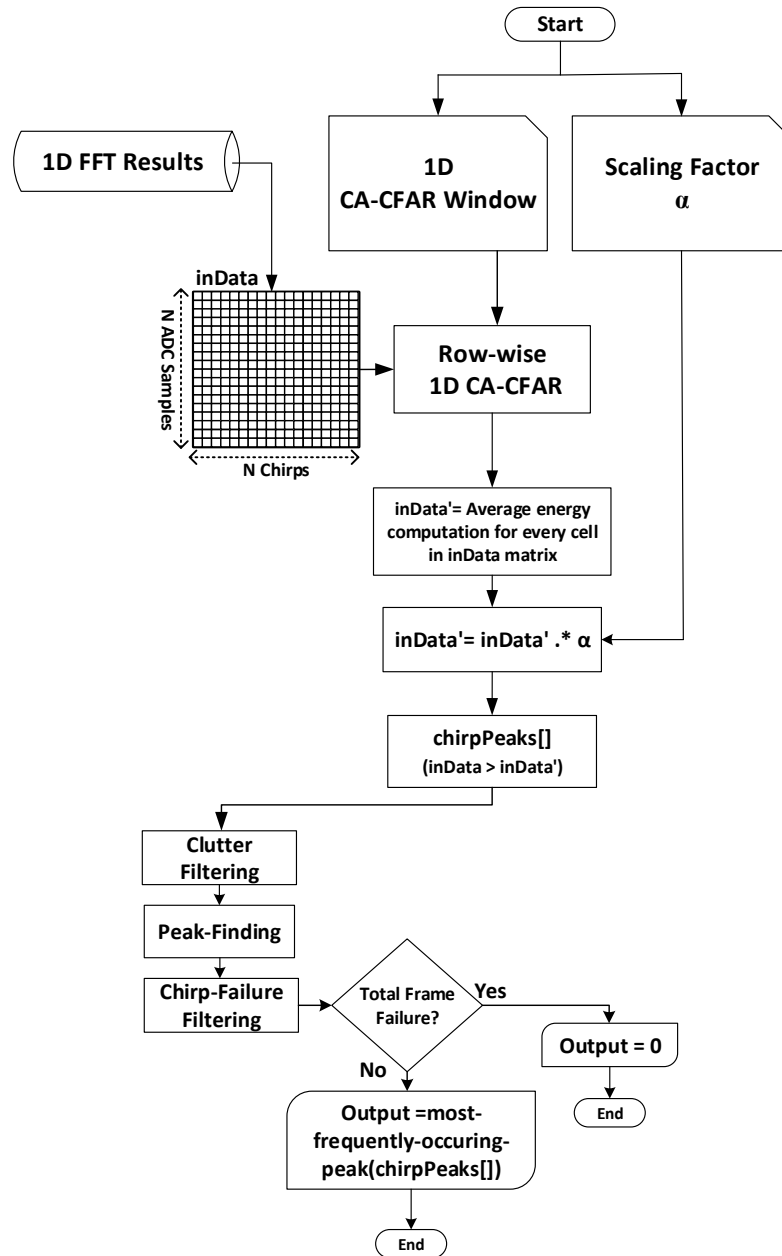


**Figure 5.10:** 1D CA-CFAR implementation flowchart.

The 1D FFT matrix is then compared with the scaled output matrix. The indices of all cells in the input 1D FFT matrix whose value exceeds that of the scaled matrix are stored in a array known as known as chirpPeak (this array corresponds to several peaks in every chirp per frame). After this storing procedure, clutter filtering is applied on this array to remove the clutter and unwanted noise. Subsequently, the algorithm computes for a single peak finding in every chirp of the input matrix and updates the chirpPeak array. Also, at this point, the algorithm applies chirp-failure filtering (removing the chirps that were not able to detect a valid target). Finally, from the final chirpPeak array, the algorithm extracts one single value for the peak signal detection, which occurs to be the most frequently occurring element in the chirpPeak array (single value to which all the chirps agree upon). This peak or value corresponds to 1D CA-CFAR output. In case that

all the chirps failed to detect a target (total frame failure) the algorithm will exit the execution with a zero (0) exit code.

Scaling up now one more dimension, Fig. 5.11 shows the flowchart for the 2D CA-CFAR implementation. Different from the 1D implementation, this algorithm will start by taking the 2D FFT matrix as the input. In this case, a two dimensional (e.g.,  $Guard_{size} = 8 || Train_{size} = 32$ ) sliding window is defined. The algorithm is then executed using the same steps as for the 1D implementation up to the point of peak finding.

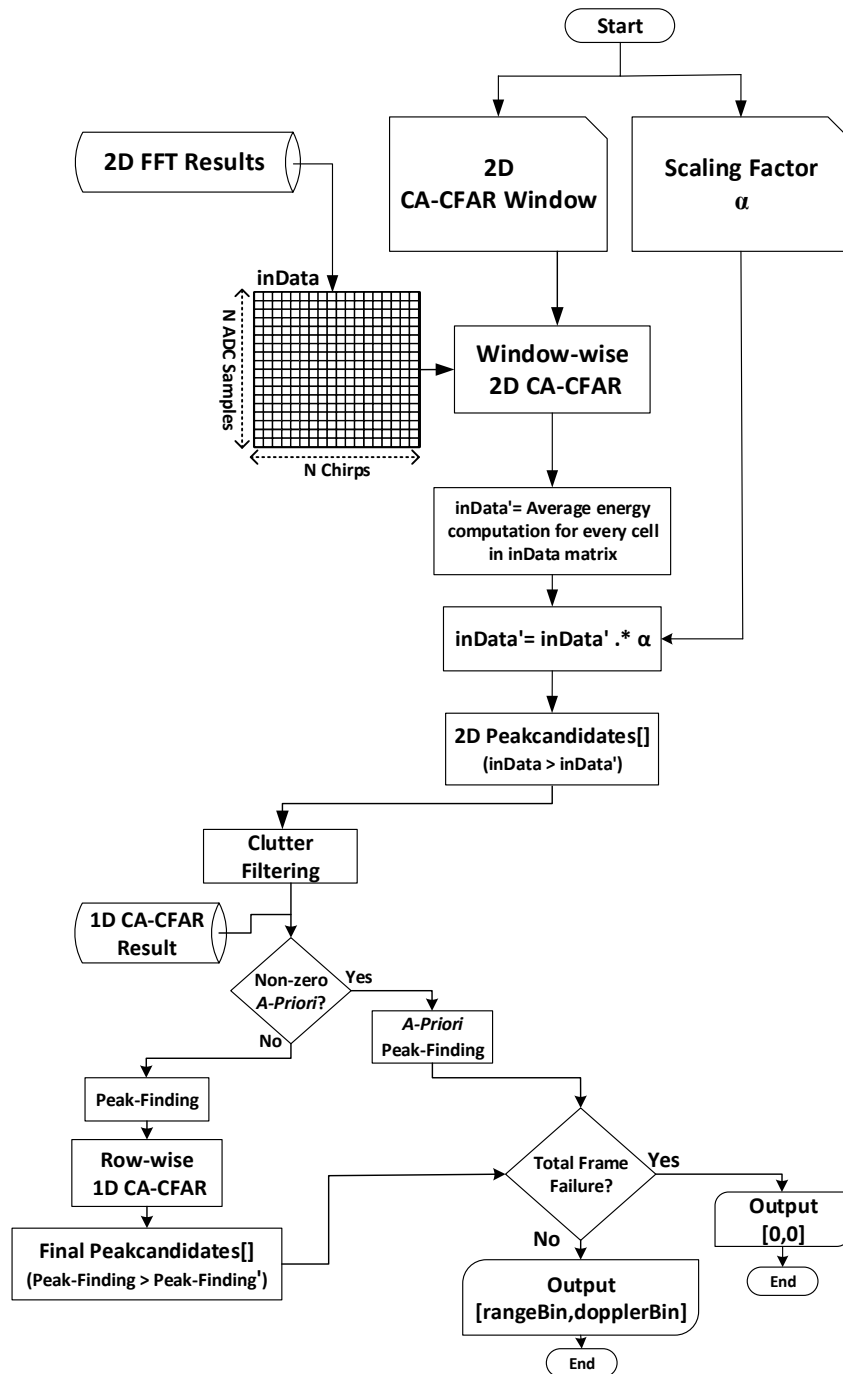


Figure 5.11: 2D CA-CFAR implementation flowchart.

For this thesis project, we have developed a “*handshake*” implementation between the 1D and 2D CFAR algorithms. This means that for a positive case, if the 1D implementation could detect a target accurately, then this result will be used as an *a-priori* knowledge. This previous result will accelerate the 2D implementation in the search for the correct signal peak and the algorithm will output a vector with the range and Doppler bin estimation.

In the case that the 1D implementation fails to detect the target, then the algorithm will follow a two-step procedure. First, a normal peak finding procedure is executed to extract the strongest possible candidates. Following this procedure, an embedded 1D vector sliding window is applied again over this candidate data-set (with their corresponding neighbouring cells) in order to separate radar clutter from target detection. At the end, the algorithm will once again output a vector with the range and Doppler bin estimation. Finally, in case that all the code failed to detect a target (total frame failure) the algorithm will exit the execution with a zero  $([0, 0])$  exit code. These two added features in our own CA-CFAR implementation will be further analyzed in the result section to see their impact on the performance of the algorithm compared to an original CA-CFAR implementation or to a target detection routine without any CA-CFAR procedure.

### 5.1.7 SNR and RCS Estimation

The calculation of the signal and target parameters such as the SNR and RCS will, as explained in Section 2.2, give an insight on the radar performance and target characterization. In this thesis work, we have implemented two separate methods (one for the SNR and one for the RCS calculation) that will compute these parameters per received frame and separate them per receiver channel (RX).

Despite the mathematical approach for the SNR calculation (2.22), we have chosen to estimate the value of the SNR by analyzing the spectral power of the received signal within the range-Doppler profile. This decision allows the usage of the mathematical model for the RCS calculation and also because, by analysing the range-Doppler map, is easier to separate the radar clutter noise from the thermal noise (especially for static scenarios). This procedure of selecting the “detected” target (from the 1D/2D CA-CFAR algorithm) signal energy ( $S$ ) and comparing it with the neighbouring bins (range and Doppler) signal energy ( $Sn$ ) can provide better results. The flowchart diagram introduced in Fig. 5.12 summarizes the implemented algorithm for the SNR estimation.

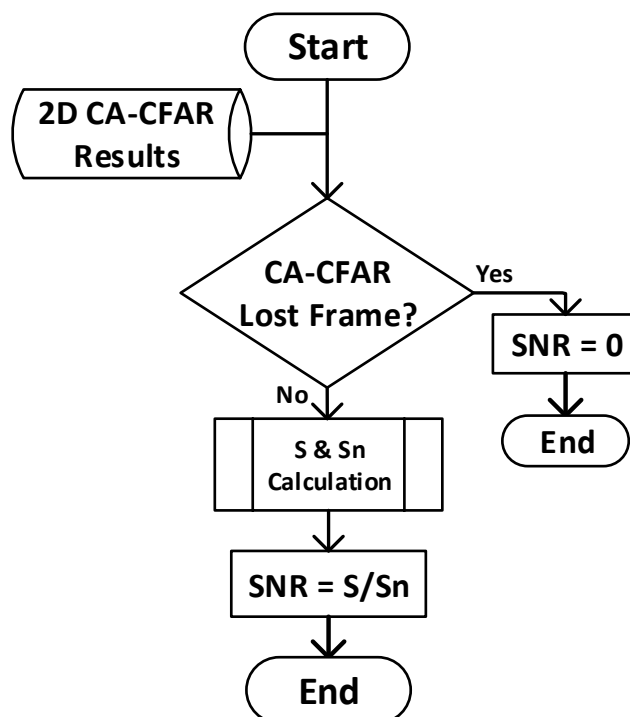


**Figure 5.12:** SNR estimation algorithm flowchart.

It is important to notice from the flowchart in Fig. 5.12 that in case of failed detection from the 2D CA-CFAR algorithm, the SNR calculation will terminate with a zero-value (0) exit code. This exit code value is later used by the RCS algorithm and any other method to filter out lost frames and estimate the frame error rate (FER). Finally, it is important to mention that the estimated SNR value is in dB.

For the case of the RCS calculation, the flowchart diagram introduced in Fig. 5.13 summarizes the implemented algorithm for the RCS estimation.

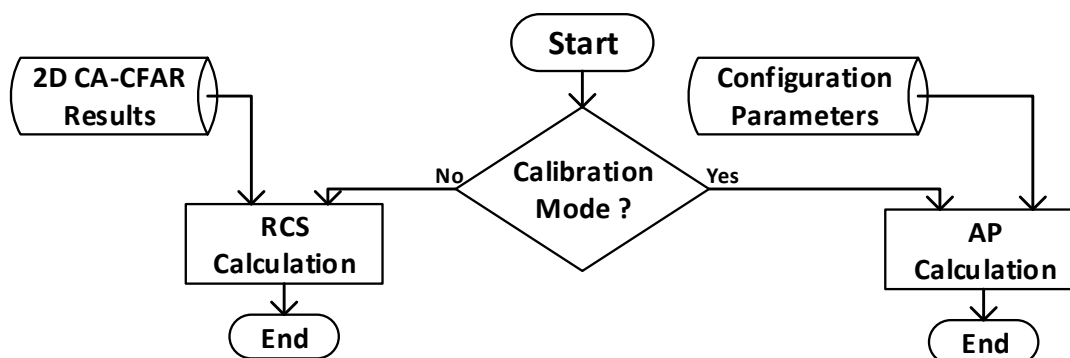


**Figure 5.13:** RCS estimation algorithm flowchart.

It is important to notice from the flowchart in Fig. 5.13 that we have defined two main modes of operation. The first mode is used for calibration purposes. In this mode, the antenna parameter coefficient ( $AP$ ) per receiver (RX) is calculated based on (2.24). In this mode, it is assumed that the user will provide (as part of the configuration parameters) the distance to the target and the RCS value ( $\sigma$ ) of the target used as calibration reference. On the other hand, the second operational mode is used for the calculation of the RCS value using (2.25). In this mode, the distance to the target is extracted from the “detected” result (from the 1D/2D CA-CFAR algorithm) and the antenna parameter coefficient is the one obtained from the calibration procedure.

### 5.1.8 The Spectral Power of the Raw ADC Data

As a final step, before displaying the results at every stage (range, range-Doppler, and angle estimation) or calculating the SNR and RCS value, a correction factor must be applied on the spectral power obtained after the corresponding FFT transformation. This correction factor, will allow us to interpret the data on a dBFS (decibel relative to full scale) or dBm (decibel relative to 1 mW) scale. The output power on a dBFS scale is expressed as

$$P_{\text{out(dBFS)}} = P_{\text{out(FFT)}} - \text{correction}_{\text{factor}} \quad (5.2)$$

$$P_{\text{out(dBFS)}} = P_{\text{out(FFT)}} - \left( 20 \log_{10} \left( 2^{\text{bits}-1} \right) + 20 \log_{10} \left( \sum_{i=0}^{N-1} w_i \right) - 20 \log_{10} \left( \sqrt{2} \right) \right),$$

in which the correction factor is composed of three elements. The first element will normalize all ADC code words to a value of  $\pm 1$ , the second factor will compensate the windowing loss, and the third factor will normalize the samples by the standard real full-scale sinusoidal power. A final dBm representation of the data can be obtained by using

$$P_{\text{out(dBm)}} = P_{\text{out(dBFS)}} + 10. \quad (5.3)$$

## 5.2 HW-Scenario Definition

All through the development of this thesis work, one main HW scenario testing was organized to capture the raw ADC data from a real-case scenario. This HW test-setup was performed for both stationary and dynamic cases. For the stationary test, the target was placed at a fixed distance from the radar. In this case type, different angle of orientation of the target with respect to the radar was also taken into consideration. On the other hand, for the dynamic test, the radar position was fixed and the target was moving with a relative non-zero speed either towards or away from it. The entire hardware tool-chain test-setup was mounted on a trolley and tested in an open environment at the AstaZero test-track. The trolley was kept stationary and the experiments were carried out for both, stationary and moving objects. The detections were carried out for objects such as the corner reflector, pedestrian, bicycle, motorbike and car.

### 5.2.1 Stationary Test Case Scenarios

In this type of measurement, both the radar trolley set-up and the objects were stationary. Figs. 5.14 and 5.15 demonstrate the ground truth test-case scenarios for the stationary object type.

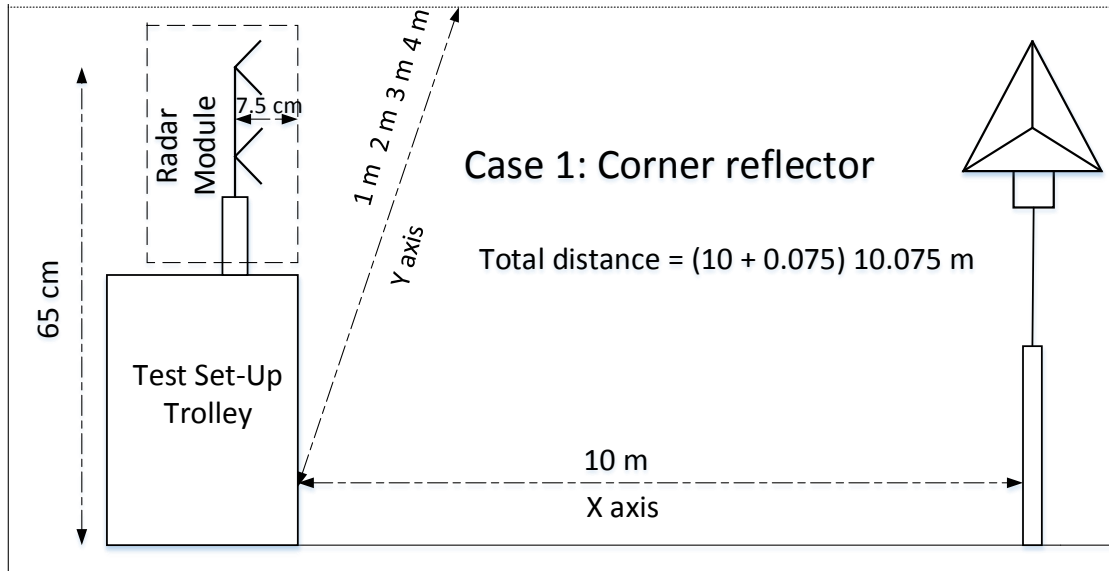


**Figure 5.14:** Test scenario (a): Corner reflector.

For the first case type, involving the corner reflector, the distance between the object and the radar was kept constant along the X-axis throughout the measurement. The trolley was also moved along the positive Y-axis constituting four different azimuth angles as indicated in Fig. 5.14. For every measurement, the ADC data was extracted by the capture board and the corresponding I32 (.csv), and binary (.bin) files were saved for further post-processing.

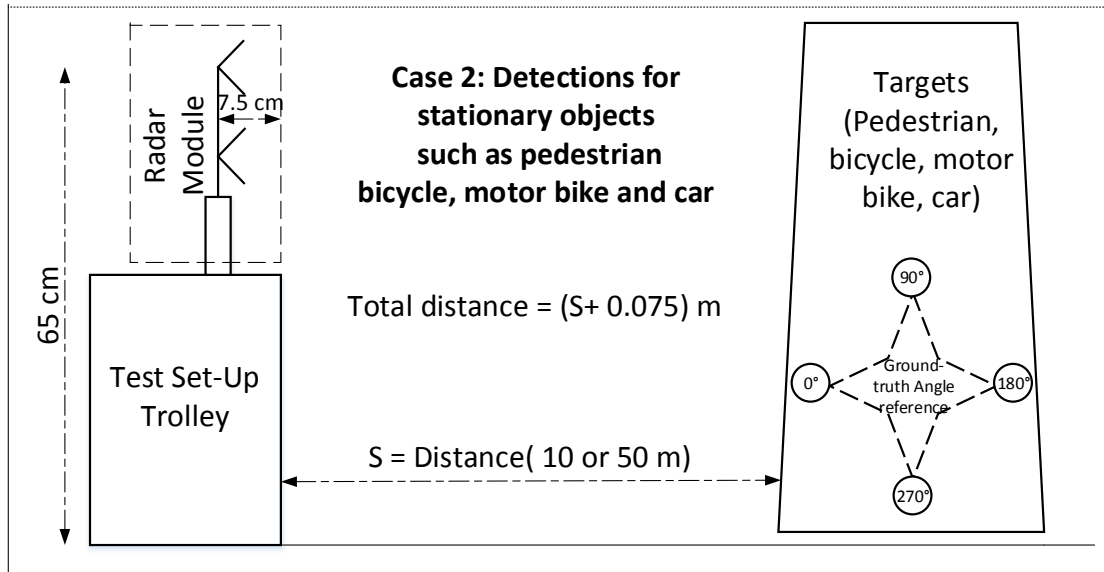


**Figure 5.15:** Test scenario (b): Stationary objects (such as pedestrian, bicycle, motorbike and car).

For the second case type, the radar and the object (such as pedestrian, bicycle, motorbike and car) were placed at line of sight, having a fixed distance between them (either 10 or 50 m). The measurements were also carried out with different angle orientations for every object such as 0, 90, 180 and 270 degrees as seen in the Fig. 5.15. The convention for these angle orientations is also explained in Table 5.1.

**Table 5.1:** Convention used for different angle orientation for every object.

| Angle [deg] | Direction of object                                      |
|-------------|--|
| 0           | Facing towards the radar                                 |
| 90          | Facing lateral towards left (with respect to the radar)  |
| 180         | Facing away from the radar                               |
| 270         | Facing lateral towards right (with respect to the radar) |

### 5.2.2 Dynamic Test Case Scenario

This type of measurement was specifically conducted for targets such as motorbike and car. The radar was always held stationary and the targets moved in a direction either towards or away from it. The measurements were carried out for different relative speed of targets such as 30, 40 and 50 kmph. The ADC data was extracted for every measurement and the corresponding I32 (.csv), and binary (.bin) files were saved for further post-processing algorithms.

### 5.2.3 Configuration of Chirp and Frame Parameters

The values that were used to configure the parameters of chirps and frames for the hardware testing described above is presented in Table. 5.2. Mainly three different profiles were used

to configure the mmWave front-end namely *Prof\_Stat A*, *Prof\_Stat B* and *Prof\_Dyn*. The *Prof\_Stat A* profile was mainly used to configure the parameters for the measurement of target type corner-reflector, whereas *Prof\_Stat B* was used for measurements of other stationary targets such as car, motorbike, bicycle and pedestrian. The *Prof\_Dyn* was used for the measurement of dynamic scenarios involving car and motorbike.

**Table 5.2:** Configuration of chirp and frame parameters.

| Parameter                | Unit         | Prof_Stat A | Prof_Stat B | Prof_Dyn |
|--------------------------|--------------|-------------|-------------|----------|
| Frequency Start          | GHz          | 77.00       | 77.00       | 77.00    |
| Slope                    | MHz/ $\mu$ s | 29.98       | 15.59       | 15.59    |
| Idle Time                | $\mu$ s      | 2.00        | 2.00        | 2.00     |
| TX Start Time            | $\mu$ s      | 0.00        | 0.00        | 0.00     |
| ADC Start Time           | $\mu$ s      | 2.49        | 2.49        | 2.49     |
| ADC Samples              |              | 2048        | 2048        | 2048     |
| Sample Rate              | Ksps         | 37500       | 37500       | 37500    |
| Ramp End Time            | $\mu$ s      | 60.09       | 60          | 60       |
| RX Gain                  | dB           | 30.00       | 30.00       | 30.00    |
| Bandwidth                | MHz          | 1801.62     | 935.64      | 935.64   |
| Chirp Period             | $\mu$ s      | 62.09       | 62          | 62       |
| Number of Frames         |              | 150         | 80          | 150      |
| Chirp Loops              |              | 32          | 32          | 32       |
| Frame Periodicity        | ms           | 50.00       | 50.00       | 50.00    |
| Frame Period             | ms           | 1.99        | 1.98        | 1.98     |
| Wavelength ( $\lambda$ ) | m            | 0.0039      | 0.0039      | 0.0039   |

Table. 5.3 presents the theoretical computed results for the characteristics such as resolution or maximum value for range and velocity estimations per configuration profile. This computation is performed in accordance with the estimation results presented in Table 2.1. Since the slope of the chirp is inversely proportional to the value of maximum range, reducing the slope exactly to half from *Prof\_Stat A* to *Prof\_Stat B* and *Prof\_dyn*, increases the value of maximum range from 187.61 m to 360.72 m. This change in slope was specifically done to have measurements for long range, especially for scenarios involving the dynamic targets.

**Table 5.3:** The theoretical computed results for the characteristics of range and velocity.

| Parameter           | Unit | Prof_Stat A | Prof_Stat B | Prof_Dyn |
|---------------------|------|-------------|-------------|----------|
| Maximum Range       | m    | 187.61      | 360.72      | 360.72   |
| Range Resolution    | mm   | 83.26       | 160.32      | 160.32   |
| Maximum Velocity    | kmph | 56.47       | 56.56       | 56.56    |
| Velocity Resolution | kmph | 3.53        | 3.53        | 3.53     |

# 6

## Results and Analysis

In this chapter, we present the most relevant results and analysis from this thesis work. This chapter is mainly divided into three sections: stationary results, dynamic results and CA-CFAR performance results. In the first section, we mainly focus on the results from the calibration case and target characterization of the car and pedestrian type using polar plots. The second section presents the results from the dynamic scenarios involving a car moving at different velocities and directions with respect to the radar. In addition, the characteristics of parameters such as SNR and RCS of every measured target is also discussed in this section. This chapter finalizes by presenting the performance and success rate of the implemented CA-CFAR algorithm.

### 6.1 Stationary Results

In this section of the chapter, we will discuss the results for the stationary test scenarios. This section is mainly divided into two parts. In the first part, the results from the target detection algorithms such as range (1D) FFT, Doppler (2D) FFT, angle (3D) FFT will be discussed for the corner-reflector target type. In the second part, the results from the evaluation module to characterize the different type of targets will be analyzed.

#### 6.1.1 Calibration Case: The Corner Reflector

A corner-reflector of known RCS value was used for this measurement purpose. This test set-up was mainly used to calculate the SNR and hence to calibrate the  $AP$  per receiver (RX) based on the known values of SNR and RCS as discussed in Section 5.1.7 of Chapter 5.

## Range Estimation

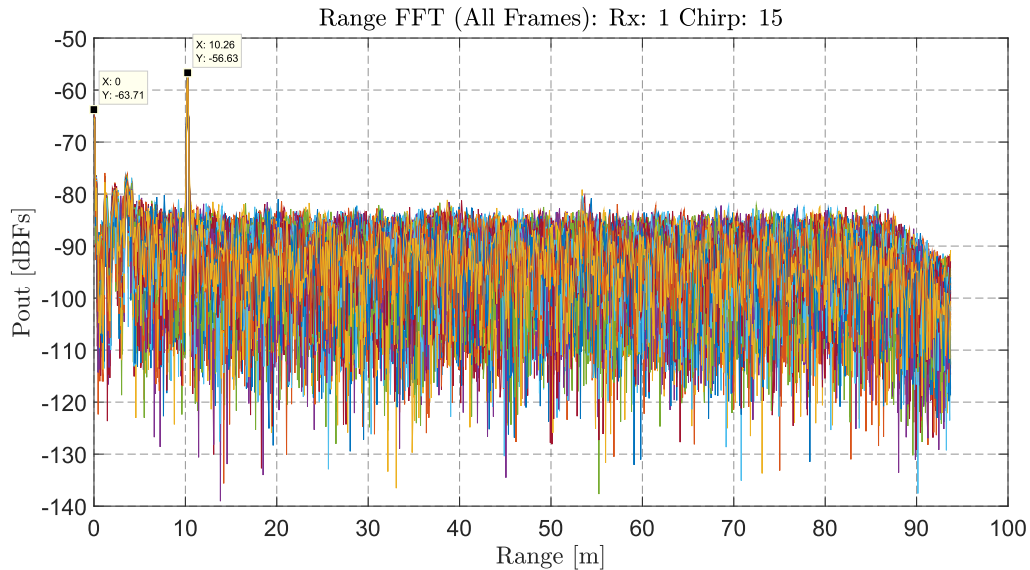


**Figure 6.1:** Range FFT (1D) plot for corner-reflector case.

Fig. 6.1 presents the results for the range estimation when the target was placed at a fixed distance of 10 m and in the line of sight i.e., 0 degrees with respect to the radar. It is important to note that only one chirp per frame for an individual receiver i.e., chirp (No. 15) for *RX1* were taken into consideration for plotting and analyzing the results.

From the (1D) FFT analysis, the peak signal value was found to be  $-56.63$  dBFS. This peak corresponds to the target in the range bin 10.26 m which is approximately equal to the ground-truth data (10 m). From the analytical point of view, it was also observed that the range-bin and peak energy corresponding to target was found to be equal in all the chirps for every frame and for all the receivers. This is because both target and radar were stationary throughout the entire measurement time. Apart from the peak of the target, we also observed that there was a second highest peak at the 0 range-bin with peak energy of  $-63.71$  dBFS. A detailed analysis on the existence of this peak will be presented in the next section.

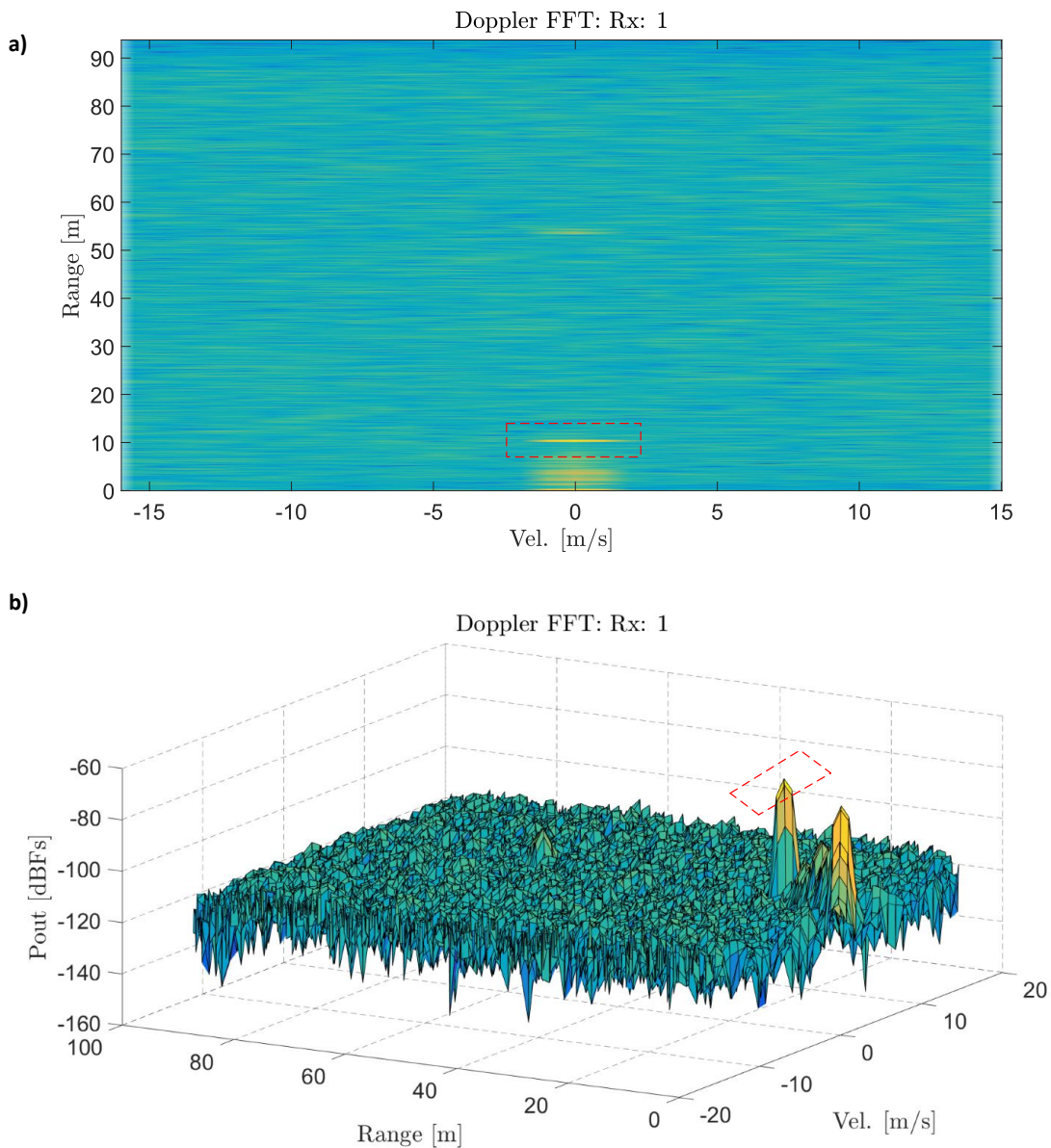
## Velocity Estimation

Fig. 6.2 (a) shows a two-dimensional view i.e., the range-Doppler response and Fig. 6.2 (b) shows the same response in a three-dimensional view, where even the signal level (spectral power) is plotted against range and velocity for the case of the corner-reflector placed at 10 m away from the radar. The response was plotted only for a single frame in one receiver i.e., frame (No. 1) from *RX1*.

From the diagrams presented in Fig. 6.2, several characteristics of radar performance and target identification can be discussed. Initially, let's start with the analysis of the strong peak signal close to the origin (0 range and Doppler bin). This strong peak at the beginning of the spectrum is a consequence of what has been discussed as the radar clutter. We can notice now that the clutter extends not only on the range dimension but also

on the velocity bins. There are several DSP-techniques to eliminate the clutter from the spectrum considering digital filters, moving or sliding windows, among others. However, in this thesis work we have decided to filter out the clutter by establishing safety bins on the range dimension as part of the CA-CFAR algorithms as presented in Fig. 5.10 and Fig. 5.11.

Once the radar clutter has been analyzed, the next step is to analyze the signal peak which is highlighted in both the figures. This signal peak which is concentrated around the 0 velocity-bin and nearly equal to the 10 m range-bin, corresponds to the target. Since the target and radar were kept stationary, the analysis for all the frames from all the receivers yielded a similar result as the one shown in Fig. 6.2.



**Figure 6.2:** Range-Doppler response for the corner-reflector case. Figure a) shows the Range-Doppler response (2D view). Figure b) 3D view (Power-Range-Doppler) response for the corner-reflector case.

## Lateral Distance Estimation

Fig. 6.3 shows the lateral distance estimation for the target type corner-reflector in three different cases.

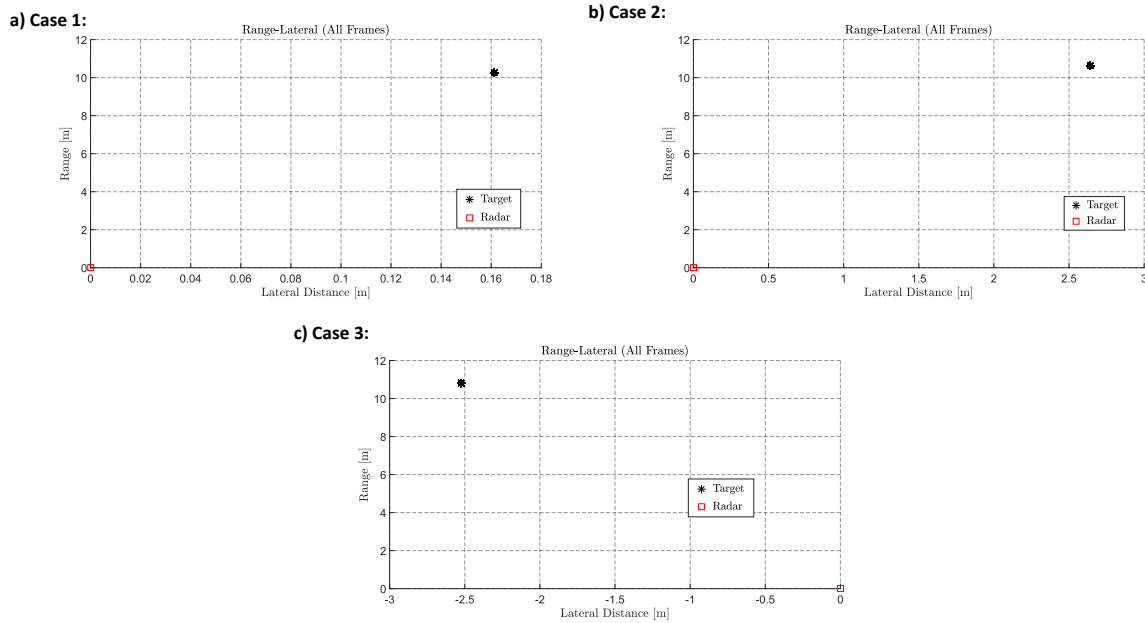


**Figure 6.3:** Lateral distance of the target with respect to the radar. Figure a) presents the lateral distance estimation of target with zero-offset. Figure b) and Figure c) presents the lateral distance estimation of target with positive offset and negative offset respectively.

As we can observe from the diagrams in Fig. 6.3, for the first case type, the target and radar are placed in line of sight i.e., zero-offset. But for the second and third case type, the target is placed with positive offset of 3 m and negative offset of  $-3$  m, respectively. The AoA was estimated for all the cases as shown in Table 6.1 by using the algorithm for angle FFT. This estimated AoA was further exploited to compute the lateral distance for all the cases. The computed lateral distance result from the algorithm is also shown in Table 6.1.

**Table 6.1:** The AoA and lateral distance estimation for the corner-reflector with zero, +3 m and  $-3$  m offset.

| Ground-truth Offset (in m) | Estimated AoA (deg) | Computed lateral distance (in m) | Lateral error rate (in %) |
|----------------------------|---------------------|----------------------------------|---------------------------|
| 0                          | 0.8995              | 0.1612                           | 16.12                     |
| 3                          | -14.3984            | 2.643                            | 11.9                      |
| -3                         | 13.4989             | -2.523                           | 15.9                      |

It was observed that for the case of positive offset, the estimated angle was found to be a negative value and vice-versa for the negative offset case. This is an expected outcome because, according to the theory of AoA,  $\theta$  is negative for targets which lie to the right-side (positive-offset case) and  $\theta$  is positive for targets lying to the left-side (negative-offset

case) with respect to the radar. The computed lateral distances for all the cases were nearly equal to that of the ground-truth data. Nonetheless, the lateral error rate is also presented along with the results.

### 6.1.2 Target Characterization: The Polar RCS

In this section we present the results for static RCS measurements at different distances from the radar (10 and 50 m) utilizing different type of targets. At the same time, in these measurements we also evaluate the RCS response by using different orientation angles as summarized in Table 5.1.

Fig. 6.4 presents the static RCS results for the target-type car at two different distances.

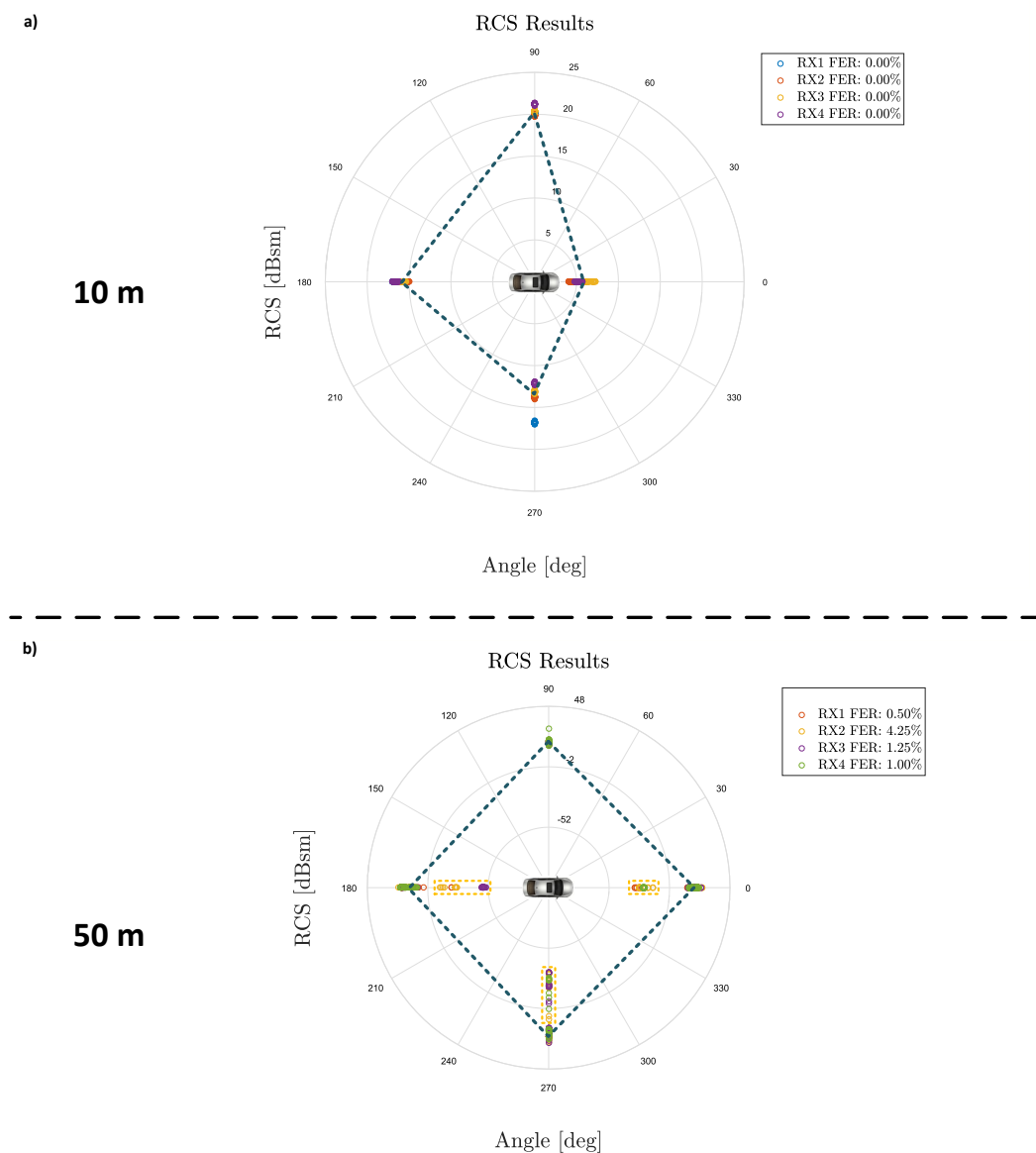


**Figure 6.4:** Static RCS results for car target at 10 and 50 m. Figure a) presents the static RCS results for 10 m distance to the radar. Figure b) presents the static RCS results for 50 m distance to the radar. Detection failure points are marked with a yellow rectangle.

From Fig. 6.4, we can extract some important characteristic of the RCS value for the car target. First, for the 10 m case, we can observe that only the frontal view of the car (0 deg) presents lower RCS estimation in comparison with other views (lateral and back side of the car). This effect is a consequence of two main factors:

- The shape of the frontal side of the car which contains less reflective material and an irregular windshield structure that will bounce waves in other directions.
- The small illumination field of view from the radar that is not able to cover all the main scattering points from the target.

On the other hand, we can observe from the diagram that, for the 50 m case, the distribution of the RCS value is more uniform from all angles of view. This effect is a consequence of the increment in the illumination field of view of the target that now is able to capture most of the relevant scattering points from the target. It is also important to notice that the diagrams present the FER value per receiver (RX channel). This value represents the number of frames that failed to detect the target from all the observing angles. This error result does not represent the FER per angle case.

Finally, the points that are marked with yellow rectangles are a direct effect of a SNR/RCS calculation error as a consequence of a detection failure from the CA-CFAR algorithm. Since radar clutter is mainly concentrated on the zero-Doppler bins, it is challenging to separate these clutter peaks from a stationary target itself. For this reason, in some frames, the CA-CFAR algorithm incorrectly identifies clutter peaks as a target. As a consequence, the subsequent calculation of SNR and RCS will present incorrect results that do not belong to the main tendency from all the other frame detections.

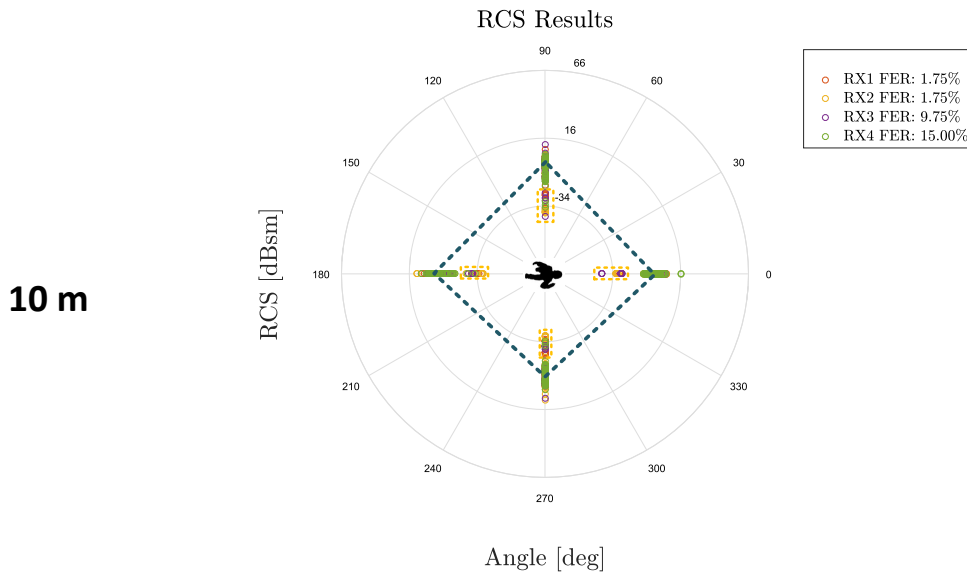


**Figure 6.5:** Static RCS results for pedestrian target at 10 m. Detection failure points are marked with a yellow rectangle.

Fig. 6.5 presents the static RCS results for the pedestrian target type. From the figure it is observed that the RCS values are uniformly distributed for all angles of view. One important observation to note here is that the spanning interval of RCS values for every receiver is relatively larger i.e., the RCS values for every receiver have a larger variation

when compared to the car case described in Fig. 6.4. For the same distance measurement, it was found that the RCS spanning interval for the car is not greater than 1 dBsm compared to the bigger spanning interval ( $> 3$  dBsm) for the pedestrian case.

The difference of the spanning interval can be understood as a consequence of the geometry and the material of each measured target. A pedestrian target does not contain a reflective material as the metal from the car. Also, the irregular shape of the pedestrian geometry will affect the RCS estimation. For all these reasons, we can expect a higher RCS uncertainty for vulnerable road user targets as the pedestrian. For the static RCS results measured over other targets (motorcycle and bicycle), please refer to the diagrams on Appendix B.

## 6.2 Dynamic Results: Moving Target Analysis

In this section, we present the results for the dynamic test scenarios. We will mainly concentrate the results for the test scenario in which a car (target) is moving towards and away from the radar. This experiment was executed several times with different speeds for the car.

### 6.2.1 Range Profile (1D) Results

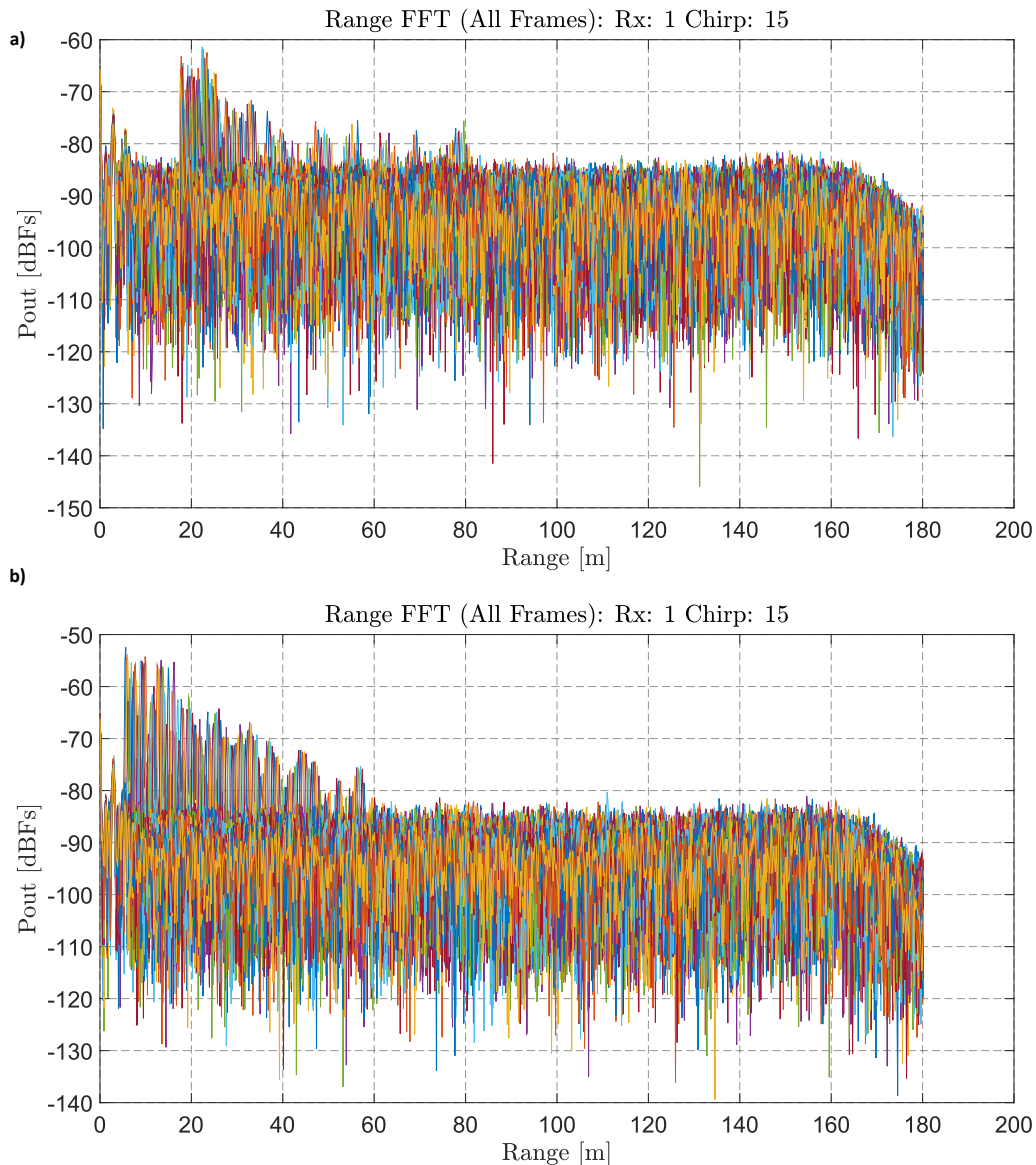


**Figure 6.6:** Range response for the moving car case (40 kmph). Figure a) presents the results when the target was moving towards the radar. Figure b) presents the results when the target was moving away from the radar. Both diagrams present the results for chirp (No. 15) in all frames of the first receiver (RX1).

Fig. 6.6 presents the results for the range estimation when the target (car) is moving towards the radar as in Fig. 6.6 (a) or away from the radar as in Fig. 6.6 (b). Despite the fact that all measurements were executed using the same target, this 1D profile starts to provide some interesting differences not only on the variation of the signal level with respect to the range, but also the signal reflection variation according to the angle (side) the radar is measuring the target with.

With respect to the signal energy variation, we can notice that the signal strength is the highest when the target is closer to the radar (closer the target the more reflections we

will expect). However, as the target gets away from the radar, the signal energy starts to decrease with an oscillatory behavior rather than a linear (as would have been expected). This oscillatory behavior will be later explained in detail within the SNR and RCS analysis.

With respect to the signal reflection behavior in accordance to the orientation angle, we can notice from the diagram a clear difference between the measurements when the radar was looking the front of the car (0 deg) from the ones when the radar was only looking the back side of the car (180 deg). Recalling the results and analysis from the static RCS estimation, the frontal part of the car will present more signal variation than the back side. Consequently, it will be more affected by this oscillatory behavior and present less signal energy.

Finally, as we can notice from the diagram, the two measurements provide different range limits from which the radar first and last detects a strong signal peak within a specific range bin. The main reason for this is that these two measurements are independent from each other and were executed in different ways. From the test with the car moving towards the radar, the car had already a non-zero initial velocity whereas the car started from zero velocity for the second measurement as presented in Fig. 6.6 (b). Notice that, using only these first 1D estimation diagrams, it is not clear to understand if the target was moving away or towards the radar without any prior knowledge. For this reason, further dimensional estimations will be needed, which are explained in the following sections.

### 6.2.2 Range-Doppler Profile (2D) Results

Fig. 6.7 presents the comparison between the range-Doppler estimation for two different test cases. In each of the diagrams, on the upper part there is the range-Doppler heat map which presents the estimation not only for range but also for velocity. On the lower part, there is the representation of the velocity estimation against signal level. Fig. 6.7 (a) represents the case of the target moving towards the radar at 40 kmph. On the other side, Fig. 6.7 (b) presents the case of the target moving away from the radar at 50 kmph. It is important to mention that these diagrams represent only a snapshot of the entire test, i.e., the figures only plot a single frame measurement. For individual range-Doppler heat map results for both (40 and 50 kmph), please refer to the diagrams on Appendix B.

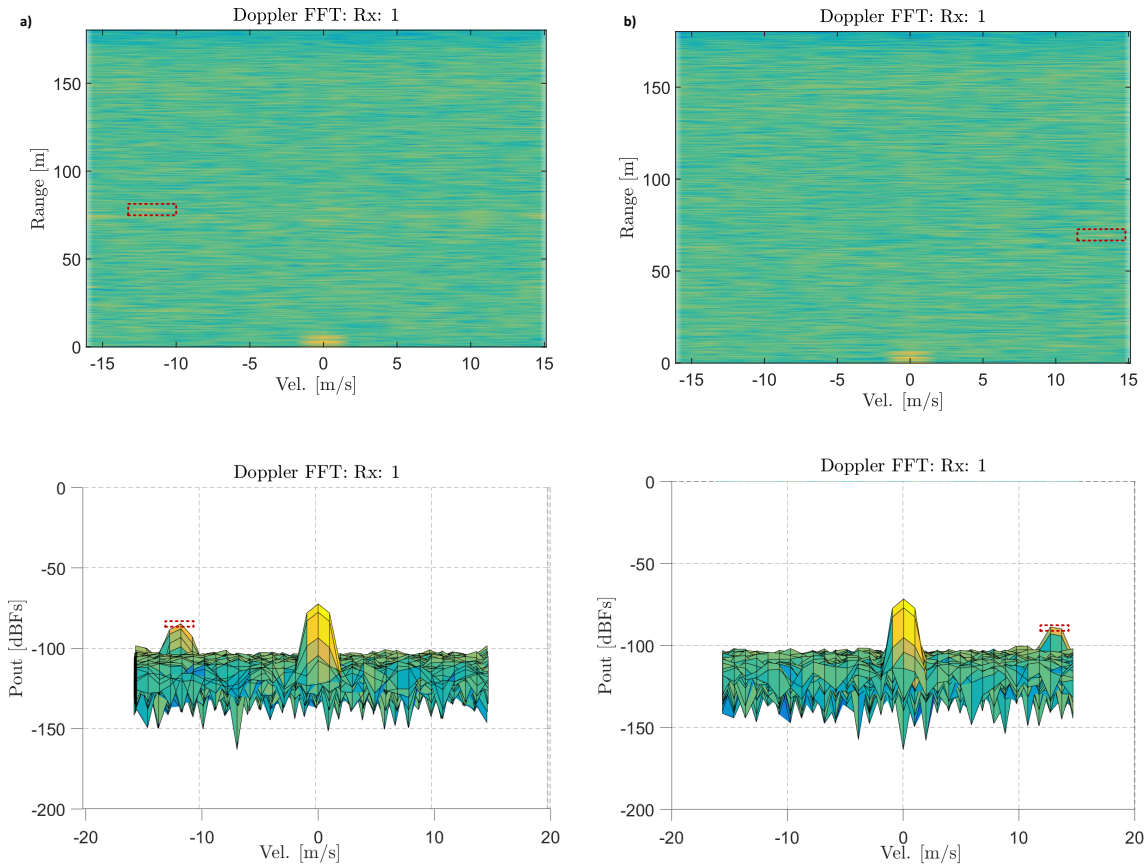


**Figure 6.7:** Range-Doppler response for the moving car case. Figure a) (upper and lower) presents the results when the target was moving towards the radar (40 kmph). Figure b) (upper and lower) presents the results when the target was moving away from the radar (50 kmph).

For the case when the car was moving towards the radar with a speed of 40 kmph, the radar allocated the target with a speed of  $-11.71$  m/s which is equivalent to  $-42.15$  kmph. On the other hand, for the case that the car was moving away from the radar with a speed of 50 kmph, the radar allocated the target with  $13.66$  m/s which corresponds to 49.18 kmph.

Finally, we must reflect on the sign of the measurements. For the case that the target is moving towards the radar, the estimated speed is negative ( $< 0$ ) which agrees with the theory since a movement towards the radar represents a negative phase shift. On the other hand, a movement away from the radar represents a positive ( $> 0$ ) phase shift which translates to a positive estimated velocity as contained in these results. In contrast with the 1D estimation, we can now use the velocity-bin value and its sign to describe not only the speed of the target but also its direction (towards or away) with respect to the radar.

### 6.2.3 Angle Profile (3D) Results

Angular estimation, as described before, can be useful to extract the lateral distance information from the measured target. Fig. 6.8 presents the results from the test case scenario in which the target (car) was moving towards and away with respect to the radar

with a lateral offset. In these diagrams, we have colored the target starting points with green and ending points with red. With this color scheme, the reader will easily understand if the target was moving away or towards to the radar.

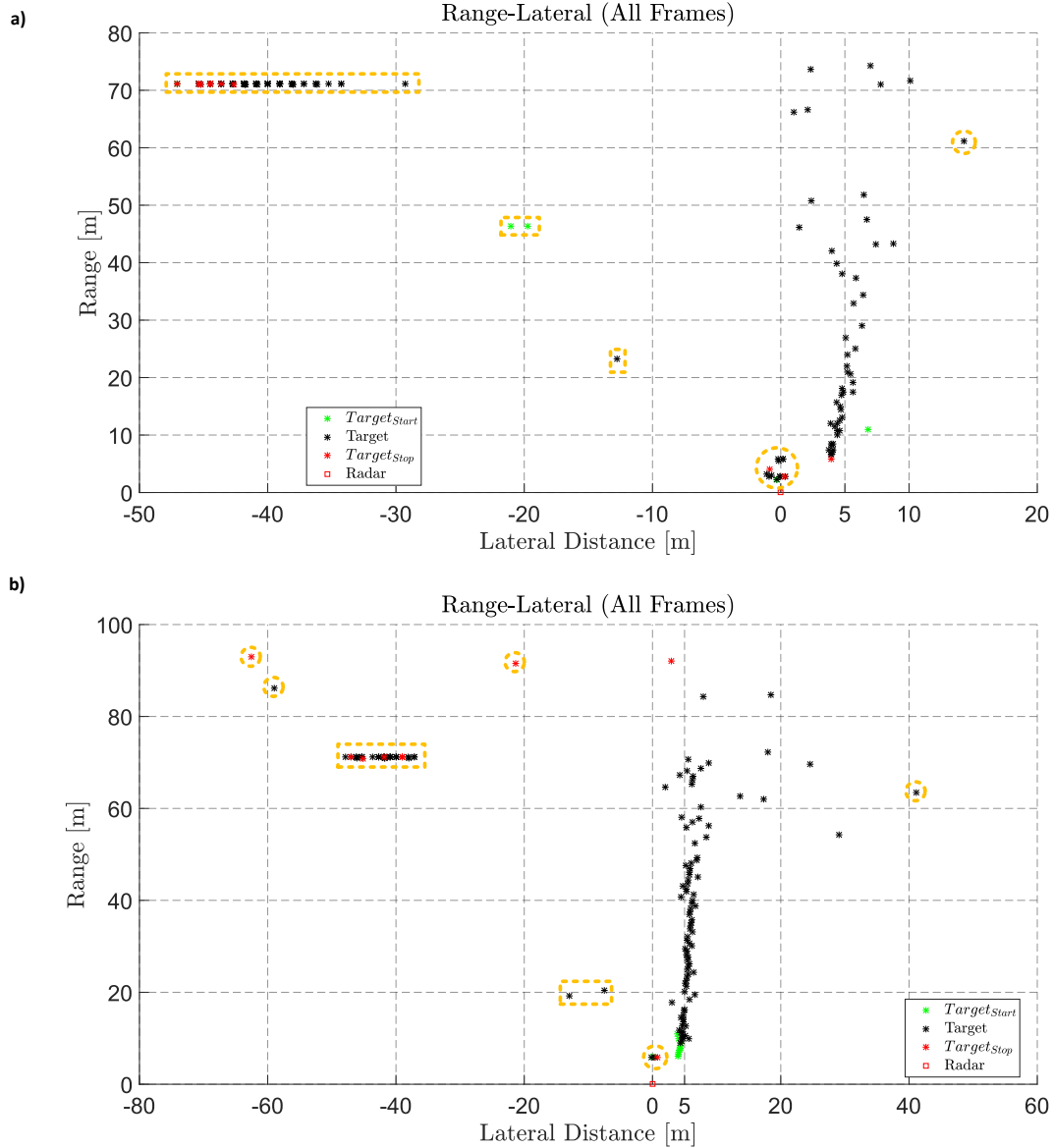


**Figure 6.8:** Lateral estimation response for the moving car case (50 kmph || lateral: 5.5 m). Figure a) presents the results when the target was moving towards the radar. Figure b) presents the results when the target was moving away from the radar. Detection failure points are marked with a yellow circle.

As we can see from the diagram in Fig. 6.8, when the car is closer to the radar there are more detection points than when the car is far away. This far distance effect is a consequence of frame failure (due to the low signal level and the challenges to separate the peak from the noise) that leads to a detection failure which then translates to less detection points. Also, for both test case scenarios, the moving car is always detected on average around a lateral distance of 5 m from the radar. This result agrees with the ground-truth offset which was set to 5.5 m lateral from the radar.

One important characteristic to notice from the results are the points which do not correspond to the cluster from the trajectory of the moving target and are marked in the diagrams with the yellow color. These points are mainly a consequence of a failure in the detection algorithm (1D/2D CA-CFAR) as explained before or an assignment of a wrong AoA due to the limitations in the implemented algorithm. This detection failure effect is more noticeable for the zero (0 m) lateral calculation and will be discussed in further detail in the following section.

### Zero-lateral Moving Target

Fig. 6.9 presents the results for the test case scenario in which the car was moving towards the radar without any lateral offset.

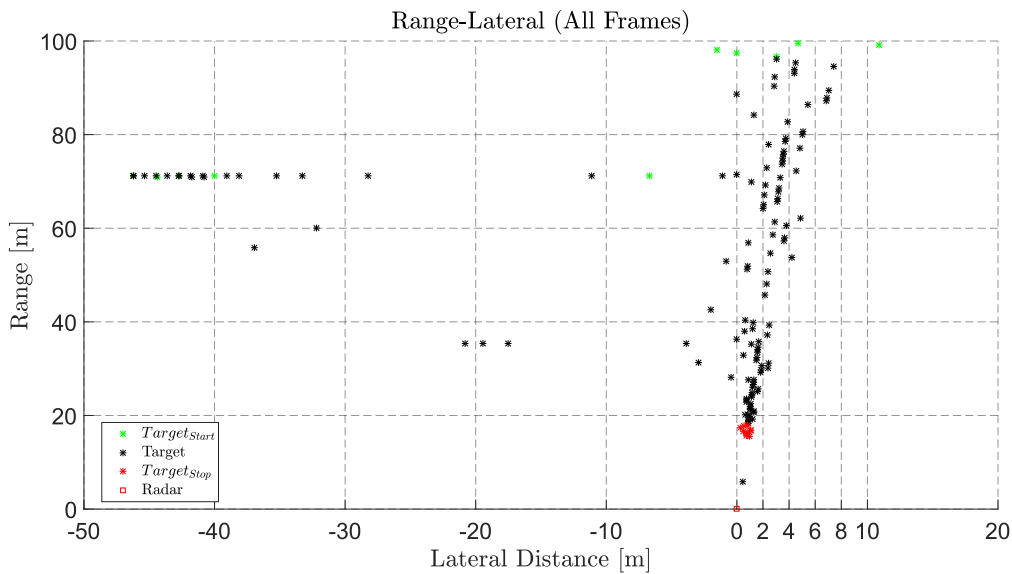


**Figure 6.9:** Lateral estimation response for the moving car case (50 kmph ||lateral: 0 m).

As we can notice from the diagram, there are a lot of detections that are miscalculated. This miscalculation happens due to the fact that the detected AoA is really small (close to 0 deg), however, the detection algorithm still detects a non-zero angle that is later multiplied by the longitudinal distance (5.1), which expands the error value (especially for the long longitudinal distance calculations).

Angular estimation can be further improved by using other DSP beamforming techniques to estimate the direction of arrival (DOA) and to steer the maximum radiation of the antenna pattern to the signal of interest (SOI). In this thesis work, we have used a conventional DOA estimation method which exploits the peaks of the output power spectrum by steering the beam in all possible directions (classic Fourier method). However, as we can see from the results, this method suffers from its poor resolution. On the other hand, subspace methods like multiple signal classification (MUSIC) or estimation of signal parameters via rotational invariance technique (ESPRIT) [13] will dramatically improve the obtained results. Nevertheless, these advance beamforming techniques are out of the scope of this thesis work.

### 6.2.4 SNR and RCS Results

As emphasized in the static RCS results, target characterization parameters (SNR and RCS) give a good description on the signal energy that the radar is receiving from the target reflection as well as the signal scattering distribution from the target. However, in this section we will analyze how these parameters change over range for the cases that the target (car) is moving towards or away with respect to the radar. Fig. 6.10 and Fig. 6.11 present the results for the SNR and RCS over range respectively, for the case of the moving car (40 kmph) with no lateral offset.

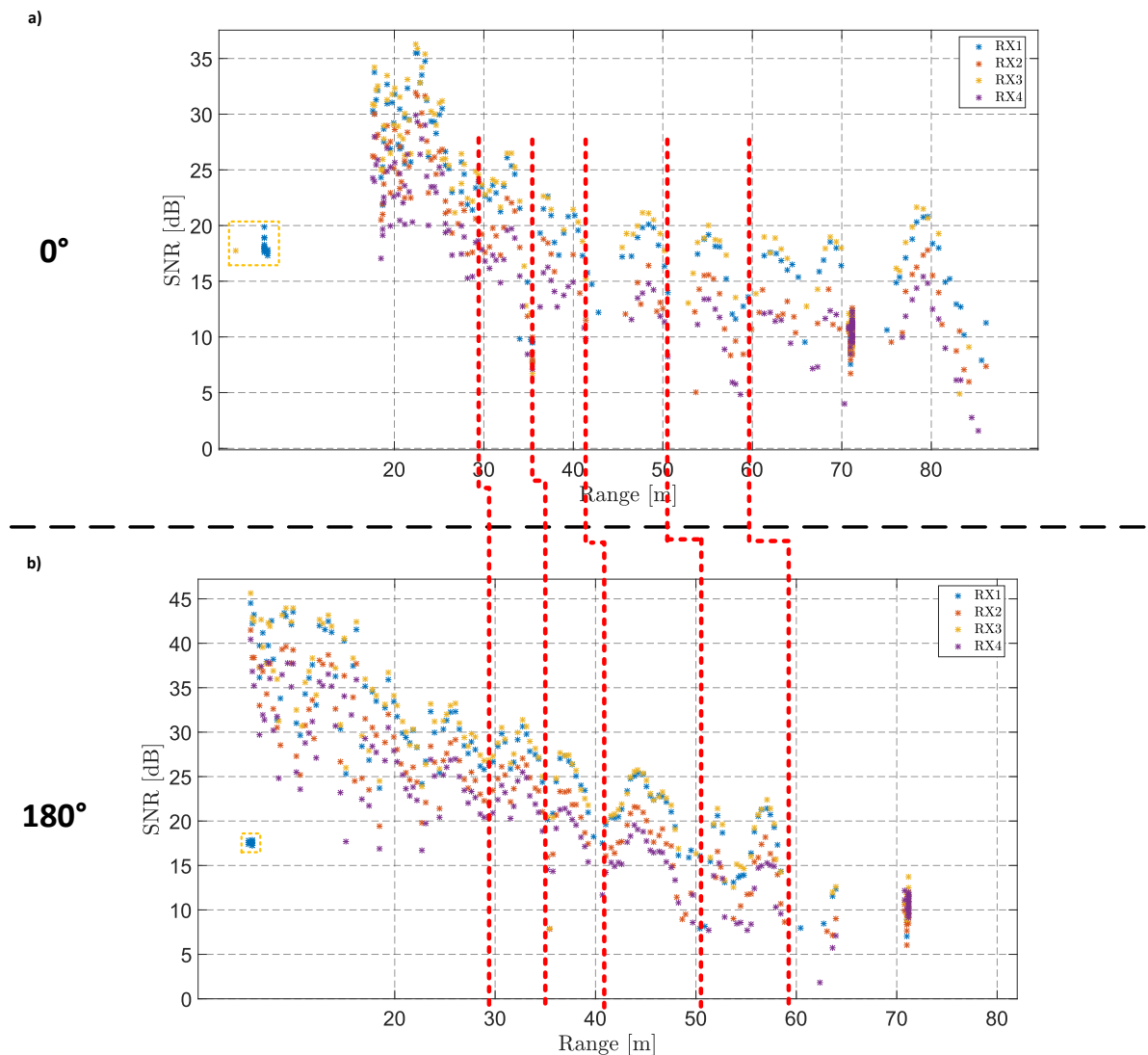


**Figure 6.10:** SNR response for the moving car case (40 kmph). Figure a) presents the results when the target was moving towards the radar. Figure b) presents the results when the target was moving away from the radar. Detection failure points are marked with a yellow rectangle.

As we can notice from the diagrams in Fig. 6.10, the evolution of the SNR over range variation has an overall linear tendency to decrease. This outcome, as presented in other similar results, is anticipated since closer the target the more signal energy would be

expected. However, we can also notice from the diagram that there is an oscillatory behavior over range variation that makes the SNR value to increase and decrease at certain points in range. These points in range are marked with the red-dotted lines. The same behavior we can encounter in Fig. 6.11 for the RCS calculation.

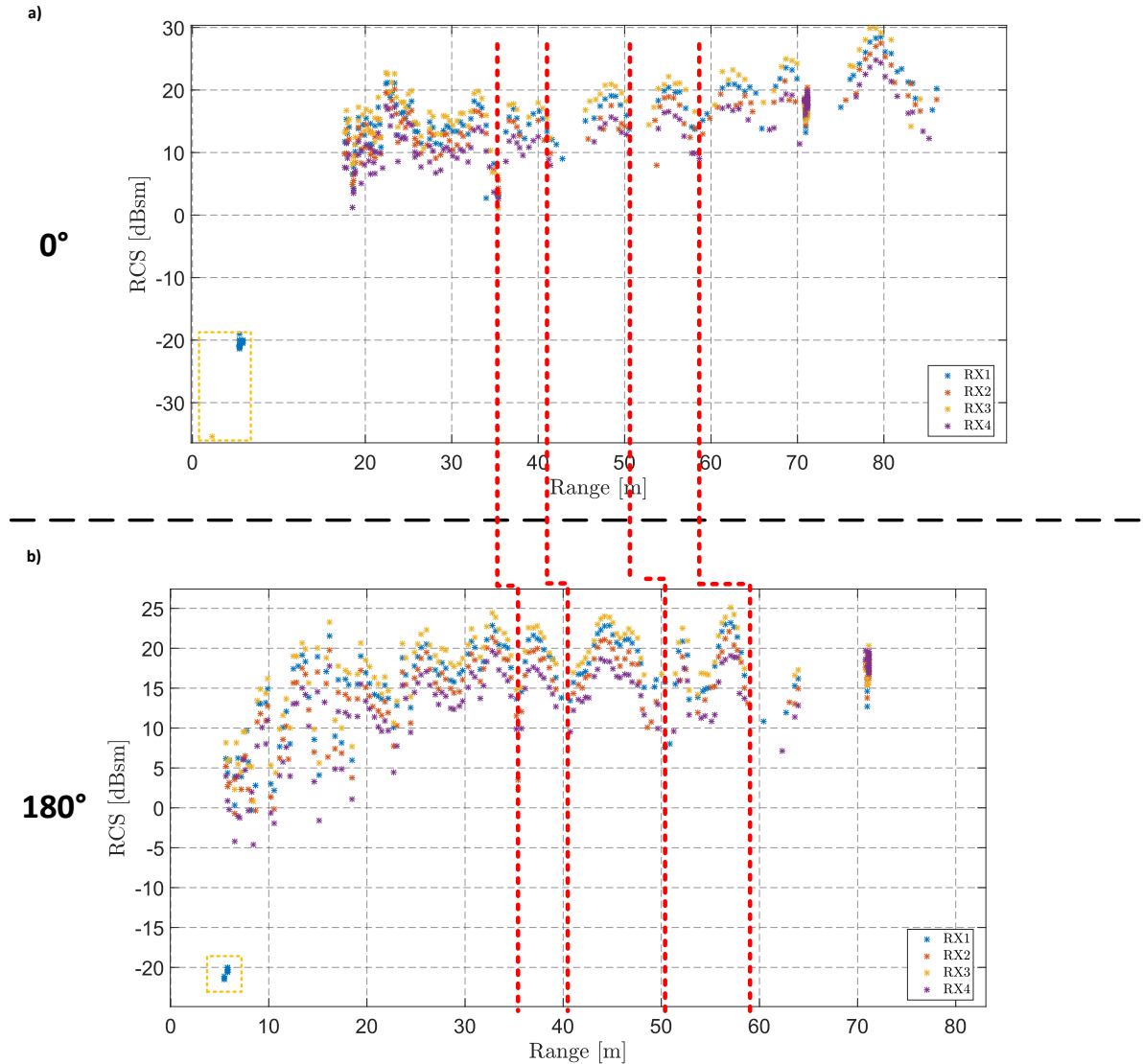


**Figure 6.11:** RCS response for the moving car case (40 kmph). Figure a) presents the results when the target was moving towards the radar. Figure b) presents the results when the target was moving away from the radar. Detection failure points are marked with a yellow rectangle.

As we can notice from the diagrams in Fig. 6.11, the evolution of the RCS over range variation has a low value at close range and it increases into the same oscillatory behavior as the results for the SNR. This decrease of the RCS estimation at close ranges can be explained as the consequence of several factors:

- The dynamics between the SNR value with the distance to the target ( $d$ ) as expressed in the theoretical definition (2.25), makes the RCS a function of distance.
- At close range, the area of the target that is being illuminated by the radar is less,

resulting in a lower RCS calculation.

- The radiation pattern of the antenna and the antenna alignment are more sensitive when the radar is closer to the target, affecting the RCS estimation.

It is important to emphasize that the expected RCS value should be constant and independent of the range variation. Since the RCS is a parameter that describes the target, it is expected to be the same even for the moving target scenarios. However, due to the ground reflection, the RCS estimation presents this fluctuation around its true value that, in most analytical cases, can be approximated by an average calculation.

The red-dotted lines across both diagrams mark the several “*dips*” or valleys of this oscillatory behavior for both test scenarios. This oscillatory behavior can be explained as the effect of the constructive/destructive interference between the signal reflection that bounces straight back to the radar with the other signal reflections that are bouncing back from other obstacles in the environment (e.g., ground). For this reason, the height from which the radar is illuminating the target as well as the height of the scattering point(s) of the target will influence how this oscillatory behavior will be. This means that as long as the radar or the scattering point(s) of the target are kept on the same height, the constructive/destructive interference should happen at the same distance independently from the test case scenario. For the SNR and RCS results for the 50 kmph test case, please refer to the diagrams on Appendix B.

### 6.3 CA-CFAR Performance Results

As we have commented before, in this thesis work we have followed the theoretical implementation of a normal CA-CFAR algorithm for adaptive signal processing. However, we also propose two additional details as part of the CA-CFAR implementation to enhance its performance and success rate on target detection. These two additional characteristics are the “*handshake*” protocol between the 1D/2D CA-CFAR and the “*embedded*”-1D CFAR window as part of the 2D CA-CFAR procedure.

In order to evaluate the performance of our implemented algorithm, we have calculated the success rate on target detection. This success rate can be understood as the percentage of correct frames that detected the target in relationship to the total number of frames. A single frame is considered to be correct if the range-Doppler detected profile (distance and velocity estimation) matches the ground-truth data (experimental distance to the target and zero velocity). Table 6.2 summarizes the success percentage results from all the stationary target test cases both at 10 m ( $r_{10}$ ) and 50 m ( $r_{50}$ ) from the radar with different orientation angles. It also presents the comparison between three scenarios. The first (own CA-CFAR), represents the results by using our implementation. The second (pure CA-CFAR), represents the results by using a normal CA-CFAR algorithm without any extra characteristics. The last one (no CA-CFAR), represents the results by completely removing a CA-CFAR implementation for target detection and just looking directly at the strongest signal peak.

**Table 6.2:** CA-CFAR implementation comparison and success rate percentage results.

| Test Case        | Own CA-CFAR |       |       |       | Pure CA-CFAR |       |       |       | No CA-CFAR |       |       |       |
|------------------|-------------|-------|-------|-------|--------------|-------|-------|-------|------------|-------|-------|-------|
|                  | RX1         | RX2   | RX3   | RX4   | RX1          | RX2   | RX3   | RX4   | RX1        | RX2   | RX3   | RX4   |
| r_10deg_0car     | 100         | 100   | 100   | 100   | 100          | 100   | 100   | 100   | 100        | 100   | 100   | 100   |
| r_10deg_90car    | 100         | 100   | 100   | 100   | 100          | 100   | 100   | 100   | 100        | 100   | 100   | 100   |
| r_10deg_180car   | 100         | 100   | 100   | 100   | 100          | 100   | 100   | 100   | 100        | 100   | 100   | 100   |
| r_10deg_270car   | 100         | 100   | 100   | 100   | 100          | 100   | 100   | 100   | 100        | 100   | 100   | 100   |
| r_10deg_0motor   | 85          | 83.75 | 72.50 | 93.75 | 37.50        | 53.75 | 48.75 | 52.50 | 100        | 96.25 | 100   | 100   |
| r_10deg_90motor  | 100         | 96.25 | 97.50 | 93.75 | 0            | 0     | 0     | 0     | 100        | 100   | 100   | 97.50 |
| r_10deg_180motor | 95          | 48.75 | 81.25 | 66.25 | 33.75        | 27.50 | 7.50  | 21.25 | 100        | 100   | 100   | 100   |
| r_10deg_270motor | 100         | 98.75 | 100   | 100   | 43.75        | 35    | 40    | 37.50 | 100        | 100   | 100   | 100   |
| r_10deg_0ped     | 71.25       | 78.75 | 71.25 | 81.25 | 0            | 0     | 6.25  | 1.25  | 30         | 50    | 56.25 | 81.25 |
| r_10deg_90ped    | 88.75       | 77.50 | 86.25 | 90    | 47.50        | 41.25 | 45    | 47.50 | 51.25      | 70    | 67.50 | 77.50 |
| r_10deg_180ped   | 86.25       | 87.50 | 88.75 | 85    | 52.50        | 62.50 | 43.75 | 53.75 | 58.75      | 76.25 | 73.75 | 92.50 |
| r_10deg_270ped   | 66.25       | 70    | 81.25 | 88.75 | 48.75        | 36.25 | 53.75 | 46.25 | 17.50      | 37.50 | 41.25 | 71.25 |
| r_10deg_0cycle   | 97.50       | 98.75 | 100   | 100   | 48.75        | 57.50 | 47.50 | 65    | 98.75      | 100   | 100   | 100   |
| r_10deg_90cycle  | 100         | 100   | 100   | 100   | 43.75        | 57.50 | 35.50 | 31.25 | 100        | 100   | 100   | 100   |
| r_10deg_180cycle | 72.50       | 76.25 | 80    | 90    | 47.50        | 53.75 | 46.25 | 45    | 67.50      | 86.25 | 88.75 | 98.75 |
| r_10deg_270cycle | 100         | 100   | 100   | 100   | 62.50        | 53.75 | 38.75 | 36.25 | 100        | 100   | 100   | 100   |
| r_50deg_0car     | 95          | 68.75 | 91.25 | 83.75 | 60           | 50    | 48.75 | 52.50 | 0          | 0     | 0     | 0     |
| r_50deg_90car    | 100         | 95    | 100   | 98.75 | 32.50        | 52.50 | 43.75 | 51.25 | 0          | 0     | 0     | 0     |
| r_50deg_180car   | 96.25       | 71.25 | 53.75 | 88.75 | 51.25        | 56.25 | 60    | 53.75 | 0          | 0     | 13.75 | 0     |
| r_50deg_270car   | 98.75       | 16.25 | 70    | 81.25 | 53.75        | 42.50 | 46.25 | 55    | 31.25      | 0     | 0     | 0     |
| r_50deg_0motor   | 0           | 0     | 0     | 0     | 0            | 0     | 0     | 0     | 0          | 0     | 0     | 0     |
| r_50deg_90motor  | 43.75       | 11.25 | 31.25 | 43.75 | 51.25        | 13.75 | 41.25 | 41.25 | 0          | 0     | 0     | 0     |
| r_50deg_180motor | 0           | 0     | 0     | 0     | 0            | 0     | 0     | 0     | 0          | 0     | 0     | 0     |
| r_50deg_270motor | 100         | 97.50 | 100   | 100   | 47.50        | 47.50 | 57.50 | 48.75 | 0          | 0     | 10    | 12.50 |

As we can see from the results in Table 6.2, at close range (10 m distance), all algorithms have an overall tendency to correctly detect the target. We can even see that if we remove the CA-CFAR implementation (no CA-CFAR case), we can still detect the target. At close range, we will expect that the peak of the target will overtake the radar clutter energy so any algorithm will be able to detect correctly the target peak. However, when the target is further away from the radar (e.g., 50 m), we can clearly see that a CA-CFAR implementation is needed. From the data on Table 6.2, we can confirm the enhancement in the results for target detection for all test-case scenarios by adding these extra characteristics over a normal CA-CFAR algorithm.

# 7

## Conclusion and Future Work

The concept of self-driving vehicles is becoming a reality by adapting the current automotive technology to a dynamic one in which there is a fusion of sensors and actuators, advanced algorithms, and a powerful processor to execute software. Directing the vehicle in a way that it will act appropriately under all circumstances by following the rules of the road is one of the most important safety and ethical goals for an autonomous vehicle. Radar plays an important role in autonomous-driving assistance systems (ADAS), which constitutes an intermediate in the development of self-driving vehicles. Automotive radar is particularly used in two ADAS technologies: adaptive cruise control (ACC) and automatic emergency breaking system (AEBS), which improve safety, comfort, convenience, and energy efficiency. In ADAS, radar also forms one of several sensor systems used in applications such as collision avoidance, pedestrian and cyclist detection. For all these reasons, it is fundamental to stress not only the scientific importance on the research of radar-development tools, but also the ethical contribution of this thesis project by supporting systems that will have an impact on reducing deadly road accidents in the future.

In this thesis work, we have presented a complete cycle of radar development from the raw ADC data acquisition up to target detection with adaptive DSP. From all the theoretical background research, practical measurement execution, and constant algorithm development, we have obtained several results that demonstrate, step by step, the correlation between the theoretical expected outcomes and the obtained results from the implemented algorithms. From this correlation, several conclusions can be drawn based on the presented implementation and future work possibilities can be suggested from them as well.

As we could notice from the description of the system implementation, the core of our analysis is based on the Fourier transform, which relates to the study of the signal spectrum. From the implemented work, it is important to notice that a complete target-detection map (range, velocity, and angle estimation) can be obtained only by exploiting the energy and phase change of the signals within the received spectrum. It is important to stress that based on the results, we have proven the capability of the implemented tool to analyze the raw ADC data at every dimensional space (1D, 2D, and/or 3D). Moreover, this tool gives the opportunity to the user to comprehend how the pure input data gradually changes at every stage of the DSP block.

Although the Fourier method provides a fast estimation technique, we could see from the results (especially for the angle estimation case) that further DSP algorithms can be implemented to improve the performance of the system and the detection of the targets. These algorithms, mainly focused on DBF processing, can exploit different subspaces from the spectrum response in order to identify the direction of arrival of the signal of interest. As future work, we propose the implementation of these advance DBF algorithms like

MUSIC or ESPRIT over the angular spectral data so the targets can be properly identified and the detection failure points can be potentially eliminated.

Apart from the angular estimation and further DBF processing that can enhance target detection, there are some other adaptive DSP techniques that can also be used for target detection. In this thesis work, we have demonstrated that with a CA-CFAR implementation we can obtain a first step on target identification based on its signal energy. Moreover, in this thesis project, we have proposed two additional features for the CA-CFAR algorithm to boost target detection. The first, is the “*handshake*” protocol between the 1D and 2D CA-CFAR implementation. The second, is the “*embedded*”-1D CFAR window for an extra radar clutter-target separation as part of the 2D detection process. These extra features presented an improvement on target detection when compared with a regular CA-CFAR implementation. However, as future work, we propose to change the implemented CA-CFAR algorithm with other approaches like the greatest-of CFAR (GO-CFAR), least-of CFAR (LO-CFAR) or the ordered-statistic CFAR (OS-CFAR) and evaluate their impact on the detection performance.

As we could observe from the implemented results, the correctness of the calculation of all radar-signal and target characterization parameters is dependent on the appropriate definition of the antenna parameters ( $AP$ ). For this reason, the importance of having a calibration test scenario (as the one presented at the beginning of the results section) is fundamental to achieve appropriate results that will be more close to the expected outcome and will reduce the error rate.

Target characterization can be considered as one of the important outcomes from this thesis project, since it gives the possibility not only to evaluate the radar performance itself, but also to have some criteria to describe the target that is being measured. Through the static and dynamic cases presented on the results section, we could observe that understanding parameters like the RCS can be used to comprehend not only the type of target that is being measured but also the orientation (side) that the radar is illuminating the target. Considering the dynamic results, we came to the conclusion that the RCS measurement can be affected by additional physical phenomena (constructive/destructive interference) depending on the elevation i.e., height of the radar as well as the height of the main scattering points from the target. The RCS analysis can provide many alternatives for future work from deepening the knowledge on target characterization to constructing new criteria, not only to identify and describe targets, but also categorize them (car, motorcycle, bicycle, pedestrian, among others). Nonetheless, the radar verification tool provided in this thesis project can give the freedom to see the impact of changing main algorithmic design parameters on the DSP results. Consequently, this feature provides a wide spectrum of possibilities for the designer to select carefully the best parameters values in accordance to the test/performance requirements.

The implemented radar signal processing algorithm is limited to the detection of a single target. This limitation was a consequence of implemented adaptive signal processing algorithm (i.e., CA-CFAR), which yielded only in one result that will be a single target. The detection from the CA-CFAR was restricted to a single target mainly because of three reasons. First, there was no data collected for the hardware test-case definition comprising multiple targets since the hardware testing was limited to the detection of a single target. Second, all definitions of hardware-test scenarios must consider all security and ethical conditions to ensure safety to the people that is executing the test as well as the target itself (e.g., pedestrian case). Gathering data from vulnerable road users as the

pedestrian requires extra security considerations that may complicate the execution of the test. For this reason, in this thesis project we avoided a dynamic test case for pedestrian and we just focused on the stationary scenarios. Third, further research needs to be carried out on the criteria to separate detected peaks as individual and different targets. Nonetheless, the complete spectral map i.e., (Range  $\times$  Doppler  $\times$  Angle) containing the target information (single/multiple) from the target detection part of the algorithm has been saved. This feature of saving the complete spectral map characteristic of the measurement brings the possibility not to only understand the radar and the target but also to model how the radar will behave if different physical parameters (frame configuration) are applied within the same/similar test scenarios. With this complete spectral map information, a possible future work suggestion would be to scale the CA-CFAR algorithm from single to multiple target detection.

Finally, a final future work suggestion from the outcome of this thesis work will be related to the variation of the chirp parameters and frame profiles that will allow to explore the impact of the physical characteristics of the radar over the detection results. One interesting field of future investigation can be related to the effect of utilizing the complex-based sampler instead of the real-sampler and to compare/contrast the obtained results.

# Bibliography

- [1] WHO, “Global status report on road safety, 2015,” tech. rep., WHO Library Cataloguing-in-Publication Data, 2015.
- [2] A. G. Stove, “Linear FMCW radar techniques,” *IEE Proceedings F - Radar and Signal Processing*, vol. 139, pp. 343–350, Oct 1992.
- [3] H. Zhou, P. Cao, and S. Chen, “A novel waveform design for multi-target detection in automotive FMCW radar,” in *2016 IEEE Radar Conference (RadarConf)*, pp. 1–5, May 2016.
- [4] J.-J. Lin, Y.-P. Li, W.-C. Hsu, and T.-S. Lee, “Design of an FMCW radar baseband signal processing system for automotive application,” *SpringerPlus*, vol. 5, p. 42, Jan 2016.
- [5] G. Brooker, “Understanding millimetre wave FMCW radars,” *1st International Conference on Sensing Technology*, pp. 152–157, Nov 2005.
- [6] E. Hyun, Y. S. Jin, and J. H. Lee, “Moving and stationary target detection scheme using coherent integration and subtraction for automotive FMCW radar systems,” in *2017 IEEE Radar Conference (RadarConf)*, pp. 0476–0481, May 2017.
- [7] I. Milosavljevic, D. Glavonjic, D. Krcum, D. Tasovac, L. Saranovac, and V. Milovanovic, “An FMCW fractional-N PLL-based synthesizer for integrated 79 GHz automotive radar sensors,” in *IEEE EUROCON 2017 -17th International Conference on Smart Technologies*, pp. 265–270, July 2017.
- [8] V. Winkler, “Range doppler detection for automotive FMCW radars,” in *2007 European Microwave Conference*, pp. 1445–1448, Oct 2007.
- [9] S. Rao, “Introduction to mmWave sensing: FMCW radars.” Texas Instruments (TI) mmWave Training Series, April 2017.
- [10] T. Fei, C. Grimm, R. Farhoud, T. Breddermann, E. Warsitz, and R. Häb-Umbach, “A novel target separation algorithm applied to the two-dimensional spectrum for FMCW automotive radar systems,” in *2017 IEEE International Conference on Microwaves, Antennas, Communications and Electronic Systems (COMCAS)*, pp. 1–6, Nov 2017.
- [11] K. Ramasubramanian, “mmWave radar for automotive and industrial applications.” Texas Instruments (TI) mmWave Training, December 2017.
- [12] M. Parker, “Radar basics–part 2:pulse doppler radar.” EETimes.com, [https://www.eetimes.com/document.asp?doc\\_id=1278808&utm\\_source=eetimes&utm\\_medium=relatedcontent](https://www.eetimes.com/document.asp?doc_id=1278808&utm_source=eetimes&utm_medium=relatedcontent), May 2011.
- [13] A. Balanis, *Antenna Theory*. Hoboken, New Jersey: A John Wiley and Sons, 2005.

- 
- [14] P. Poshala, R. KK, and R. Gupta, “Signal chain noise figure analysis.” Texas Instruments (TI) Application Report, October 2014.
- [15] M. Miacci and M. Rezende, “Basics on radar cross section reduction measurements of simple and complex targets using microwave absorbers,” in *Applied Measurement Systems* (M. Z. Haq, ed.), ch. 16, Rijeka: InTech, 2012.
- [16] M. A. Richards, *Fundamentals of Radar Signal Processing*. New York: McGraw-Hill, 2005.
- [17] C. J. Venter, H. Grobler, and K. A. AlMalki, “Implementation of the CA-CFAR algorithm for pulsed-Doppler radar on a GPU architecture,” in *2011 IEEE Jordan Conference on Applied Electrical Engineering and Computing Technologies (AEECT)*, pp. 1–6, Dec 2011.
- [18] Texas Instruments, *AWR1443, AWR1243 Evaluation Module mmWave Sensing Solution UserGuide*, 1 ed., May 2017.
- [19] K. Ramasubramanian and B. Ginsburg, “Highly integrated 76–81-GHz radar front-end for emerging ADAS applications,” tech. rep., Texas Instruments, Dallas, Texas, 2017.
- [20] Texas Instruments, *AWR1243 Single-Chip 77-79 GHz FMCW Transceiver*, 1 ed., May 2017.
- [21] Texas Instruments, *MMWAVE DEVPACK UserGuide*, 1 ed., May 2017.
- [22] Texas Instruments, *TSW140X High Speed Data capture/Pattern Generator card*, 4 ed., March 2012.
- [23] Texas Instruments, *Radar Studio GUI*, 2016-2017.
- [24] Texas Instruments, *High Speed Data Converter Pro GUI*, 2013.
- [25] V. Dham, “Programming Chirp Parameters in TI Radar Devices,” tech. rep., Texas Instruments, Dallas, Texas, 2017.

# A

## Appendix 1

### Setup for Hardware Tool-chain

**Connection between BoosterPack and the DevPack:** The connection between the BoosterPack and the DevPack is made over the 20-pin launchPad connectors and the 60-pin HD connectors. The two boards are directly connected over the 20-pin connectors, whereas the 60-pin HD connectors are connected using a separate Samtec cable. The BoosterPack is always placed above the DevPack [21]. Fig. A.1 shows the hardware connection between the two boards.

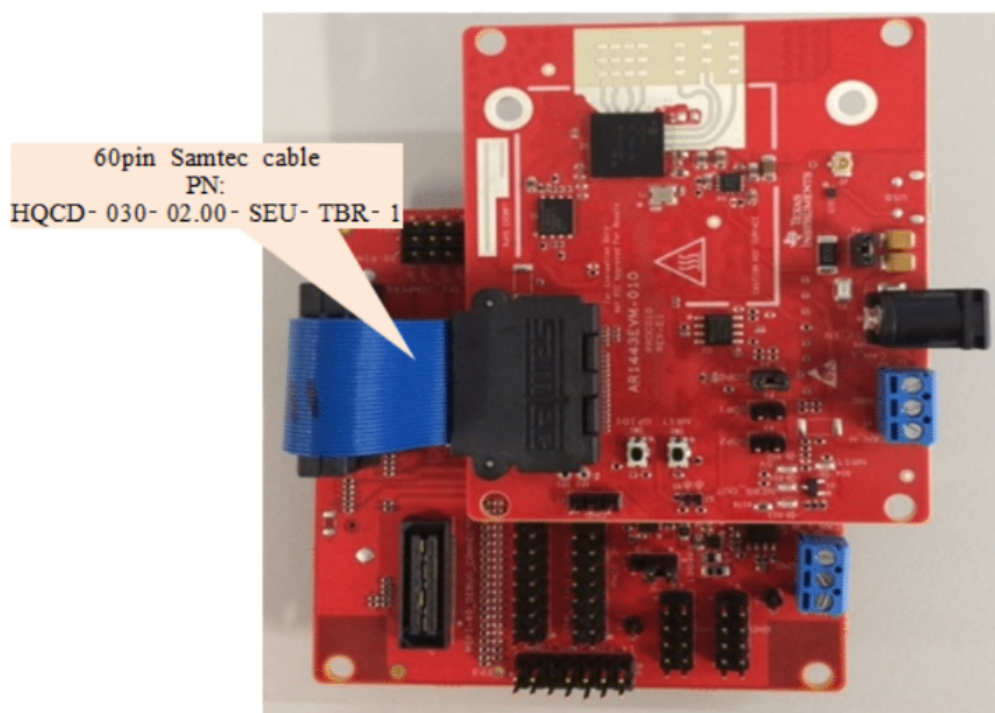


**Figure A.1:** BoosterPack connection with DevPack [21].

**Connection between BossterPack, DevPack and TSW1400EVM:** To set-up the entire hardware tool chain, a 120-pin Samtec cable is used to establish the connection between the J6 (120-pin connector on the DevPack) and J3 ADC input connector on the TSW1400 EVM [21]. Fig. A.2 shows the front and read end view of the entire hardware setup that is used in this thesis work.

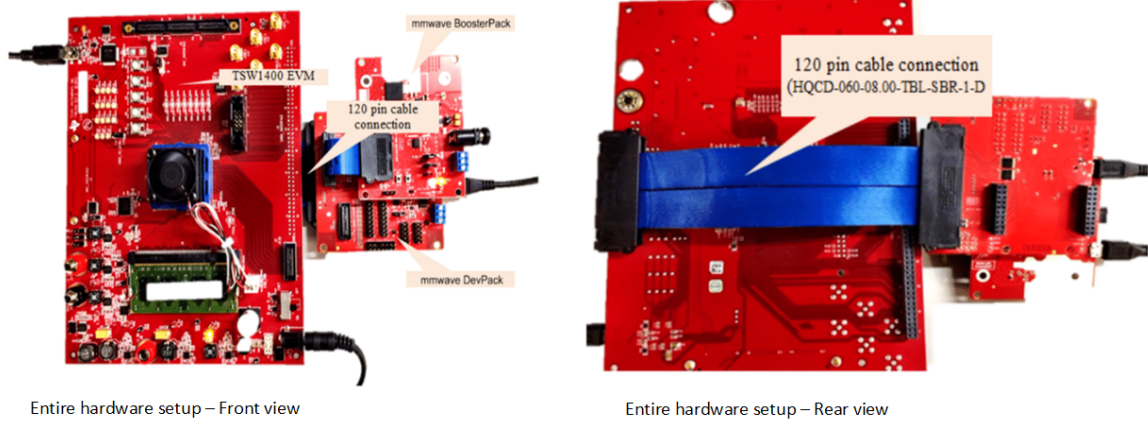


**Figure A.2:** TSW1400 EVM Connection [21].



## B

## Appendix 2

## Target Characterization: The Polar RCS

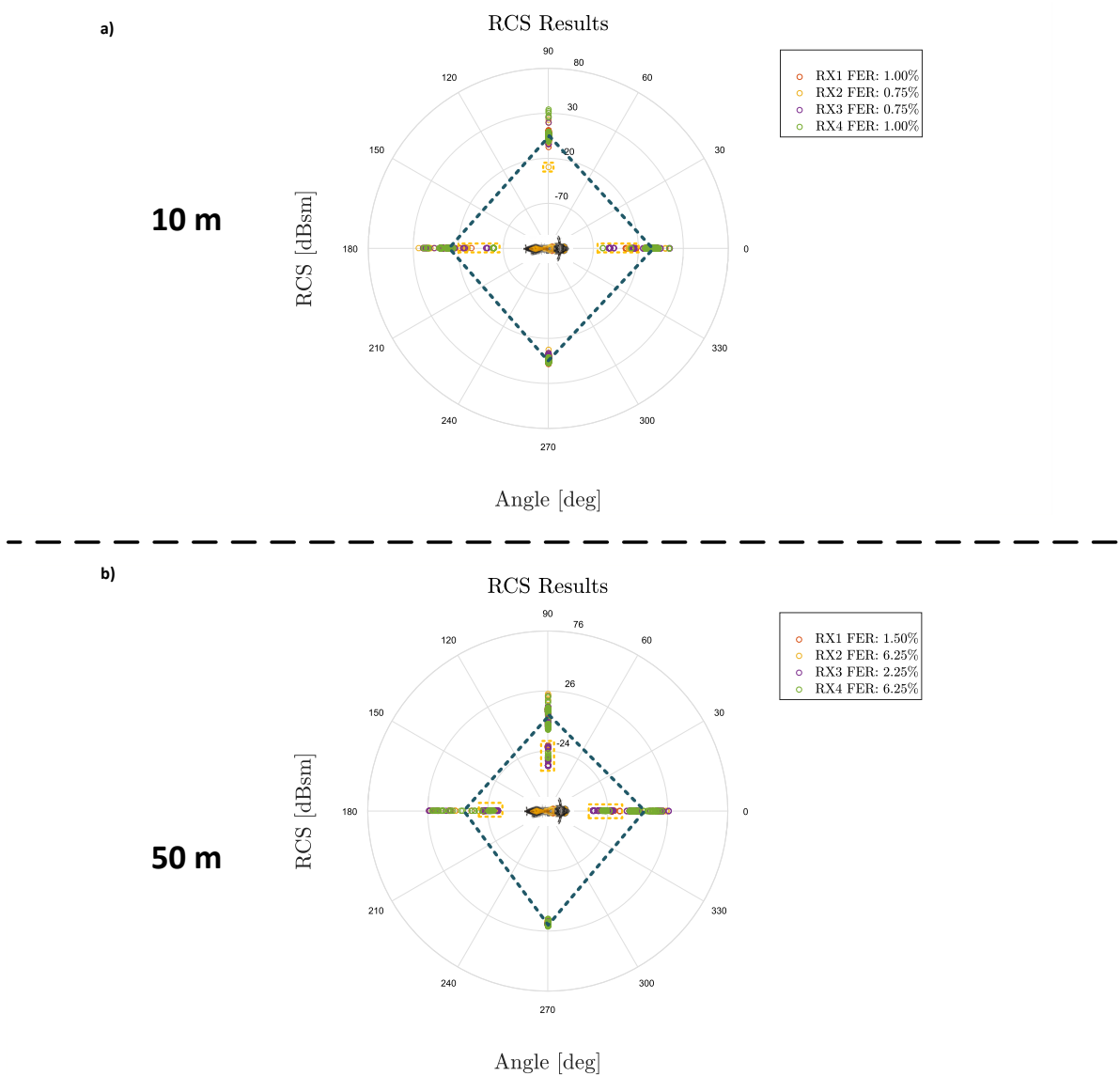


**Figure B.1:** Static RCS results for motorcycle target at 10 and 50 m. Figure a) presents the static RCS results for 10 m distance to the radar. Figure b) presents the static RCS results for 50 m distance to the radar. Detection failure points are marked with a yellow rectangle.

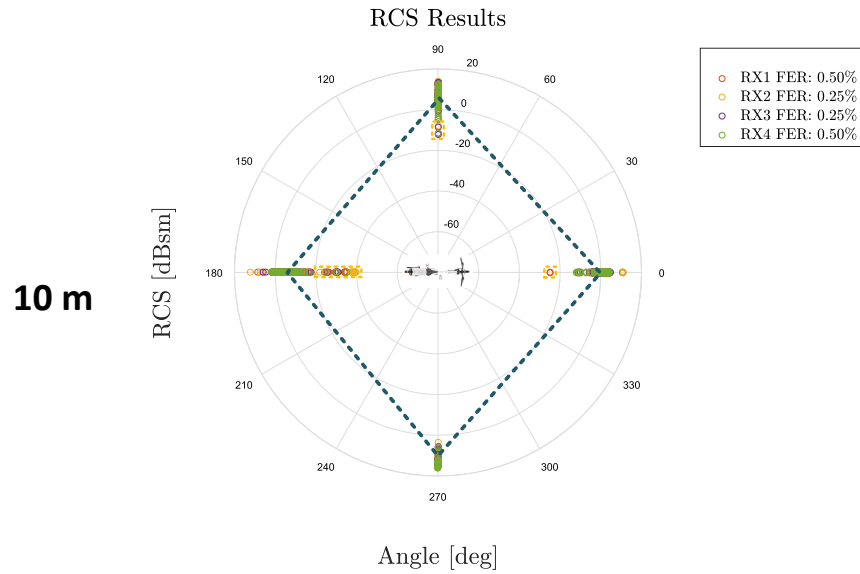


**Figure B.2:** Static RCS results for bicycle target at 10 m. Detection failure points are marked with a yellow rectangle.

## Range-Doppler Profile (2D) Results

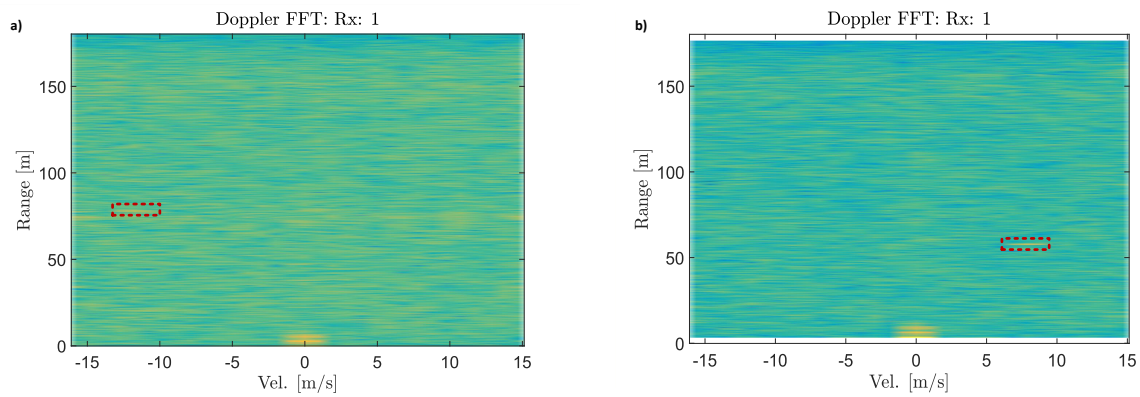


**Figure B.3:** Range-doppler responses for the moving car case (40 kmph). Figure a) presents the results when the target was moving towards the radar. Figure b) presents the results when the target was moving away from the radar. The red rectangle represents the target's peak signal.

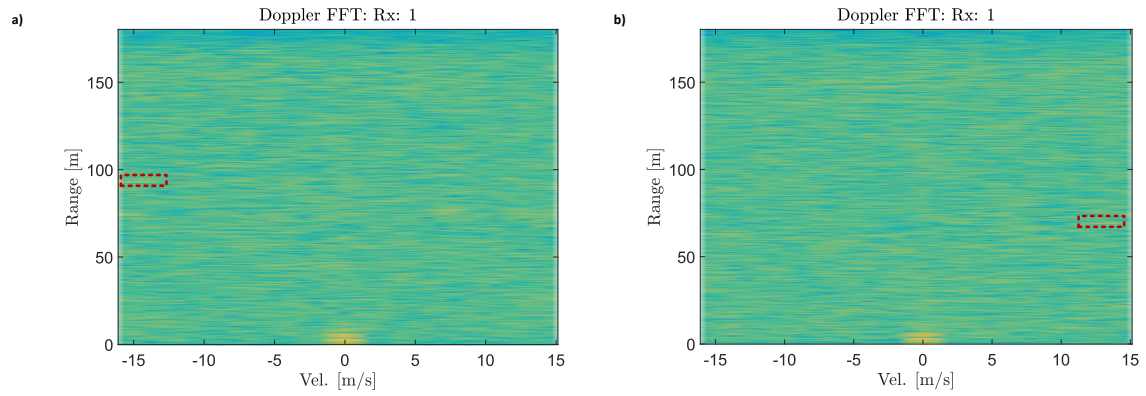


**Figure B.4:** Range-doppler responses for the moving car case (50 kmph). Figure a) presents the results when the target was moving towards the radar. Figure b) presents the results when the target was moving away from the radar. The red rectangle represents the target's peak signal.

## SNR and RCS Results

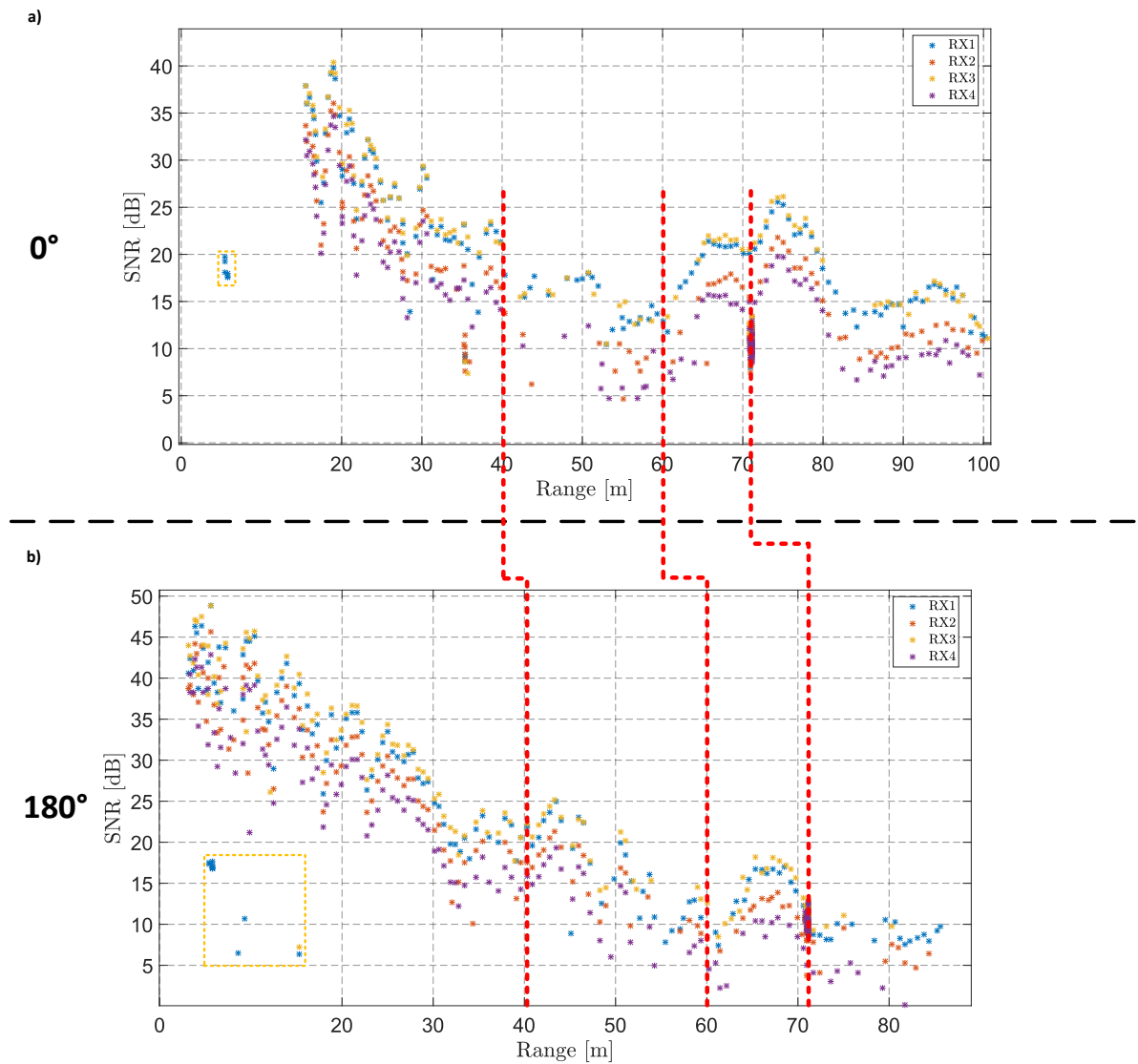


**Figure B.5:** SNR responses for the moving car case (50 kmph). Figure a) presents the results when the target was moving towards the radar. Figure b) presents the results when the target was moving away from the radar. Detection failure points are marked with a yellow rectangle.

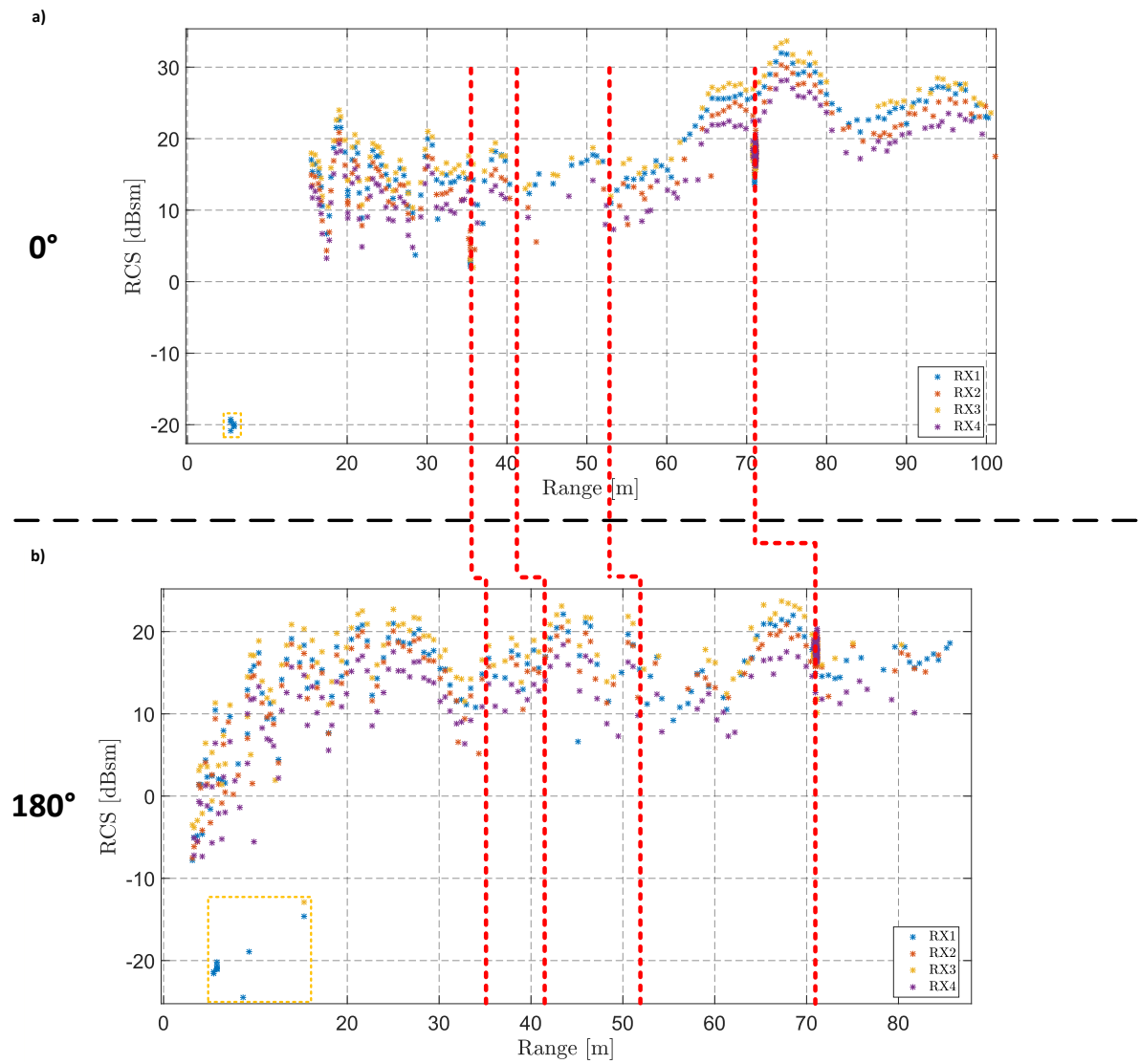


**Figure B.6:** RCS responses for the moving car case (50 kmph). Figure a) presents the results when the target was moving towards the radar. Figure b) presents the results when the target was moving away from the radar. Detection failure points are marked with a yellow rectangle.